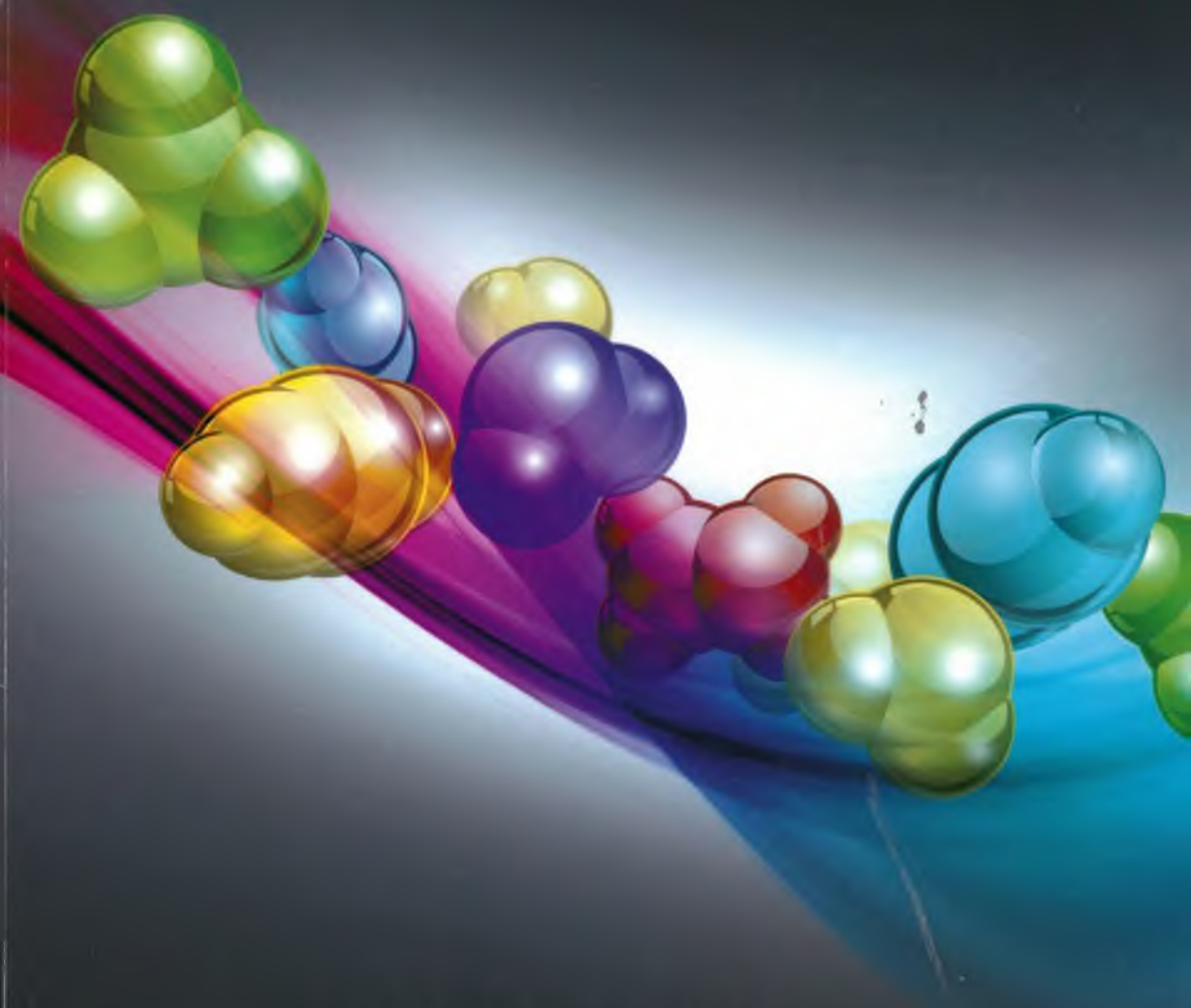


Advancing the detection  
of molecules in gas phase  
with infrared lasers



Raymund Centeno

# ADVANCING THE DETECTION OF MOLECULES IN GAS PHASE WITH INFRARED LASERS

RAYMUND CENTENO

Copyright © Raymund Centeno, 2015

Advancing the detection of molecules in gas phase with infrared lasers,  
*Further development of semiconductor Laser-based Cavity Enhanced Absorption Spectroscopy.*

The copyright of each published article, on which this thesis is based, has been transferred to the respective journals.

All rights reserved. The reproduction, distribution and utilization of this document as well as the communication of its contents to others without express authorization is prohibited.

ISBN: 978-94-6259-605-4

Cover title: *"The flow of molecules"*.

Cover illustration by Promotie In Zicht. Printed by Ipskamp Drukkers.

# Advancing the detection of molecules in gas phase with infrared lasers

Further development of semiconductor Laser-based Cavity  
Enhanced Absorption Spectroscopy

Proefschrift

ter verkrijging van de graad van doctor  
aan de Radboud Universiteit Nijmegen  
op gezag van de rector magnificus prof. dr. T. L. M. Engelen,  
volgens besluit van het college van decanen  
in het openbaar te verdedigen op vrijdag 8 mei 2015  
om 10.30 uur precies

door  
Raymund Centeno  
geboren te Bochum, Duitsland


Promotor: Prof. dr. D. H. Parker

Copromotoren: Dr. F. J. M. Harren  
Dr. S. M. Cristescu

Manuscriptcommissie: Prof. dr. J. Oomens (voorzitter)  
Dr. B. Redlich  
Prof. dr. O. Axner  
Universiteit Umeå, Zweden



This work is part of the research programme of the Foundation for Fundamental Research on Matter (FOM), which is part of the Netherlands Organisation for Scientific Research (NWO).



*La persona  
más próxima  
a mí*

*eres tú  
a la que  
sin embargo*

*no veo  
hace tanto tiempo  
más que en sueños.*

*E. Cardenal*

*Für meine Familie*



# Contents

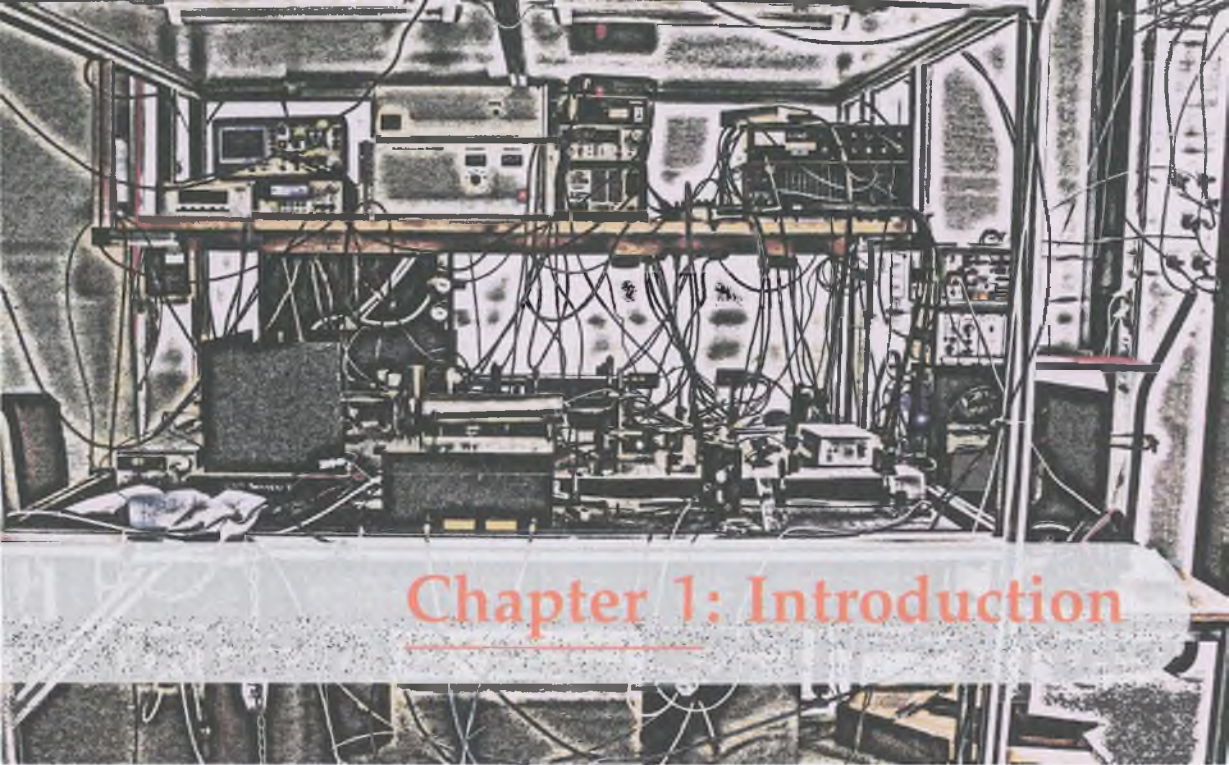
<b>1</b>	<b>Introduction</b>	<b>1</b>
1.1	Development of laser spectroscopy . . . . .	1
1.2	Analysis requirements . . . . .	2
1.3	Absorption spectroscopy . . . . .	4
1.4	Lineshapes . . . . .	5
1.5	The mid-infrared spectral region . . . . .	6
1.6	Mid-infrared light sources . . . . .	10
1.7	The scope of this thesis . . . . .	14
<b>2</b>	<b>Quantum cascade laser</b>	<b>21</b>
2.1	Introduction . . . . .	21
2.2	Tuning methods . . . . .	23
2.3	Applications of QCLs in laser-based spectroscopy . . . . .	25
<b>3</b>	<b>Absorption spectroscopy</b>	<b>31</b>
3.1	Introduction . . . . .	32
3.1.1	The influence of noise on the sensitivity . . . . .	36
3.2	Allan variance . . . . .	39
3.3	Cavity enhanced absorption spectroscopy . . . . .	41
3.3.1	Off-axis integrated cavity output spectroscopy . . . . .	44
<b>4</b>	<b>Three mirror off-axis integrated cavity output spectroscopy</b>	<b>51</b>
4.1	Introduction . . . . .	53
4.2	Materials and methods . . . . .	55
4.2.1	OA-ICOS . . . . .	55
4.2.2	Experimental setup . . . . .	56
4.2.3	Optical enhancement . . . . .	59
4.2.4	Application to apple storage . . . . .	61
4.3	Results . . . . .	62
4.3.1	Instrumental optimization . . . . .	62
4.3.2	Optical enhancement and sensitivity . . . . .	64
4.3.3	Application to apple storage . . . . .	68
4.4	Discussion . . . . .	69
4.5	Conclusion . . . . .	71

5	Sensitivity enhancement in OA-ICOS	75
5.1	Introduction	77
5.2	Materials and methods	77
5.2.1	OA-ICOS	77
5.2.2	Re-injection model	78
5.2.3	Experimental setup	80
5.3	Results	81
5.4	Discussion	84
5.5	Conclusion	85
6	Development of external cavity quantum cascade laser	89
6.1	Introduction	91
6.2	Experimental details	92
6.3	Results and discussion	94
6.4	Conclusion	98
7	Influence of ethanol on breath acetone measurements	103
7.1	Introduction	105
7.2	Results and discussion	110
7.3	Conclusions	112
8	The NICE-OHMS technique	117
8.1	Frequency modulation spectroscopy	118
8.2	Laser frequency stabilization with an optical cavity	122
8.3	Electronic feedback	126
8.4	Residual amplitude modulation	128
8.5	NICE-OHMS	129
9	ECDL-based detection of trace gases with NICE-OHMS	135
9.1	Introduction	137
9.2	Experimental setup	138
9.3	Results and discussion	141
9.4	Conclusion	145
	Summary	149
	Samenvatting	153
	Acknowledgments	157

List of publications 159

Curriculum vitae 161





## Chapter 1: Introduction

### 1.1 Development of laser spectroscopy

**L**IGHT HAS A GREAT IMPACT ON OUR LIVES. Not only because of the sun, but many common tools or important inventions would not work without it. Light gives us the opportunity to study the properties of matter. The field of spectroscopy started in the early 19<sup>th</sup> century, when Fraunhofer and Wollaston observed the first spectral lines in the sun light. This supported the development of fundamental theories like quantum mechanics in the early 20<sup>th</sup> century. With the invention of the laser in 1960, the field of spectroscopy was revolutionized. Atomic and molecular absorption lines could be probed with monochromatic and tunable light sources, which quickly evolved fields like high-resolution spectroscopy and light-matter interactions. Different physical phenomena such as the Raman-effect [1] or the hydrogen Lamb shift [2] were discovered. Furthermore, stabilizing the frequency of a laser led to ultra-sensitive and -precise spectroscopic measurements as well as the control of light-matter interactions [3, 4]. During the last few decades, research and commercial applications of laser spectroscopy in physics, chemistry,

medicine, geology and biology have increased enormously. Examples from physics and chemistry include the formation of Bose-Einstein condensates [5], the study of molecular plasmas [6] and the efficiency optimization of fossil fuel and car engines [7]. Other widely used applications include human breath analysis for disease detection [8], biomedical vibrational imaging [9], air quality monitoring [10], and detection of biologically hazardous or explosive materials for security purposes [11]. Simultaneously, with the increasing demands of light sources for spectroscopy, a wide variety of lasers was developed, including diode lasers [12], quantum cascade lasers (QCLs) [13] and fiber lasers [14]. Each of these lasers possesses unique capabilities and has been combined with different detection methods to contribute significantly to the field of laser spectroscopy. For example, cavity enhancement techniques for increased detection sensitivity combined with diode lasers were used for monitoring ethylene in fruit storage facilities [15]; they were also combined with QCLs operating in the mid-infrared (MIR) and have been applied to human breath analysis for early stage health diagnostics [16, 17]. However, these technologies are mostly based on single frequency lasers with narrow tuning range, thus limiting the analytical capabilities of a detection system. The monitoring of molecular gases requires high selectivity and exceptionally good sensitivities of the order of parts-per-trillion-by-volume (pptv,  $1 : 10^{12}$ ) or parts-per-billion-by-volume (ppbv,  $1 : 10^9$ ) in concentration over a long time period. Thus, there is a strong demand for detection systems with high selectivity, sensitivity and precision. Next to the choice of a light source and the wavelength, the right detection method is crucial to meet these demands.

## 1.2 Analysis requirements

Since the most interesting molecular gases appear only in very low concentrations, their detection requires highly sensitive methods. For the temporal dynamics of processes such as breathing, high speed analysis is required. Also, it is crucial that there is no spectral interference from overlapping molecular absorptions, especially water vapor or CO<sub>2</sub>. In particular, for trace gas analysis the following requirements are relevant:

- **Sensitivity:** The sensitivity is defined in terms of the relationship between the molecular gas concentration and the electrical signal from the detector. The lowest detectable concentration is called the limit of detection (LOD),

a useful entity for assessing the performance of a system. For medically relevant trace gas detection of the most important biomarkers a sensitivity in the range of several ppbv is required, in some cases even pptv levels. An example of an overview of the concentration ranges of important trace gases in breath can be found in Risby et al. [17].

### Info

Sensitivity is a quantity that expresses better performance by smaller values, which intuitively is contradictory when stating 'more sensitive' meaning a lower value of 'sensitivity'. A sensitivity of 1 ppbv is better than one of 100 ppbv, thus stating 'better sensitivity values' or 'better performance' possibly avoids such a misunderstanding. It should be noted that the amount of time, in which this result is achieved, is indispensable for a correct comparison. We shall elucidate this matter later.

- **Precision:** This indicates the reproducibility of a measurement.
- **Accuracy:** A measure of how trustable the measured values are, in other words how close the measured concentration is to the actual one. Figure 1.1 gives a visual distinction between *precision* and *accuracy*.

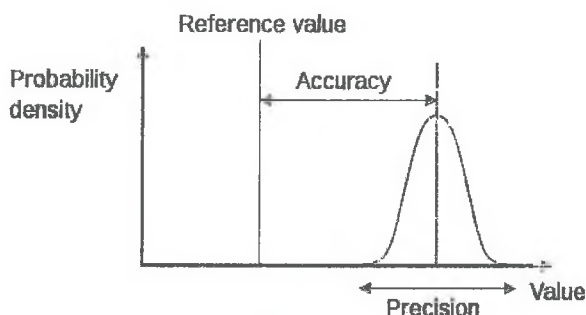


Figure 1.1: Visual representation [18] of the terms *accuracy* and *precision*.

- **Selectivity:** A high selectivity means that a technique is quite insensitive to spectral interference effects arising from overlapping molecular transitions. In many applications, water vapor and  $\text{CO}_2$  are the main interfering molecules.

- **Portability:** Sometimes it is not possible to carry out an experiment in the laboratory, therefore a portable analyzer or an appropriate sampling method is required.

### 1.3 Absorption spectroscopy

A very suitable method for the rapid and sensitive analysis of trace gases is absorption spectroscopy. Here, the type and concentration of the substances contained in a gas sample can be determined from a measured absorption spectrum. A detailed overview of the physical principles of laser spectroscopy can be found in Demtröder [1]. In Chapter 3, a detailed description of the theory behind laser-based absorption spectroscopy is given alongside various cavity enhanced techniques. Here, only the most important phenomena are explained.

Each atom or molecule is uniquely characterized by a number of energy levels  $E_n$ . If light falls on a particle in the energy level  $E_i$ , it can be excited into the higher energy state  $E_k$ , if the relation  $h\nu = E_k - E_i$  holds for the frequency of the light. This energy is then lacking in the beam and leads to absorption. This can be observed by using a gas sample irradiated with a laser and measuring the transmitted intensity. The absorbed intensity plotted against the frequency of light is called the absorption spectrum.

The Beer-Lambert law describes the relation between the optical intensities in the absence and presence of an absorber in the direct absorption sensor shown

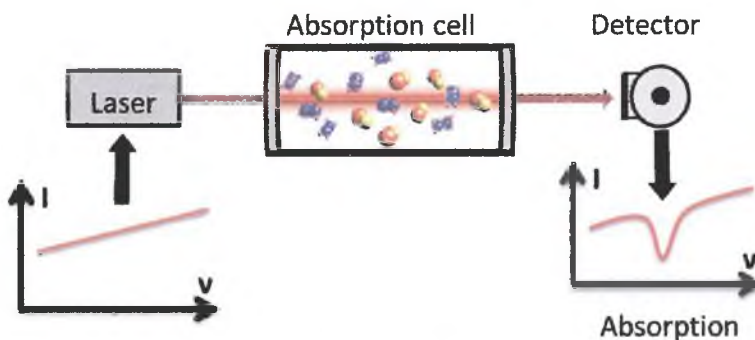


Figure 1.2: Direct absorption sensor.

in Fig. 1.2 for not too large laser intensities and constant absorption coefficient along the absorption path:

$$I_t = I_0 \exp(-\alpha(\nu)L) \quad (1.3.1)$$

where  $I_0$  is the power in the absence of an absorber in Watt,  $\alpha(\nu) = \sigma(\nu)N$  is the linear absorption coefficient of the medium at a given optical frequency  $\nu$  in  $\text{cm}^{-1}$ ,  $L$  is the optical path length in cm of the laser beam within the medium,  $\sigma(\nu)$  represents the specific linear absorption cross-section in  $\text{cm}^2/\text{molecule}$ , and  $N$  is particle density of the absorbent medium in  $\text{molecules}/\text{cm}^3$ . The absorption cross-section  $\sigma(\nu)$  depends on the electromagnetic transition moment, the occupation of the energy levels involved (and thus on the temperature) and the lineshape function. Thus for a known  $\sigma$ , the corresponding concentration can be calculated from the measurement of  $I$  and  $I_0$ . The absorption coefficient  $\alpha(\nu)$  is the product of the absorption cross-section and the particle number. For typical trace gas concentrations (ppbv range), this absorption coefficient is in the order of  $10^{-11}$  to  $10^{-8} \text{ cm}^{-1}$ .

#### Info

There are different possibilities to express the wavelength dependency of a quantity: (1) the wavelength  $\lambda$  [m], (2) the frequency  $\nu$  [Hz] and (3) the wave number  $k \equiv 1/\lambda$  [ $\text{cm}^{-1}$ ]. That means that a wavelength of  $8 \text{ }\mu\text{m}$  corresponds to  $1250 \text{ cm}^{-1}$  and  $37,5 \text{ THz}$ . Moreover, in the MIR a frequency shift of  $30 \text{ GHz}$  corresponds to  $1 \text{ cm}^{-1}$ .

The absorption of a molecule transition is not constant, but extends over a specific frequency interval around the center of the absorption line. The resulting shape depends on various physical phenomena, such as pressure, temperature and velocity. In the following section the main features of different lineshapes are summarized.

## 1.4 Lineshapes

Due to various broadening processes, each absorption line has a frequency distribution around its main frequency. The lineshape function  $f(\nu)$  is related to the absorption cross-section  $\sigma(\nu)$  by

$$\sigma(\nu) = \hat{S} \cdot f_l \quad \text{with} \quad \int_0^\infty f_l d\nu = 1 \quad (1.4.1)$$

where  $\hat{S}$  represents the integrated line strength of an absorption line found in databases like HITRAN [19]. Depending on the broadening mechanism, the absorption line can take several shapes. If the lineshape originates from a homogeneously (natural/lifetime or collision) broadened transition, it can be described by a Lorentzian function, whereas the lineshape has a Gaussian form in case of an inhomogeneously (Doppler) broadened transition. The uncertainty principle relates the lifetime of an excited atomic or molecular state with the uncertainty of its energy. The spectral line describing this phenomenon is called 'Lorentzian' and its normalized lineshape can be written as

$$f_L(\nu, \nu_0) = \frac{1}{2\pi} \frac{(\Delta\nu_L)}{(\nu - \nu_0)^2 + (\Delta\nu_L/2)^2} \quad (1.4.2)$$

where  $\nu_0$  is the transition center frequency and  $\nu_L$  is the full width at half maximum (FWHM) of the normalized Lorentzian lineshape, also called the natural line width.

In gases, variations of the particle velocities affect the spectrum due to their different local environment. This effect is known as Doppler effect and its normalized lineshape, characterized by a Gaussian curve, can be expressed as

$$f_D(\nu, \nu_0) = \sqrt{\frac{4\ln 2}{\pi}} \cdot \frac{1}{\Delta\nu_D} \exp \left[ -4\ln 2 (\nu - \nu_0)^2 / \nu_D^2 \right] \quad (1.4.3)$$

where the Doppler width,  $\nu_D$ , is given by  $2\nu_0/c\sqrt{2kT\ln 2/m}$  with  $k$  the Boltzmann constant,  $T$  the temperature of the gas in K,  $m$  its molecular mass in amu and  $\nu_0$  the transition frequency in  $\text{cm}^{-1}$ . If neither of these two broadening mechanisms dominates, the lineshape is described by a Voigt function, which is a convolution of a Gaussian and Lorentzian profile. Other effects might further influence the lineshape, for example Dicke-narrowing, which occurs when a Voigt profile is recorded under the condition of weak collision broadening. Modified Voigt lineshapes include the Galatry (soft collisions) [20] or the Rautian-Sobelman profile (hard collisions) [21].

## 1.5 The mid-infrared spectral region

Optical spectroscopy is based upon the principle that a molecule is characterized by a certain amount of energy levels and can absorb light at specific wavelengths corresponding to transitions between electronic or rotational-vibrational energy

levels or a combination thereof. Vibrational energies describe how the atoms in the molecule move with respect to each other. The energetic and dynamical properties of molecules are described by the solutions of the Schrödinger equation [22]. The vibrational modes of a diatomic molecule can be modeled using the Born-Oppenheimer approximation [23]. Molecular vibrations are then described by the nuclear Schrödinger equation

$$\hat{H}(R)\Psi(R) = E\Psi(R) \quad (1.5.1)$$

where the wave function  $\Psi(R)$  only depends on the internuclear distance  $R$  for two nuclei of masses  $m_1$  and  $m_2$ . For a diatomic molecule, the Hamiltonian has the simplest form, when the nuclei move in a parabolic potential around their equilibrium positions with equilibrium displacement  $q$

$$\hat{H}(R) = \frac{1}{2}\omega\dot{q}^2 + \frac{1}{2}kq^2 \quad (1.5.2)$$

The solution of the Schrödinger equation is then that of a harmonic oscillator with eigenenergies  $E(v) = \hbar\omega(v + 1/2)$  and frequencies  $\omega = \sqrt{k/\mu}$  with the reduced mass  $\mu = m_1 m_2 / (m_1 + m_2)$  of the two nuclei and the vibrational force constant  $k$ . The harmonic approximation is only good at small displacements around the equilibrium, as anharmonicities and a dissociation are not included in this model. It is often more suitable to use the Morse potential [24], which depends on the dissociation energy of the molecule,  $D_e$ , as an approximation and to additionally include, apart from a classical harmonic oscillator, contributions of 1) a rigid rotor, 2) anharmonicity and 3) centrifugal distortion as well. The eigenenergies of this Morse potential depend on the vibrational constants  $\omega_e$  and  $\omega_e x_e$  as well as the rotational,  $B_v$ , and the centrifugal constant,  $D_v$ , and can be written as

$$E(v, J) = E_e + \omega_e \left( v + \frac{1}{2} \right) - \omega_e x_e \left( v + \frac{1}{2} \right)^2 + B_v J(J+1) - D_v J^2(J+1)^2 \quad (1.5.3)$$

with  $E_e$  the electronic energy of the molecular state. A more general function representing the diatomic molecule is given by the Dunham potential function [25]

$$E(v, J) = \sum_{i,j} Y_{i,j} \left( v + \frac{1}{2} \right)^i [J(J+1)]^j \quad (1.5.4)$$

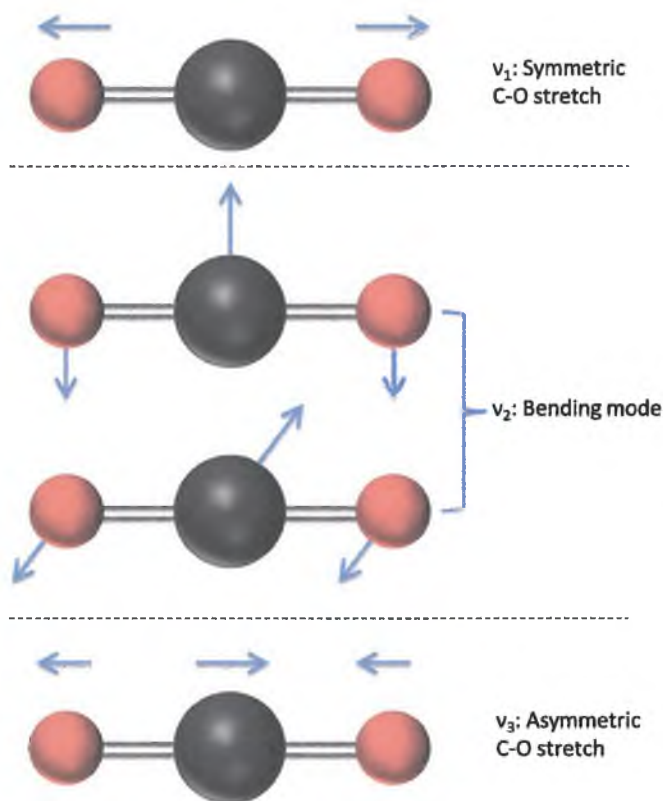


Figure 1.3: Three normal vibrational modes of  $\text{CO}_2$  [1, 26].

where  $Y_{i,j}$  are known as Dunham coefficients and represent fit parameters chosen such that the eigenenergies best reproduce the measured ones of rotational levels in vibrational states of the molecule. The constants given in Eq. 1.5.4 are related to the set of molecular coefficients of Eq. 1.5.3 by

$$Y_{10} = \omega_e, Y_{11} = -\alpha_e, Y_{01} = B_e, Y_{20} = -\chi_e \omega_e, Y_{02} = D_e \quad (1.5.5)$$

For polyatomic molecules consisting of  $N$  molecules, the nonlinear ones possess  $3N - 6$  normal vibrational modes, while linear molecules possess  $3N - 5$ . An example of a linear molecule is carbon dioxide ( $\text{CO}_2$ ), shown in Fig. 1.3, which demonstrates how the oxygen atoms can stretch and bend with respect to the carbon atom.  $\text{CO}_2$  has three vibrational modes: the symmetric stretch ( $\nu_1$ ), asymmetric stretch ( $\nu_3$ ), and a degenerate bending mode ( $\nu_2$ ) [1, 26].

The spectroscopic parameters given in Eq. 1.5.5 are unique properties, thus each molecule will have its unique set of vibrational energy levels. As can be

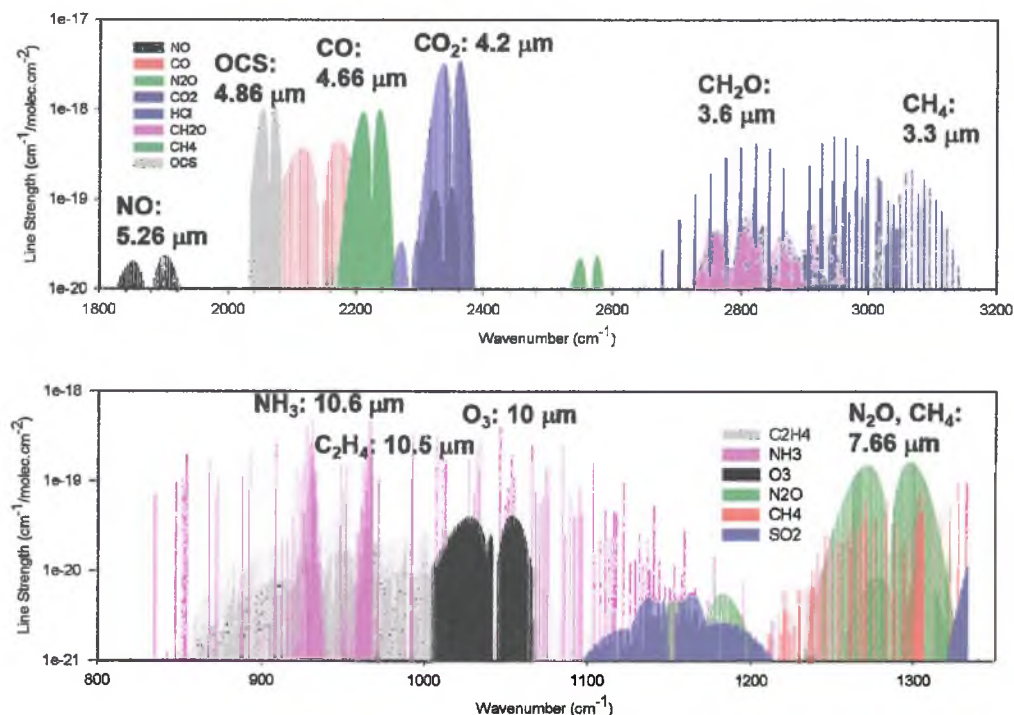


**Figure 1.4:** Line strengths of ro-vibrational transitions in the MIR of nitric oxide (NO), carbon monoxide (CO), nitrous oxide (N<sub>2</sub>O), carbon dioxide (CO<sub>2</sub>), hydrogen chloride (HCl), ammonia (NH<sub>3</sub>), methane (CH<sub>4</sub>), formaldehyde (CH<sub>2</sub>O), carbonyl sulfide (OCS), ethylene (C<sub>2</sub>H<sub>4</sub>), and ozone (O<sub>3</sub>) taken from HITRAN 2008 database [17, 19].

seen from Eq. 1.5.4, each chemical compound has a unique infrared absorption and emission spectrum due to the fundamental nature of the vibrational and rotational modes, its higher order shifts and its ro-vibrational interaction, just as each person has a unique set of fingerprints. These strong and unique absorption patterns emerge in the infrared, particularly in what is logically called the 'fingerprint region' (5000 cm<sup>-1</sup> to 500 cm<sup>-1</sup>, 2 – 20 μm). The fingerprint region involves molecular vibrations, usually bending motions, that are characteristic of the entire molecule or large fragments of the molecule. An overview of different molecules absorbing between 3 μm (3000 cm<sup>-1</sup>) and 12 μm (800 cm<sup>-1</sup>) is given in Fig. 1.4.

## 1.6 Mid-infrared light sources

Infrared radiation was discovered in the early 19<sup>th</sup> century by Fredrick William Herschel, while investigating the colors associated with heat from the sunlight [27]. He found that the temperature maximum was beyond the red light and thus discovered infrared radiation. Infrared spectroscopy can analyze samples in the liquid, solid and gas phase and can be combined with other devices for different sampling procedures. Due to limited availability, MIR spectroscopy is typically performed with a broadband source such as a Nernst glower, Globar, or Fourier transform infrared spectrometer to resolve the spectrum by wavelength. This provides the advantage of measuring a broadband sample absorption spectrum at once. To assure high selectivity, IR spectroscopic measurements can also be performed with a monochromatic infrared laser source with a narrow wavelength band and narrow line width. Ideally, lasers should operate stable at room temperature, since those, which require cryogenic cooling, are impractical for field measurements and miniaturization. To achieve a high sensitivity and spectral resolution in spectroscopic methods such as photoacoustic and cavity enhanced spectroscopy (see Chapter 3), a high optical power and a narrow laser line width are essential. Furthermore, the laser should have a large tuning range to perform multi-species and broadband molecular spectroscopy. MIR lasers provide a powerful output at their specific emission wavelength and thus potentially provide a high sensitivity. Presently available lasers vary strongly in their power output, line width, tunability, and spectral coverage. Figure 1.5 summarizes the spectral coverage of a number of MIR laser sources, which will be discussed in detail below.

### Gas lasers

In general, gas lasers operate by exciting a gas to a high-energy state using a DC discharge power through a gas as a pump. A very popular MIR laser is the CO<sub>2</sub> laser, which was first demonstrated in 1964 by Patel at the Bell Labs [28]. The emission wavelengths of gas lasers are based on the transition energies available in the gas of choice. CO<sub>2</sub> lasers are line tunable between 9 and 11  $\mu\text{m}$ , and are capable of emitting continuous powers in the kilowatts range. Because of their high power levels, CO<sub>2</sub> lasers are frequently used in power-demanding industrial applications like cutting and welding of metals and for sensitive trace gas detection [29]. Another commonly used MIR gas laser is the CO laser with typical output powers in the order of hundreds of Watts, which emits from

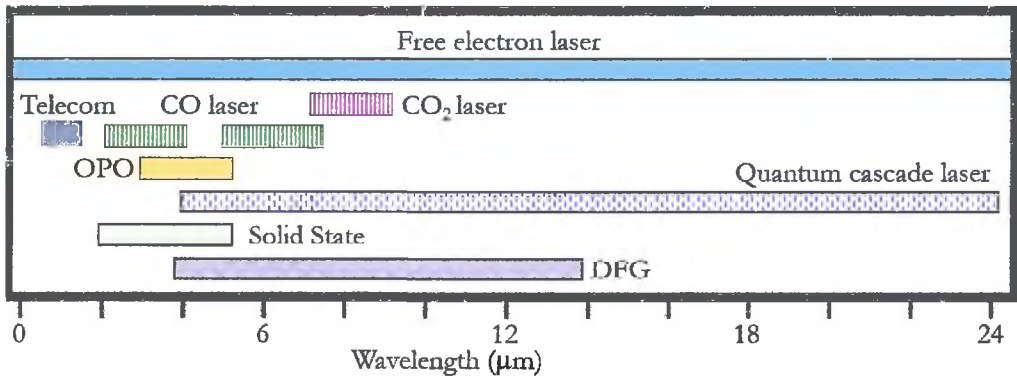


Figure 1.5: Overview of a selection of available laser sources in the MIR spectral region.

5 – 8  $\mu\text{m}$  utilizing fundamental CO transitions and which can be extended to discrete lines between 2,5 – 8  $\mu\text{m}$  using overtone vibrations [30, 31]. CO lasers need cryogenic cooling and therefore are difficult to use in field applications. Non-linear generation of infrared light provides an alternative.

### Coherent light sources based on nonlinear frequency generation

With optical parametric oscillators (OPO), a pump beam enters a nonlinear crystal and splits into two separate frequencies, whose sum equals that of the pump [32]. The key element of the OPO is a nonlinear periodic crystal, which is used to achieve a phase matching condition through a periodic structure. The period of the crystal is changed by varying its temperature, thus altering the ratio of the output wavelengths to provide wavelength tunability. The choice of the pump source and crystal transparency allows wavelengths from 1 – 5  $\mu\text{m}$  to be generated. Power outputs of up to 10 W average power are possible depending on the intensity of the pump beam and the conversion efficiency of the nonlinear crystal, capable of reaching line widths down to 10 kHz. To give an example of its spectroscopic abilities, a detection limit of 50 pptv ethane in nitrogen in 0,25 s at  $2997\text{ cm}^{-1}$  was demonstrated with cavity enhanced absorption spectroscopy as well as real-time breath sampling of methane and water within 0,1 s [32]. The disadvantages of OPOs are the dependency on powerful pump sources, the challenging tuning mechanism and its limited wavelength range.

Difference frequency generation is similar to an OPO, but here two single-frequency sources get mixed on a single pass through a nonlinear crystal to generate a tunable narrowband frequency at a third frequency equal to the difference between the two input frequencies. Wavelength tuning is accomplished by changing the crystal temperature or tuning of the pump and/or the signal laser frequency. With periodically poled nonlinear crystals (PPLN), the three frequencies can be phase-matched and permit the use of near-infrared diode or fiber lasers as pump lasers, making the system both compact and robust. The technique has been applied, for example, to the analysis of the chemical compositions of surgical smoke [33]. DFG lasers can operate at room temperature and generate sufficient cw-output powers to be useful in spectroscopic applications. The main limitation of the technique is the low conversion efficiency, resulting in maximum output power levels of the order of few milliwatts.

### Solid state lasers

Mid-infrared solid-state lasers use crystals or glasses as gain media doped with rare earth or transition-metal ions. A well known example is the Nd:YAG laser with its most common emission at 1064 nm. Solid state lasers are optically pumped in contrast to semiconductor lasers by either diode lasers or arc lamps [34] and emit mostly in the visible and near infrared region with several kilowatts output power. They can operate in cw- and pulse mode, have line widths of a few MHz [35] and are used in all sorts of applications including welding, cutting drilling and micro-processing. In spectroscopy, solid state lasers are used for intra-cavity spectroscopy [36] or noninvasive biomedical photoacoustics [37] using nanosecond pulses and millijoule pulse energy. Fiber lasers belong to this category and deliver high average output power, high beam quality, and broad wavelength tunability. Recently, they have been applied to the ultra-sensitive detection of acetylene, reaching detection limits of only 5 pptv in 10 s [38]. However, the generation of light can be a complex and costly process and solid state lasers only emit in the 1 – 3  $\mu\text{m}$  range.

### Free electron lasers

The free electron laser (FEL) uses a beam of relativistic electrons passing through a periodic, transverse magnetic field to produce coherent radiation. The name is somewhat misleading as the term 'laser' refers to optical amplification based on quantum stimulated emission of radiation, while in FELs, the electrons

move freely through a magnetic structure, hence the term 'free electron'. FELs can generate very high peak and average power, possess a broad tunability from the X-ray to the infrared region and have been applied to biomedical investigations [39] and to infrared absorption spectroscopy [40]. A MIR-FEL was upgraded to meet the standards of a medical laser and was serving as a surgical tool in ophthalmology and human neurosurgery [41]. Another application of IR FELs concerns the use in action spectroscopy as a way to measure vibrational spectra in highly diluted gas phase samples [42]. Still, FELs are most commonly incorporated into a facility and the sheer size and its costs make them unattractive for commercial use.

### Semiconductor lasers

1. Lead salt lasers generate MIR emission dependent on the bandgap energy of IV-VI materials. By varying the composition of these materials, emissions between 3 – 30  $\mu\text{m}$  have been achieved [43]. Typical power outputs reaching several tens of mW are produced. Lead salt lasers are capable of tuning over a few wavenumbers by temperature and have line widths of  $\sim 1$  MHz [43]. Because of the low thermal conductivity of those materials, cw operation requires cryogenic cooling. The typical output powers are of the order of hundreds of microwatts. Tuning occurs via injection current (tuning range tens of  $\text{cm}^{-1}$ ) and/or temperature ( $\sim 100 - 200$   $\text{cm}^{-1}$ ), but both mechanisms are not continuous. Lead salt diode lasers have been applied in scientific research [44], but are nowadays neither considered in research nor in industrial applications, because of multiple practical drawbacks such as cryogenic cooling, low power (100–500  $\mu\text{W}$ ) and change in characteristics with temperature cycling [30].
2. Antimonide semiconductor lasers are based on compositions of III-V elements, where the large number of possible alloys allows a variety of active regions and waveguide designs. Diode lasers based on antimonide have line widths up to  $\sim 100$  MHz and generate higher optical powers than lead-salt diode lasers. Antimonide-based diode lasers operate at short mid-infrared wavelengths between 2 and 3,3  $\mu\text{m}$  and can fill the gap in the diode laser spectrum between 1,7  $\mu\text{m}$  and the quantum cascade laser around 4  $\mu\text{m}$ . They are capable of cw operation at room temperatures with output powers of  $\sim 500$  mW [45, 46] and have been used among others to perform photoacoustic spectroscopy of methane [47].

3. Interband cascade lasers (ICLs) are semiconductor lasers, which combine diode lasers with a cascade scheme, in which electron and hole transitions occur between adjacent layers of conduction and valence bands, generating multiple photons. The ICL concept has been first proposed by Yang in 1995 [48] and ICLs have performed best around 3 – 5,6  $\mu\text{m}$ , where cw-operation is possible [49] with an output power in excess of 20 mW. A recently developed distributed feedback ICL emitted up to 27 mW in a single spectral mode at 3,79  $\mu\text{m}$  at 40°C and 1 mW at 80°C [50]. Spectroscopic applications of ICLs include the detection of formaldehyde [51] at room temperature and a distributed-feedback ICL designed for the detection of methane was aboard the Curiosity Rover that was sent to explore the environment of Mars [52]. ICLs are hybrids between normal diode lasers and quantum cascade lasers, the latter will be briefly explained below and in more detail in Chapter 2.
4. Quantum cascade lasers (QCLs) are the only MIR laser source able to cover almost the entire MIR with a single material system. Its operation is based on quantum well heterostructures and tunneling between them, thus its performance strongly depends on the design of tens of quantum layers. The structure of a QCL was originally proposed in 1971 by Kazarinov and Suris [53] and was realized for the first time by Faist et. al. [13] at the Bell Laboratories in 1994. QCLs are the only semiconductor lasers to operate at room temperature in both the MIR and far-IR and are particularly well adapted for chemical spectroscopy in both medical [54, 55] and atmospheric [56] applications. The next Chapter 2 of this thesis is devoted to the operation principles and current developments of QCLs.

## 1.7 The scope of this thesis

This thesis presents the design and application of mid-infrared and near-infrared trace gas sensors for the analysis of medically, environmentally and biologically relevant molecules. For that purpose, laser-based spectrometers were developed with high detectability, accuracy, selectivity and simplicity. Chapter 2 gives a brief account on the operating principles of the QCL and its applications. Chapter 3 reviews the basic principles of absorption spectroscopy, whereas Chapter 4 presents the development of an off-axis integrated cavity output spectroscopy (OA-ICOS) spectrometer for the *in-situ* detection of ethylene.

The following chapter, Chapter 5, shows the possibilities of enhancing the ICOS technique by the re-injection of light into the optical cavity. Chapter 6 describes the development of an external cavity quantum cascade laser and its application is shown in Chapter 7, which deals with the influence of ethanol on the measurement of breath acetone. As one particular goal was to build a user-friendly and compact, yet highly sensitive NICE-OHMS spectrometer suitable for trace species detection, the last two chapters of this thesis deal with aspects of NICE-OHMS. Chapter 8 contains a detailed description of the NICE-OHMS method. The final chapter, Chapter 9, shows the development of a NICE-OHMS setup in combination with an external cavity diode laser for the detection of methane, acetylene and hydrogen cyanide.

# References

- [1] W. Demtröder, *Laserspektroskopie*, vol. 4. Springer, 2011.
- [2] T. Hänsch, I. Shahin, and A. Schawlow, "Optical resolution of the Lamb shift in atomic hydrogen by laser saturation spectroscopy," *Nature*, vol. 235, no. 56, pp. 63–65, 1972.
- [3] T. Hänsch and B. Couillaud, "Laser frequency stabilization by polarization spectroscopy of a reflecting reference cavity," *Optics Communications*, vol. 35, no. 3, pp. 441–444, 1980.
- [4] R. Drever, J. L. Hall, F. Kowalski, J. Hough, G. Ford, A. Munley, and H. Ward, "Laser phase and frequency stabilization using an optical resonator," *Applied Physics B*, vol. 31, no. 2, pp. 97–105, 1983.
- [5] M. H. Anderson, J. R. Ensher, M. R. Matthews, C. E. Wieman, and E. A. Cornell, "Observation of Bose-Einstein condensation in a dilute atomic vapor," *Science*, vol. 269, no. 5221, pp. 198–201, 1995.
- [6] J. Röpcke, P. Davies, N. Lang, A. Rousseau, and S. Welzel, "Applications of quantum cascade lasers in plasma diagnostics: A review," *Journal of Physics D: Applied Physics*, vol. 45, no. 42, p. 423001, 2012.
- [7] U. Willer, M. Saraji, A. Khorsandi, P. Geiser, and W. Schade, "Near-and mid-infrared laser monitoring of industrial processes, environment and security applications," *Optics and Lasers in Engineering*, vol. 44, no. 7, pp. 699–710, 2006.
- [8] C. S. Patterson, L. C. McMillan, C. Longbottom, G. M. Gibson, M. J. Padgett, and K. D. Skeldon, "Portable optical spectroscopy for accurate analysis of ethane in exhaled breath," *Measurement Science and Technology*, vol. 18, no. 5, p. 1459, 2007.
- [9] N. Kröger, A. Egl, M. Engel, N. Gretz, K. Haase, I. Herpich, B. Kränzlin, S. Neudecker, A. Pucci, A. Schönhals, *et al.*, "Quantum cascade laser-based hyperspectral imaging of biological tissue," *Journal of Biomedical Optics*, vol. 19, no. 11, p. 111607, 2014.
- [10] S. Spuler, M. Linne, A. Sappey, and S. Snyder, "Development of a cavity ringdown laser absorption spectrometer for detection of trace levels of mercury," *Applied Optics*, vol. 39, no. 15, pp. 2480–2486, 2000.
- [11] M. Todd, R. Provencal, T. Owano, B. Paldus, A. Kachanov, K. Vodopyanov, M. Hunter, S. Coy, J. Steinfeld, and J. Arnold, "Application of mid-infrared cavity-ringdown spectroscopy to trace explosives vapor detection using a broadly tunable (6–8  $\mu\text{m}$ ) optical parametric oscillator," *Applied Physics B*, vol. 75, no. 2-3, pp. 367–376, 2002.
- [12] R. Hall, G. Fenner, J. Kingsley, T. Soltys, and R. Carlson, "Coherent light emission from Ga-As junctions," *Phys. Rev. Lett.*, vol. 9, p. 366, 1962.
- [13] J. Faist, F. Capasso, D. L. Sivco, C. Sirtori, A. L. Hutchinson, and A. Y. Cho, "Quantum cascade laser," *Science*, vol. 264, no. 5158, pp. 553–556, 1994.

- [14] R. Mears, L. Reekie, S. Poole, and D. Payne, "Neodymium-doped silica single-mode fibre lasers," *Electronics Letters*, vol. 21, no. 17, pp. 738–740, 1985.
- [15] S. M. Cristescu, J. Mandon, D. Arslanov, J. De Pessemier, C. Hermans, and F. J. Harren, "Current methods for detecting ethylene in plants," *Annals of Botany*, vol. 111, no. 3, pp. 347–360, 2013.
- [16] S. Cristescu, D. Marchenko, J. Mandon, K. Hebelstrup, G. Griffith, L. Mur, and F. Harren, "Spectroscopic monitoring of NO traces in plants and human breath: Applications and perspectives," *Applied Physics B*, vol. 110, no. 2, pp. 203–211, 2013.
- [17] T. H. Risby and F. K. Tittel, "Current status of midinfrared quantum and interband cascade lasers for clinical breath analysis," *Optical Engineering*, vol. 49, no. 11, p. 111123, 2010.
- [18] Wikipedia, "[Accuracy and precision](#)".
- [19] L. S. Rothman, I. E. Gordon, A. Barbe, D. C. Benner, P. F. Bernath, M. Birk, V. Boudon, L. R. Brown, A. Campargue, J. P. Champion, *et al.*, "The HITRAN 2008 molecular spectroscopic database," *Journal of Quantitative Spectroscopy and Radiative Transfer*, vol. 110, no. 9, pp. 533–572, 2009.
- [20] F. Rohart, G. Wlodarczak, J. M. Colmont, G. Cazzoli, L. Dore, and C. Puzzarini, "Galatry versus speed-dependent voigt profiles for millimeter lines of O<sub>3</sub> in collision with N<sub>2</sub> and O<sub>2</sub>," *Journal of Molecular Spectroscopy*, vol. 251, no. 1, pp. 282–292, 2008.
- [21] N. Ngo, H. Tran, R. Gamache, and J. Hartmann, "Pressure effects on water vapour lines: Beyond the Voigt profile," *Philosophical Transactions of the Royal Society A: Mathematical, Physical and Engineering Sciences*, vol. 370, no. 1968, pp. 2495–2508, 2012.
- [22] W. Demtröder, *Atoms, molecules and photons*. Springer, 2008.
- [23] M. Born and R. Oppenheimer, "Die Quantentheorie der Moleküle," *Annalen der Physik*, vol. 389, no. 20, pp. 457–484, 1927.
- [24] P. M. Morse, "Diatomic molecules according to the wave mechanics. II. Vibrational levels," *Physical Review*, vol. 34, no. 1, p. 57, 1929.
- [25] J. Dunham, "The energy levels of a rotating vibrator," *Physical Review*, vol. 41, no. 6, p. 721, 1932.
- [26] Y. Itikawa, "Cross sections for electron collisions with carbon dioxide," *Journal of Physical and Chemical Reference Data*, vol. 31, no. 3, pp. 749–768, 2002.
- [27] M. Rowan-Robinson, *Night Vision: Exploring the Infrared Universe*. Cambridge University Press, 2013.
- [28] C. K. N. Patel, "Continuous-wave laser action on vibrational-rotational transitions of CO<sub>2</sub>," *Physical Review*, vol. 136, no. 5A, p. A1187, 1964.

- [29] S. Cristescu, S. Persijn, S. te Lintel Hekkert, and F. Harren, "Laser-based systems for trace gas detection in life sciences," *Applied Physics B*, vol. 92, no. 3, pp. 343–349, 2008.
- [30] R. Curl and F. Tittel, "Tunable infrared laser spectroscopy," *Annual Reports Section "C" (Physical Chemistry)*, vol. 98, pp. 219–272, 2002.
- [31] U. Merker, P. Engels, F. Madeja, M. Havenith, and W. Urban, "High-resolution CO-laser sideband spectrometer for molecular-beam optothermal spectroscopy in the 5–6.6  $\mu\text{m}$  wavelength region," *Review of Scientific Instruments*, vol. 70, no. 4, pp. 1933–1938, 1999.
- [32] D. D. Arslanov, M. Spunei, J. Mandon, S. M. Cristescu, S. T. Persijn, and F. J. Harren, "Continuous-wave optical parametric oscillator based infrared spectroscopy for sensitive molecular gas sensing," *Laser & Photonics Reviews*, vol. 7, no. 2, pp. 188–206, 2013.
- [33] M. Gianella and M. W. Sigrist, "Chemical analysis of surgical smoke by infrared laser spectroscopy," *Applied Physics B*, vol. 109, no. 3, pp. 485–496, 2012.
- [34] M. Doroshenko, H. Jelínková, P. Koranda, J. Šulc, T. Basiev, V. Osiko, V. Komar, A. Gerasimenko, V. Puzikov, V. Badikov, *et al.*, "Tunable mid-infrared laser properties of  $\text{Cr}_2^+$ : ZnMgSe and  $\text{Fe}_2^+$ : ZnSe crystals," *Laser Physics Letters*, vol. 7, no. 1, p. 38, 2010.
- [35] S. Mirov, V. Fedorov, I. Moskalev, D. Martyshkin, and C. Kim, "Progress in  $\text{Cr}_2^+$  and  $\text{Fe}_2^+$  doped mid-IR laser materials," *Laser & Photonics Reviews*, vol. 4, no. 1, pp. 21–41, 2010.
- [36] H. Pask, R. Mildren, and J. Piper, "Optical field dynamics in a wavelength-versatile, all-solid-state intracavity cascaded pulsed Raman laser," *Applied Physics B*, vol. 93, no. 2–3, pp. 507–513, 2008.
- [37] M. V. Bogdanovich, V. V. Kabanov, G. I. Ryabtsev, A. G. Ryabtsev, and Y. V. Lebiadok, "High-performance LD-pumped solid-state lasers for range finding and spectroscopy," in *XIX International Symposium on High-Power Laser Systems and Applications*, p. 86770X, International Society for Optics and Photonics, 2013.
- [38] P. Ehlers, I. Silander, J. Wang, A. Foltynowicz, and O. Axner, "Fiber-laser-based noise-immune cavity-enhanced optical heterodyne molecular spectrometry incorporating an optical circulator," *Optics Letters*, vol. 39, no. 2, pp. 279–282, 2014.
- [39] G. S. Edwards, "Mechanisms for soft-tissue ablation and the development of alternative medical lasers based on investigations with mid-infrared free-electron lasers," *Laser & Photonics Reviews*, vol. 3, no. 6, pp. 545–555, 2009.
- [40] T. Masaki, Y. Inouye, and S. Kawata, "Submicron-resolving infrared absorption spectroscopy and analysis in fingerprint region utilizing a free electron laser," *Chemical Physics Letters*, vol. 417, no. 4, pp. 410–413, 2006.
- [41] R. J. Shah, J. H. Shen, and K. M. Joos, "Endoscopic free electron laser technique development for minimally invasive optic nerve sheath fenestration," *Lasers in Surgery and Medicine*, vol. 39, no. 7, pp. 589–569, 2007.

- [42] M. Haertelt, J. T. Lyon, P. Claes, J. de Haeck, P. Lievens, and A. Fielicke, "Gas-phase structures of neutral silicon clusters," *Journal of Chemical Physics*, vol. 136, no. 6, p. 064301, 2012.
- [43] M. Tacke, "New developments and applications of tunable IR lead salt lasers," *Infrared Physics & Technology*, vol. 36, no. 1, pp. 447–463, 1995.
- [44] P. Werle, F. Slemr, M. Gehrtz, and C. Bräuchle, "High frequency modulation spectroscopy with a lead salt diode laser," in *Monitoring of Gaseous Pollutants by Tunable Diode Lasers*, p. 121, Springer, 1989.
- [45] J. Kim, L. Shterengas, R. Martinelli, and G. Belenky, "High-power room-temperature continuous wave operation of 2.7 and 2.8  $\mu\text{m}$  in (Al) GaAsSb/GaSb diode lasers," *Applied Physics Letters*, vol. 83, no. 10, pp. 1926–1928, 2003.
- [46] T. Hosoda, G. Kipshidze, G. Tsvi, L. Shterengas, and G. Belenky, "Type-I GaSb-based laser diodes operating in 3.1 – 3.3  $\mu\text{m}$  wavelength range," *Photonics Technology Letters, IEEE*, vol. 22, no. 10, pp. 718–720, 2010.
- [47] M. Jahjah, A. Vicet, and Y. Rouillard, "A QEPAS based methane sensor with a 2.35  $\mu\text{m}$  antimonide laser," *Applied Physics B*, vol. 106, no. 2, pp. 483–489, 2012.
- [48] R. Q. Yang, "Infrared laser based on intersubband transitions in quantum wells," *Superlattices and Microstructures*, vol. 17, no. 1, p. 77, 1995.
- [49] W. W. Bewley, C. L. Canedy, C. S. Kim, M. Kim, C. D. Merritt, J. Abell, I. Vurgaftman, and J. R. Meyer, "Continuous-wave interband cascade lasers operating above room temperature at  $\lambda = 4.7 - 5.6 \mu\text{m}$ ," *Optics Express*, vol. 20, no. 3, pp. 3235–3240, 2012.
- [50] C. Kim, M. Kim, J. Abell, W. Bewley, C. Merritt, C. Canedy, I. Vurgaftman, and J. Meyer, "Mid-infrared distributed-feedback interband cascade lasers with continuous-wave single-mode emission to 80°C," *Applied Physics Letters*, vol. 101, no. 6, p. 061104, 2012.
- [51] S. Lundqvist, P. Kluczynski, R. Weih, M. von Edlinger, L. Nähle, M. Fischer, A. Bauer, S. Höfling, and J. Koeth, "Sensing of formaldehyde using a distributed feedback interband cascade laser emitting around 3493 nm," *Applied Optics*, vol. 51, no. 25, pp. 6009–6013, 2012.
- [52] Y. Qiu *et al.*, "Distributed feedback mid-IR interband cascade lasers at thermoelectric cooler temperatures," *IEEE Journal of Selected Topics in Quantum Electronics*, vol. 13, no. 5, pp. 1074–1078, 2007.
- [53] R. Kazarinov and R. Sui-is, "Possibility of the amplification of electromagnetic waves in a semiconductor with a superlattice," *Soviet Physics-Semiconductors*, vol. 5, no. 4, 1971.
- [54] A. A. Kosterev, A. L. Malinovsky, F. K. Tittel, C. Gmachl, F. Capasso, D. L. Sivco, J. N. Baillargeon, A. L. Hutchinson, and A. Y. Cho, "Cavity ringdown spectroscopic detection of nitric oxide with a continuous-wave quantum-cascade laser," *Applied Optics*, vol. 40, no. 30, pp. 5522–5529, 2001.

- [55] L. Menzel, A. Kosterev, R. Curl, F. Tittel, C. Gmachl, F. Capasso, D. Sivco, J. Baillargeon, A. Hutchinson, A. Cho, *et al.*, "Spectroscopic detection of biological NO with a quantum cascade laser," *Applied Physics B*, vol. 72, no. 7, pp. 859–863, 2001.
- [56] A. A. Kosterev, R. F. Curl, F. K. Tittel, C. Gmachl, F. Capasso, D. L. Sivco, J. N. Baillargeon, A. L. Hutchinson, and A. Y. Cho, "Effective utilization of quantum-cascade distributed-feedback lasers in absorption spectroscopy," *Applied Optics*, vol. 39, no. 24, pp. 4425–4430, 2000.



## Chapter 2: Quantum cascade laser

### 2.1 Introduction

**A**MONG THE MID-INFRARED (MIR) SOURCES, quantum cascade lasers (QCLs) present an ideal light source for chemical sensing due to their compactness, high power, narrow line width and high spectral density across the MIR region. In conventional semiconductor lasers, electronic transitions occur by electron-hole recombination between the valence and conduction band, making the emission wavelength dependent on the bandgap of the material. In a QCL, a quantum heterostructure is designed to create a transition between states within a given quantum well, which results in an emission wavelength dependent on the energies of the states rather than the bandgap energy of the material. Fig. 2.1 shows the tunneling process of an electron injected into the gain region. This electron enters the heterostructure through an injector region at the left and is injected into level 3. The same electron responsible for the emission of the photon tunnels into the next quantum well (level 2) and as a result, light is emitted. Population inversion is achieved between level 3 and 2 by fast tunneling from level 2 to level 1,

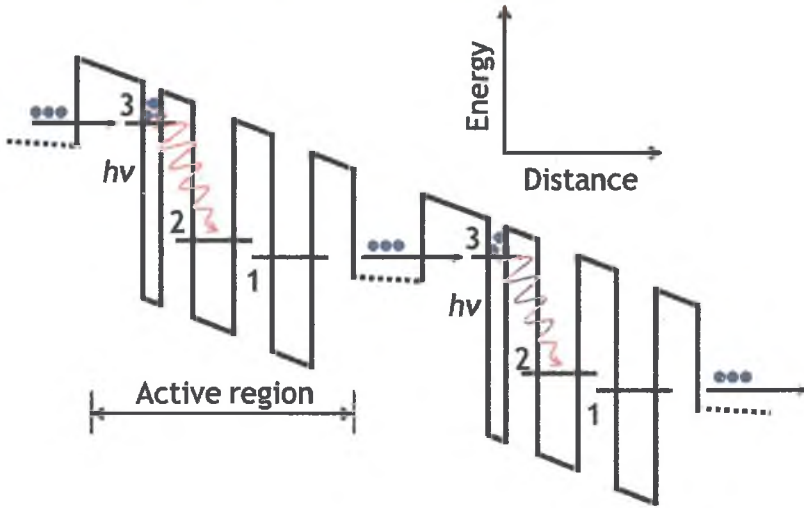


Figure 2.1: Band-structure of a typical QC laser [1].

after which the electron is coupled into the next injection band. This process is repeated for many periods in the lattice, providing a cascade effect (hence the name) and allowing a single electron to produce multiple photons, increasing the output power of the laser. Different emission wavelengths are achieved by engineering different well depths, where the thickness of the material layers is adjusted. The layer thicknesses can be controlled with atomic precision by epitaxial growth using molecular beam epitaxy techniques.

QCLs can be classified in two types: 1) Fabry-Perot and 2) distributed feedback (DFB) devices, where the latter includes a periodic structure, which acts as a distributed reflector to achieve single-frequency operation. Currently, most QCLs are fabricated as DFB type, as the narrow line width and room temperature operation is beneficial, in particular for gas sensing applications. However, also Fabry-Perot lasers are attractive for spectroscopic applications due to their broad tunability, but here, a wavelength selective element (see Section 2.2) is needed to achieve single-mode operation. QCLs can operate in pulsed and continuous wave (cw) mode and have reached several hundreds of mW output power in cw-mode and Watt level peak powers. Most quantum cascade lasers emit mid-infrared (MIR) light, yet compact and simple devices have demonstrated Terahertz waves [2]. While the overall performance of QCLs is improving steadily over the years, the wavelength range covered by QCLs is also expanding. Improvements in the long wavelength range have been gained

with optimizations of active core designs [3, 4], waveguide structures [5] and fabrication techniques. Current research centers around the extension of QCLs into the near infrared [6] and the development of frequency comb QCLs [7].

In summary, QCLs could become tools with a great impact on our society due to their versatility and suitability for many applications. In the next subsections, several tuning methods and applications of QCLs are presented.

## 2.2 Tuning methods

Tuning of a QCL wavelength can be achieved in three ways: 1) Temperature tuning of the substrate, which is a slow process that can tune the laser frequency  $0,1 - 0,3 \text{ cm}^{-1}/\text{K}$ ; 2) through a faster process of laser bias current variation that can tune  $< 7 \text{ cm}^{-1}$  [8–10] and 3) using a wavelength selective element. For DFB-QCLs, heating the chip changes the spacing of the periodic structure and the refractive index of the chip, thus the output wavelength. This methods can be used with both pulsed and cw-mode lasers. Depending on the operational mode of the QCL, different current variation methods can be applied. In cw-mode, the laser simply gets directly driven by a constant current, whereas in pulsed mode, two operating principles are possible. The first is the inter-pulse method, which

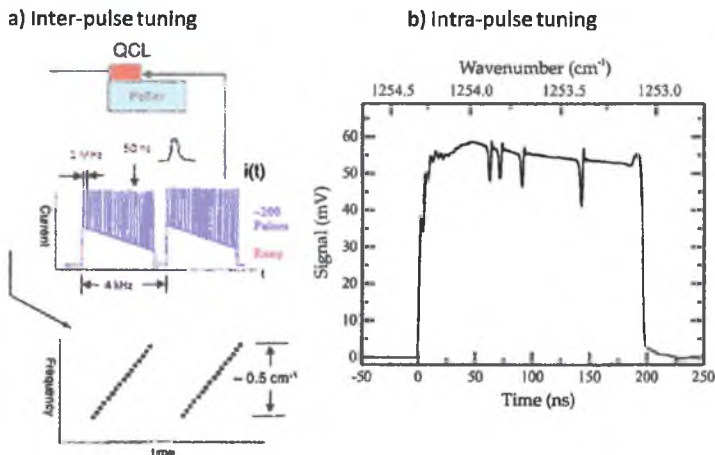


**Figure 2.2:** Schematic of the inter-pulse (panel (a)) using a puls repetition rate of 1 MHz and a period of 4 kHz with 50 ns pulses, which results in a total scanning range of  $0,5 \text{ cm}^{-1}$ . Panel (b) shows a typical scan taken with the intra-pulse tuning method with a puls width of 200 ns, resulting a scanning range of  $\sim 1 \text{ cm}^{-1}$ .

combines ultra-short current pulses to the laser with a slowly varying current, scanning the laser wavelength through the spectroscopic transition of interest (Fig. 2.2(a)). Using this technique, a spectrum is acquired in tens of milliseconds. This method was pioneered by Namjou et al. [11], using a 1 MHz pulse train with a duration of 11 ns superimposed on a sub-threshold current ramp such that each pulse had a slightly different wavelength. Although the inter-pulse methods give narrow laser line widths [12], successive scans need to be added in order to cover a larger spectral range than the typical  $0.2 \text{ cm}^{-1}$ . This has the disadvantage of introducing shot-to-shot noise between laser pulses, which affects subsequent points in a recorded spectra. Also, pulsing the laser in this way results in a frequency chirp, which is the change in frequency over time due to temperature change, broadening the laser line width and reducing the spectral resolution.

The second, alternative approach is intra-pulse spectroscopy (Fig. 2.2(b)), which uses, like inter-pulse, the laser in pulsed mode to enable room-temperature operation [13], but prolongs the pulse up to several microseconds. The spectral feature of interest is then measured during the frequency sweep due to the temperature change of the chip. Pulse widths up to several microseconds are used with large pulse amplitudes to produce scanning ranges of typically between 4 and  $6 \text{ cm}^{-1}$  wide. The spectral resolution in this case is defined by the instantaneous line width of the laser as it sweeps in wavelength. Previous research showed that the spectral resolution of a QCL, which uses the inter-pulse method, is similar to one where the intra-pulse method is used [14].

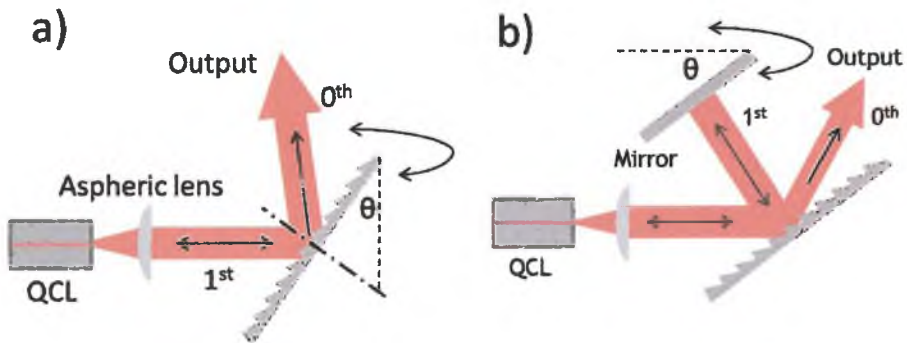


Figure 2.3: (a) Littrow and (b) Littman-Metcalf external cavity configuration. Black arrows indicate the directions of propagation.

DFB-QCLs using the above described tuning mechanisms have limited tunability and only an array of them is capable of achieving a wide tuning range [15]. Currently, broadband gain chips are easy and cheap to manufacture and allow the use of an external grating configuration for wavelength tuning and control. External cavity QCLs (EC-QCLs) thus significantly increase the tuning range of the laser compared to DFB-QCLs and render them of substantial interest for sensing applications. First demonstrated by Luo et al., frequency selective feedback is typically achieved via diffraction gratings in either the Littrow (Fig. 2.3(a)) [16, 17] or Littman–Metcalf configuration (Fig. 2.3(b)) [18, 19]. In the Littrow setup, the first-order diffracted beam from the grating is fed back into the laser chip, while the directly reflected light forms the output beam. This particularly simple and effective configuration has the advantages of easy alignment and providing a strong feedback, since light is diffracted only once by the grating. Coarse tuning is achieved by rotating the grating, which has the disadvantage of displacing the output beam as well. Currently, tuning ranges of over  $400\text{ cm}^{-1}$  for pulsed and  $250\text{ cm}^{-1}$  for cw-EC-QCLs in the Littrow configuration have been reported [20, 21].

The Littman–Metcalf configuration uses a grating close to the grazing angle with the first-order diffracted beam reflected back to the grating and the laser by an additional mirror. Coarse tuning is usually achieved by rotating the mirror, since it allows the zero-order direction to be unchanged such that it can be used for extraction. Compared to the Littrow configuration, the resulting laser light has a narrower line width due to the double pass on the grating, but it requires a larger grating, an additional mirror and has the drawback of lower output efficiency.

## 2.3 Applications of QCLs in laser-based spectroscopy

As mentioned in Section 1.5, the MIR wavelength region is very important for absorption spectroscopy, since molecules have their strongest vibrational and ro-vibrational transitions in this wavelength region. In addition, there are two atmospheric windows present ( $3 - 5\text{ }\mu\text{m}$  and  $8 - 14\text{ }\mu\text{m}$ ), which allow long-distance transmission of light at the appropriate wavelengths in the atmosphere due to weak water transitions. QCL-based sensing is suitable for applications that require narrow line width, continuous wave single-mode operation, compact devices, fast response time and broad tunability. These aspects combined with the extremely high sensitivity (pptv-level) achieved

with absorption techniques opens up a wide range of applications in the MIR. QCL-based molecular sensing has been applied to various fields, for example air pollution monitoring [22, 23], where ozone was measured with a sensitivity of 150 ppbv during the 2008 Olympic Games in Beijing, breath analysis for ammonia detection with a sensitivity of 6 ppbv in 1 s [24, 25], the detection of explosive and hazardous materials at distances between 2 and 5 m [26] or industrial process monitoring [27]. Sensitive detection of molecular gases with QCLs has been achieved with photoacoustic spectroscopy [28–30], demonstrating sub-ppbv level detection of formaldehyde. QCLs were used with quartz-enhanced photoacoustic spectroscopy [31], probing a methanol absorption line at  $131\text{ cm}^{-1}$  with a sensitivity of 7 ppmv in 4 s. Demonstration of QCLs with integrated cavity output spectroscopy showed a detection limit of 0,7 ppb of NO and was applied to breath analysis [32]. QCLs have also been applied to gas sensing for transmission spectroscopy including applications such as atmospheric monitoring [33], cigarette smoke analysis [34], and monitoring ethylene for vehicle emission analysis [35]. Because EC-QCLs have a large frequency tuning range, they enable multi-species detection and have recently been applied to breath analysis of  $\text{CO}_2$  isotopologues [36] and to atmospheric transport studies for measurements of perfluorocarbons [37]. The field of telecommunications offers possibilities for the use of QCLs as well. An optical data link using a high-speed modulated, liquid nitrogen-cooled QCL has been established over a distance of 70 m [38] and in free space between two buildings, separated by 350 m [39]. In this thesis, the application of a pulsed QCL for the detection of ethylene in fruit storage will be presented (Chapter 4), together with the development of an EC-QCL (Chapter 6) for breath analysis of acetone (Chapter 7).

- [1] G. Hancock, D. Weidmann, G. Ritchie, J. P. van Helden, and R. Walker, "Applications of midinfrared quantum cascade lasers to spectroscopy," *Optical Engineering*, vol. 49, no. 11, p. 111121, 2010.
- [2] M. A. Belkin, F. Capasso, A. Belyanin, D. L. Sivco, A. Y. Cho, D. C. Oakley, C. J. Vineis, and G. W. Turner, "Terahertz quantum-cascade-laser source based on intracavity difference-frequency generation," *Nature Photonics*, vol. 1, no. 5, pp. 288–292, 2007.
- [3] R. Colombelli, F. Capasso, C. Gmachl, A. L. Hutchinson, D. L. Sivco, A. Tredicucci, M. C. Wanke, A. M. Sergent, and A. Y. Cho, "Far-infrared surface-plasmon quantum-cascade lasers at 21.5  $\mu\text{m}$  and 24  $\mu\text{m}$  wavelengths," *Applied Physics Letters*, vol. 78, no. 18, pp. 2620–2622, 2001.
- [4] X. Huang, W. O. Charles, and C. Gmachl, "Temperature-insensitive long-wavelength ( $\lambda = 14 \mu\text{m}$ ) quantum cascade lasers with low threshold," *Optics Express*, vol. 19, no. 9, pp. 8297–8302, 2011.
- [5] X. Huang, Y. Chiu, W. O. Charles, and C. Gmachl, "Ridge-width dependence of the threshold of long wavelength ( $\lambda = 14 \mu\text{m}$ ) quantum cascade lasers with sloped and vertical sidewalls," *Optics Express*, vol. 20, no. 3, pp. 2539–2547, 2012.
- [6] D. Guo, H. Cai, M. A. Talukder, X. Chen, A. M. Johnson, J. B. Khurgin, and F.-S. Choa, "Near-infrared induced optical quenching effects on mid-infrared quantum cascade lasers," *Applied Physics Letters*, vol. 104, no. 25, p. 251102, 2014.
- [7] A. Hugi, G. Villares, S. Blaser, H. Liu, and J. Faist, "Mid-infrared frequency comb based on a quantum cascade laser," *Nature*, vol. 492, no. 7428, pp. 229–233, 2012.
- [8] F. Xie, C. Caneau, H. P. LeBlanc, N. J. Visovsky, S. Coleman, L. C. Hughes, and C. E. Zah, "Room temperature cw operation of mid-IR distributed feedback quantum cascade lasers for  $\text{CO}_2$ ,  $\text{N}_2\text{O}$  and  $\text{NO}$  gas sensing," *Selected Topics in Quantum Electronics, IEEE Journal of*, vol. 18, no. 5, pp. 1605–1612, 2012.
- [9] Y. Yao, A. J. Hoffman, and C. Gmachl, "Mid-infrared quantum cascade lasers," *Nature Photonics*, vol. 6, no. 7, pp. 432–439, 2012.
- [10] J. Zhang, F. Liu, S. Tan, D. Yao, L. Wang, L. Li, J. Liu, and Z. Wang, "High-performance uncooled distributed-feedback quantum cascade laser without lateral regrowth," *Applied Physics Letters*, vol. 100, no. 11, p. 112105, 2012.
- [11] K. Namjou, S. Cai, E. Whittaker, J. Faist, C. Gmachl, F. Capasso, D. Sivco, and A. Cho, "Sensitive absorption spectroscopy with a room-temperature distributed-feedback quantum-cascade laser," *Optics Letters*, vol. 23, no. 3, pp. 219–221, 1998.

- [12] A. A. Kosterev, F. K. Tittel, C. Gmachl, F. Capasso, D. L. Sivco, J. N. Baillargeon, A. L. Hutchinson, and A. Y. Cho, "Trace-gas detection in ambient air with a thermoelectrically cooled, pulsed quantum-cascade distributed feedback laser," *Applied Optics*, vol. 39, no. 36, pp. 6866–6872, 2000.
- [13] E. Normand, M. McCulloch, G. Duxbury, and N. Langford, "Fast, real-time spectrometer based on a pulsed quantum-cascade laser," *Optics Letters*, vol. 28, no. 1, pp. 16–18, 2003.
- [14] G. Duxbury, N. Langford, M. T. McCulloch, and S. Wright, "Quantum cascade semiconductor infrared and far-infrared lasers: From trace gas sensing to non-linear optics," *Chemical Society Reviews*, vol. 34, no. 11, pp. 921–934, 2005.
- [15] B. G. Lee, M. A. Belkin, R. Audet, J. MacArthur, L. Diehl, C. Pflügl, F. Capasso, D. C. Oakley, D. Chapman, A. Napoleone, *et al.*, "Widely tunable single-mode quantum cascade laser source for mid-infrared spectroscopy," *Applied Physics Letters*, vol. 91, no. 23, p. 231101, 2007.
- [16] A. Arnold, J. Wilson, and M. Boshier, "A simple extended-cavity diode laser," *Review of Scientific Instruments*, vol. 69, no. 3, pp. 1236–1239, 1998.
- [17] L. Ricci, M. Weidemüller, T. Esslinger, A. Hemmerich, C. Zimmermann, V. Vuletic, W. König, and T. W. Hänsch, "A compact grating-stabilized diode laser system for atomic physics," *Optics Communications*, vol. 117, no. 5, pp. 541–549, 1995.
- [18] K. Harvey and C. Myatt, "External-cavity diode laser using a grazing-incidence diffraction grating," *Optics Letters*, vol. 16, no. 12, pp. 910–912, 1991.
- [19] M. C. Phillips, T. L. Myers, M. D. Wojcik, and B. D. Cannon, "External cavity quantum cascade laser for quartz tuning fork photoacoustic spectroscopy of broad absorption features," *Optics Letters*, vol. 32, no. 9, pp. 1177–1179, 2007.
- [20] A. Hugi, R. Terazzi, Y. Bonetti, A. Wittmann, M. Fischer, M. Beck, J. Faist, and E. Gini, "External cavity quantum cascade laser tunable from 7.6 to 11.4  $\mu\text{m}$ ," *Applied Physics Letters*, vol. 95, no. 6, p. 061103, 2009.
- [21] R. Maulini, A. Mohan, M. Giovannini, J. Faist, and E. Gini, "External cavity quantum-cascade laser tunable from 8.2 to 10.4  $\mu\text{m}$  using a gain element with a heterogeneous cascade," *Applied Physics Letters*, vol. 88, no. 20, p. 201113, 2006.
- [22] D. Weidmann, F. Tittel, T. Aellen, M. Beck, D. Hofstetter, J. Faist, and S. Blaser, "Mid-infrared trace-gas sensing with a quasi-continuous-wave peltier-cooled distributed feedback quantum cascade laser," *Applied Physics B*, vol. 79, no. 7, pp. 907–913, 2004.
- [23] A. P. Michel, P. Q. Liu, J. K. Yeung, P. Corrigan, M. L. Baeck, Z. Wang, T. Day, F. Moshary, C. Gmachl, and J. A. Smith, "Quantum cascade laser open-path system for remote sensing of trace gases in Beijing, China," *Optical Engineering*, vol. 49, no. 11, p. 111125, 2010.
- [24] R. Lewicki, A. A. Kosterev, D. M. Thomazy, T. H. Risby, S. Solga, T. B. Schwartz, and F. K. Tittel, "Real time ammonia detection in exhaled human breath using a distributed feedback quantum cascade laser based sensor," in *SPIE OPTO*, p. 79450K, International Society for Optics and Photonics, 2011.

- [25] K. Owen and A. Farooq, "A calibration-free ammonia breath sensor using a quantum cascade laser with WMS 2f/1f," *Applied Physics B*, pp. 1–13, 2013.
- [26] F. Fuchs, K. Degreif, F. Schnürer, S. Hugger, M. Kinzer, R. Aidam, W. Bronner, R. Lösch, and Q. Yang, "Imaging standoff detection of explosives using widely tunable midinfrared quantum cascade lasers," *Optical Engineering*, vol. 49, no. 11, p. 111127, 2010.
- [27] G. Wysocki, A. Kosterev, and F. Tittel, "Spectroscopic trace-gas sensor with rapidly scanned wavelengths of a pulsed quantum cascade laser for *in situ* NO monitoring of industrial exhaust systems," *Applied Physics B*, vol. 80, no. 4-5, pp. 617–625, 2005.
- [28] J. Lehtinen and T. Kuusela, "Broadly tunable quantum cascade laser in cantilever-enhanced photoacoustic infrared spectroscopy of solids," *Applied Physics B*, vol. 115, no. 3, pp. 413–418, 2014.
- [29] C. Hirschmann, J. Lehtinen, J. Uotila, S. Ojala, and R. Keiski, "Sub-ppb detection of formaldehyde with cantilever enhanced photoacoustic spectroscopy using quantum cascade laser source," *Applied Physics B*, vol. 111, no. 4, pp. 603–610, 2013.
- [30] J. Kottmann, U. Grob, J. M. Rey, and M. W. Sigrist, "Mid-infrared fiber-coupled photoacoustic sensor for biomedical applications," *Sensors*, vol. 13, no. 1, pp. 535–549, 2013.
- [31] P. Patimisco, S. Borri, A. Sampaolo, H. E. Beere, D. A. Ritchie, M. S. Vitiello, G. Scamarcio, and V. Spagnolo, "A quartz enhanced photo-acoustic gas sensor based on a custom tuning fork and a terahertz quantum cascade laser," *Analyst*, vol. 139, no. 9, pp. 2079–2087, 2014.
- [32] D. Marchenko, J. Mandon, S. Cristescu, P. Merkus, and F. Harren, "Quantum cascade laser-based sensor for detection of exhaled and biogenic nitric oxide," *Applied Physics B*, vol. 111, no. 3, pp. 359–365, 2013.
- [33] J. B. McManus, R. Wehr, M. S. Zahniser, D. D. Nelson, J. H. Shorter, S. Herndon, and E. Wood, "Application of quantum cascade lasers to high-precision atmospheric trace gas measurements," *Optical Engineering*, vol. 49, no. 11, p. 111124, 2010.
- [34] Q. Shi, D. D. Nelson, J. B. McManus, M. S. Zahniser, M. E. Parrish, R. E. Baren, K. H. Shafer, and C. N. Harward, "Quantum cascade infrared laser spectroscopy for real-time cigarette smoke analysis," *Analytical Chemistry*, vol. 75, no. 19, pp. 5180–5190, 2003.
- [35] D. Weidmann, A. A. Kosterev, C. Roller, R. F. Curl, M. P. Fraser, and F. K. Tittel, "Monitoring of ethylene by a pulsed quantum cascade laser," *Applied Optics*, vol. 43, no. 16, pp. 3329–3334, 2004.
- [36] K. Wörle, F. Seichter, A. Wilk, C. Armacost, T. Day, M. Godejohann, U. Wachter, J. Vogt, P. Radermacher, and B. Mizaikoff, "Breath analysis with broadly tunable quantum cascade lasers," *Analytical Chemistry*, vol. 85, no. 5, pp. 2697–2702, 2013.
- [37] M. C. Phillips, M. S. Taubman, B. E. Bernacki, B. D. Cannon, R. D. Stahl, J. T. Schiffern, and T. L. Myers, "Real-time trace gas sensing of fluorocarbons using a swept-wavelength external cavity quantum cascade laser," *Analyst*, vol. 139, no. 9, pp. 2047–2056, 2014.

- [38] R. Martini, C. Gmachl, J. Falciglia, F. G. Curti, C. G. Bethea, F. Capasso, E. A. Whittaker, R. Paiella, A. Tredicucci, A. L. Hutchinson, *et al.*, "High-speed modulation and free-space optical audio/video transmission using quantum cascade lasers," *Electronics Letters*, vol. 37, no. 3, pp. 191–193, 2001.
- [39] S. Blaser, D. Hofstetter, M. Beck, and J. Faist, "Free-space optical data link using peltier-cooled quantum cascade laser," *Electronics Letters*, vol. 37, no. 12, pp. 778–780, 2001.



## Chapter 3: Absorption spectroscopy



The choice of an optimum detection scheme for laser-based spectroscopic methods depends on the requirements of the specific application and the characteristic features of the infrared laser source. The application of spectroscopy requires a trade-off between the different factors mentioned in Section 1.2, sensitivity, accuracy, selectivity and precision. Absorption spectroscopy offers the best compromise between these aspects due to its simplicity and capabilities in a variety of fields. A detailed description of the mechanisms behind the absorption techniques used for the experiments described in this thesis are presented below, starting with a more in-depth discussion of the direct absorption sensor presented in the introduction Chapter 1. Consequently, we expand the description to cavity enhanced sensors and discuss the impact of noise on the detection limit including a short introduction to the characterization of frequency noise in the time domain in Section 3.2.

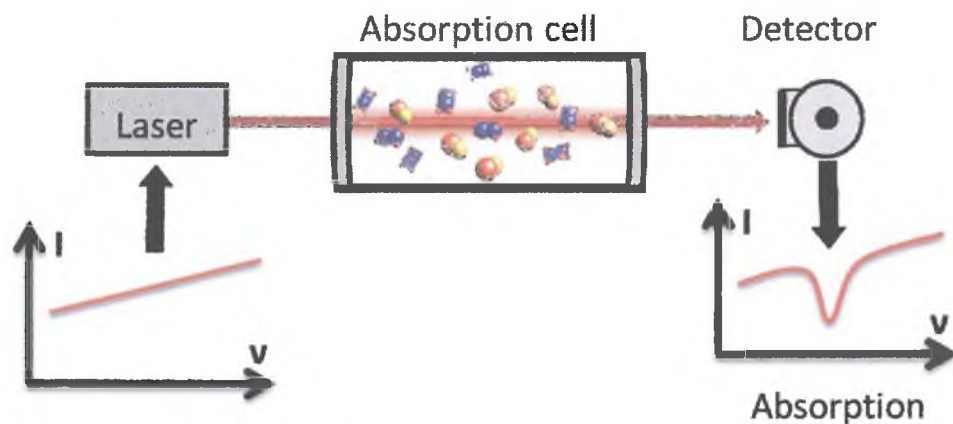
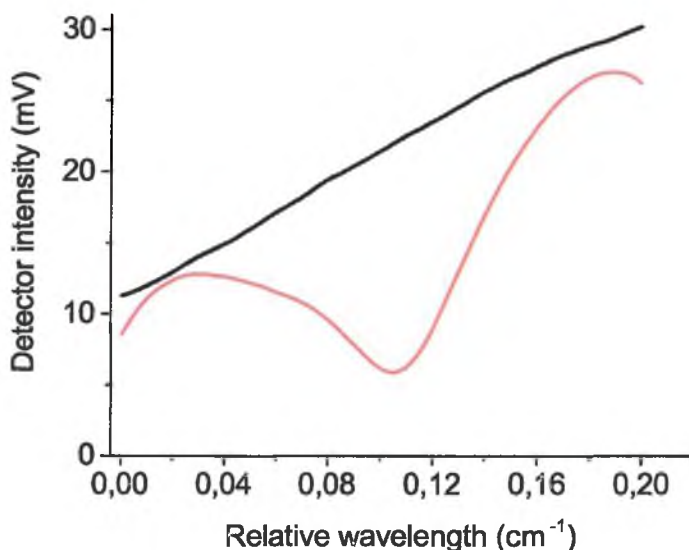


Figure 3.1: Schematic of a direct absorption sensor.

### 3.1 Introduction

**A**N ABSORPTION-BASED SENSOR consists of three elements: a light source, an absorbing sample, and a detector to measure the transmitted light. To understand the requirements of a trace-gas sensor and the important parameters for its design and characterization, we consider a simple laser-based direct absorption spectroscopy (DAS) setup as illustrated in Fig. 3.1. The laser source sends a beam through a gas cell containing an unknown gas sample at a specific pressure. To determine the concentration of the gases inside the cell, the absorption of the laser intensity in the presence of a gas sample has to be measured as a function of its optical frequency. Identification of these unknown compounds occurs by matching the recorded absorption spectrum with theoretical calculations from a database such as HITRAN [1] or GEISA [2] or by comparison with a reference measurement. As each molecule has its own unique absorption spectrum in the MIR, the absolute concentrations of the molecules in the gas sample can be calculated if the integrated line strength of the targeted absorption line is known. The optical intensities in the absence and presence of an absorber in the sensor shown in Fig. 3.1 are related by the Beer-Lambert law, given in Eq. 1.3.1 in Section 1.3. The absorption coefficient  $\alpha$ , per unit length in units of  $\text{cm}^{-1}$ , can be readily determined by a fit of Eq. 1.3.1 to the measured absorption profile. Most semiconductor lasers are scanned in frequency by varying their laser current, therefore making the optical intensities



**Figure 3.2:** Typical direct absorption scan showing a single molecular absorption feature over  $0,2 \text{ cm}^{-1}$ . Scanning is achieved by a linear current ramp to a quantum cascade laser, which results in a sloping background due to the changing laser power during a frequency scan.

$I_0$  and  $I$  frequency dependent. The form of the Beer-Lambert law (Eq. 1.3.1) rewritten in frequency dependent form is:

$$I_t(\nu) = I_0(\nu) \exp(-\alpha(\nu)L) \quad (3.1.1)$$

where  $I_0(\nu)$  and  $I_t(\nu)$  are the optical intensities in the absence and presence of an absorber,  $L$  is the effective optical path length inside the absorber in cm (in direct absorption equal to the length of the cell) and  $\alpha(\nu)$  is the absorption coefficient in  $\text{cm}^{-1}$  as introduced in Chapter 1. As the intensity changes during a scan, the resulting absorption trace will consist of a background slope with the absorption peak on top, a typical example of this being shown in Fig. 3.2. This sloping background can be removed by normalizing this varying incident intensity:

$$\frac{I_t(\nu)}{I_0(\nu)} = \exp(-\alpha(\nu)L) \quad (3.1.2)$$

We can expand the absorption coefficient  $\alpha(\nu)$  as a sum over all chemicals

present

$$\alpha(\nu) = \sum \sigma_i(\nu) N_i \quad (3.1.3)$$

where  $\sigma_i(\nu)$  is (see Eq. 1.4.1) the absorption cross-section of the  $i^{\text{th}}$  chemical at  $\nu$  and  $N_i$  is the number density. Lasers are usually employed to measure weak absorption features and it is important to know what minimum detectable absorption can be observed with a given sensor. The intensity fluctuations, while probing an absorption feature, can be written as

$$\Delta I = I_0 - I_t \quad (3.1.4)$$

Since we are assuming that  $\Delta I \ll I_0$ , the exponential in Eq. 3.1.1 can be expanded and only the constant and linear terms are retained

$$\frac{\Delta I}{I_0} = \alpha L \quad (3.1.5)$$

$\Delta I/I_0$  is a direct measure of the signal-to-noise ratio of the resulting detector signal. The signal fluctuations, which decrease the quality of the measurements, originate from different sources within a sensor and constitute noise, thus limiting  $(\Delta I/I_0)_{\min}$ . The absorption sensitivity of the instrument shows its performance limitations and can be determined by the relation

$$\alpha_{\min} = \frac{1}{L} \left( \frac{\Delta I}{I_0} \right)_{\min} \quad (3.1.6)$$

where  $(\Delta I/I_0)_{\min}$  is taken as the ratio of the noise on the baseline of the transmission signal and the maximum transmission in the absence of an absorber. The value we obtain for  $\alpha_{\min}$  depends on how long we take to measure it; longer measurement times average out the random noise contribution more and thus achieve smaller values of  $(\Delta I/I_0)_{\min}$  (we will come back to this matter when discussing the Allan deviation in Section 3.2). When comparing different techniques or systems, it is therefore important to consider the noise level that is finally obtained on the baseline of an acquired spectrum for a given measurement time. In this respect, the detection limit is usually reported in terms of a 1 Hz bandwidth, i.e. for 1 s averaging per data point (or per spectral element if scanning is performed and the data point separation is larger than the spectral resolution). Moreover, if  $N_p$  data points are measured in 1 s, it is common to normalize the detection limit by  $\sqrt{N_p}$ , since the acquisition of

$N_p$  individual data points can be considered equivalent to  $N_p$  independent values averaged to a single data point. This equivalence is only valid when the data is limited by white noise, but not in the presence of fringes or other noise sources, which usually contribute more strongly at longer timescales (' $1/f$ ' noise, associated to setup drifts, discussed in Section 3.2). For instance, an acquisition of 100 spectral data points in 1 s may yield a spectrum with a relatively large noise level  $\sigma$ , where fringes are not visible. Averaging this spectrum 100 times would decrease the white noise component by a factor 10 and would reveal the fringes, which normally are stationary over relatively long time scales. These fringes would then dominate the noise level of the spectrum, ending up with a total noise level larger than  $\sigma/\sqrt{N_p}$ .

The absorption coefficient can be converted into a minimum detectable absorption per point (MDA), normalized by time and given in  $\text{Hz}^{-1/2}$  with  $N_p$  data points per spectrum. This quantity is given for the direct absorption sensor in Fig. 3.1 by [3]:

$$\text{MDA}^{\text{DAS}} = \left( \frac{\Delta I}{I_0} \right)_{\min} \sqrt{\frac{nT}{N_p}} = \alpha_{\min} L \sqrt{\frac{nT}{N_p}} \quad (3.1.7)$$

with a relevant bandwidth taken as the data acquisition rate  $B = r_{\text{data}} = 1/nT$  ( $n$  is the number of scans). If we assume that the data, from which  $\Delta I/I_0$  is measured, involves 1 s of integration, then  $nT = 1$  s and  $B = 1$  Hz. The MDA can be used for comparing sensor performances of different instruments. Note that this quantity characterizes the overall sensor and not the chemical under detection, while  $\alpha_{\min}$  characterizes one system and allows for the determination of the lowest detectable concentration of a gas. This definition of MDA (per point) is not scaled to the optical path length. Consequently, to compare to different systems, there is another common measure of sensor performance, the so-called 'Noise Equivalent Absorbance Sensitivity' (NEAS) per point, which is the MDA scaled to path length in units of  $\text{cm}^{-1}\text{Hz}^{-1/2}$  and thus is independent of the detection method and light sources employed. This quantity is given by

$$\text{NEAS}^{\text{DAS}} = \frac{\text{MDA}}{L} = \left( \frac{\Delta I}{I_0} \right)_{\min} \frac{1}{L} \sqrt{\frac{nT}{N_p}} \quad (3.1.8)$$

**Example**

The absorption sensitivity of the signals shown in Fig. 3.2 would be  $1,7 \cdot 10^{-3} \text{ cm}^{-1}$ , assuming fluctuations of 1 mV, an absorption-free signal of 20 mV and a cell length of 30 cm. The corresponding MDA per point is then  $5 \cdot 10^{-3} \text{ Hz}^{-1/2}$  for a total integration time of 1 s and for 100 points. The system has a NEAS per point of  $1,7 \cdot 10^{-4} \text{ cm}^{-1} \text{ Hz}^{-1/2}$ .

The use of  $\alpha_{\min}$ , MDA and NEAS is ambiguous as some authors use  $\alpha_{\min}$  as NEAS with or without the spectral bandwidth, thus their interpretation varies greatly from author to author.

**Info**

Authors vary in their definitions of MDA and NEAS as they disagree on the relevant bandwidth and normalization standards. Some authors prefer a definition of MDA that is dependent on scan characteristics, referring to a sweep over an actual scan within a given integration time. Others further scale MDA by the number of optical passes or normalize it to the molecular concentration. The same issues apply for the NEAS and are not further discussed here. For an extensive review of this matter, we refer the reader to the article of Moyer et al. [3].

Ultimately, in our approach  $\alpha_{\min}$  gives the absolute potential performance of a given sensor, and allows a direct comparison of the sensitivity of gases measured different sensors. The NEAS on the other hand is particularly useful when discussing the limitations due to noise on a particular class of sensors or a specific technique of signal recovery neglecting the optical path length. This will be seen when the shot noise limited performance of the direct absorption sensor is calculated in Section 3.1.1. A consistent use of the aforementioned quantities is kept throughout this thesis.

### 3.1.1 The influence of noise on the sensitivity

Any sensor is limited in its sensitivity by noise originating from various sources. In a community where sensitivity is a central issue, noise is of great prominence. For trace gas detection, the increase in signal is as important as the reduction of noise. By using lasers with frequencies in the MIR, one can greatly increase

the absorption signal by probing absorption lines with the largest available absorption cross-section  $\sigma$ .

Eq. 3.1.6 also shows that  $\alpha_{\min}$  can be further reduced for a given sensor by minimizing the total noise or increasing the absorption path length. Herriot cells are one solution to achieve a long path length in a small sensor, as are the use of optical cavities, which will be introduced in Section 3.3. If the limiting noise is assumed to have a white spectrum, the limit of detection decreases with the square root of the effective detection bandwidth  $B$ . To minimize the noise, we need to understand the different sources of noise. We first consider 'white' noise such as shot noise in the detector photocurrent and Johnson noise in the detector and pre-amplifier resistors. Shot noise originates from the quantized nature of light, and manifests itself in random fluctuations in the electrical current upon the conversion of light incident on the transmission detector to electrical current. The current  $i_{\text{DC}}$  from a detector is given by [4]

$$i_{\text{DC}} = \eta_c P \quad (3.1.9)$$

with  $P$  the incident power of the laser in W and  $\eta_c$  the responsivity of the detector in A/W. The shot noise current then is

$$i_{\text{shot}} = \sqrt{2eBi_{\text{DC}}} \quad (3.1.10)$$

where  $e$  is the charge of the electron and  $B$  the detection bandwidth in Hz. When using lasers in the infrared region, the laser photocurrent dominates and the resulting relative current fluctuations are

$$\frac{i_{\text{shot}}}{i_{\text{DC}}} = \sqrt{\frac{2eB}{i_{\text{DC}}}} = \sqrt{\frac{2eB}{\eta_c P}} \quad (3.1.11)$$

The impact of noise can be lowered by increasing the laser power, but this benefit is limited due to the square root dependence on the photocurrent in Eq. 3.1.11.

Johnson noise is due to the thermal agitation of the charge carriers within resistors, which form an essential part of the electronics used in optical detection schemes. The Johnson current noise is given by [4]

$$i_R = \sqrt{\frac{4kTB}{R}} \quad (3.1.12)$$

where  $k$  is Boltzman's constant,  $T$  is the temperature in Kelvin and  $R$  is the resistance in Ohm. Other sources of electronic noise include the input noise of

the operational amplifiers used in the transimpedance amplifier, and the Johnson noise of other surrounding resistors in the circuit.

Shot noise is often regarded as the ultimate limit in detection, because, in theory, the effects of all other noise sources can be eliminated to an arbitrarily small value. Since photocurrent is proportional to optical intensity, we assume shot noise to be the only noise source, and write

$$\left(\frac{\Delta I}{I_0}\right)_{\min} = \left(\frac{\Delta I}{I_0}\right)_{\text{shot}} = \frac{i_{\text{shot}}}{i_{\text{DC}}} \quad (3.1.13)$$

Substituting this and Eq. 3.1.11 into Eq. 3.1.8, we get the shot noise limited version of the NEAS per point for the direct absorption sensor shown in Fig. 3.1:

$$\text{NEAS}_{\text{shot}}^{\text{DAS}} = \frac{1}{L} \sqrt{\frac{nT}{N_p}} \sqrt{\frac{2eB}{i_{\text{DC}}}} = \frac{1}{L} \sqrt{\frac{2e}{\eta_c P N_p}} \quad (3.1.14)$$

### Example

For example, if we detect a photocurrent of 65  $\mu\text{A}$  in the system used for the example above, the relative current fluctuation (Eq. 3.1.11) due to the shot noise is  $7,0 \cdot 10^{-8}$ . The relative Johnson current noise  $i_R/i_{\text{DC}}$  for a 42  $\text{k}\Omega$  resistance is then  $9,6 \cdot 10^{-9}$ . In this example, the shot noise dominates the Johnson noise. The shot noise limited NEAS for this system (30 cm cell length, 100 points per spectrum) is then  $2,3 \cdot 10^{-10} \text{ cm}^{-1} \text{ Hz}^{-1/2}$ .

However, it is often not desirable to achieve this limit as it adds enormous complexity to the setup. In conventional absorption spectroscopy, it would be difficult to reach this noise level for a sensor due to a different type of noise, explained hereafter.

Another type of noise is '1/f'-noise or 'pink noise', where the measured noise is inversely proportional to a center frequency  $f$ . This is the most common kind of noise after the shot noise and has multiple origins. Sources of 1/f-noise include all kinds of electrical components like detectors, laser power supplies and laser intensities itself. To reduce 1/f-noise, several methods exist such as implementing modulation techniques (Section 8.1) and laser frequency stabilization (Section 8.2).

White and pink noise are examples of random noise sources, but there are also systematic noise sources. The most important ones are residual amplitude

modulation (RAM) and etalons, arising from multiple reflections between optical surfaces, such as cell and detector windows, lenses, and other optics. This interference is frequency dependent and can only be circumvented by use of optical isolators, optical elements with a anti-reflective coating or by placing the optical components at etalon immune distances [5]. RAM is an example of a combined noise effect. When we modulate the frequency of a laser field, a small fraction of amplitude modulation (AM) is present. The moment the intensity varies due to a frequency scan or modulation (similar to the laser scan causing the slope in Fig. 3.2), RAM can actually re-couple  $1/f$ -noise back into the signal, although the FM technique is supposed to suppress it. A more in-detail discussion of this phenomenon will take place in the discussion of the laser locking in Section 8.4.

## 3.2 Allan variance

To characterize frequency stability of oscillators in the time-domain, D. W. Allan introduced the so-called Allan variance,  $\sigma_y^2(\tau)$  [6]. This quantity is a measure for the stability of an oscillator in the time domain over an averaging time  $\tau$ , but has the disadvantage of being a one-variable evaluation test, which can be applied to a single spectral point at a time, but not to a complete spectral section. The Allan variance delivers information about the time variability of certain baseline drifts such as fringes, temperature or pressure fluctuations affecting a single spectral point. The Allan variance is the difference of two fractional frequency values  $f(i+1)$  and  $f(i)$  measured at times  $t_0 + i\tau$  and  $t_0 + (i+1)\tau$ , respectively. For each time interval  $\tau$ , a series of  $N$  measurements are made. The Allan variance for a finite number of measurements is then estimated using the formula

$$\sigma_y^2(\tau) = \frac{1}{2(N-1)} \sum_{n=1}^{N-1} (f_{n+1} - f_n)^2 \quad (3.2.1)$$

The Allan deviation is given by taking the square root of the Allan variance

$$\sigma_y(\tau) = \sqrt{\sigma_y^2(\tau)} \quad (3.2.2)$$

An Allan deviation plot is useful to quantitatively estimate the precision in the determination of some spectroscopic parameters such as the measured concentration of a gas sample. Providing a stationary sample, the Allan deviation determines over what time interval the data can be averaged before

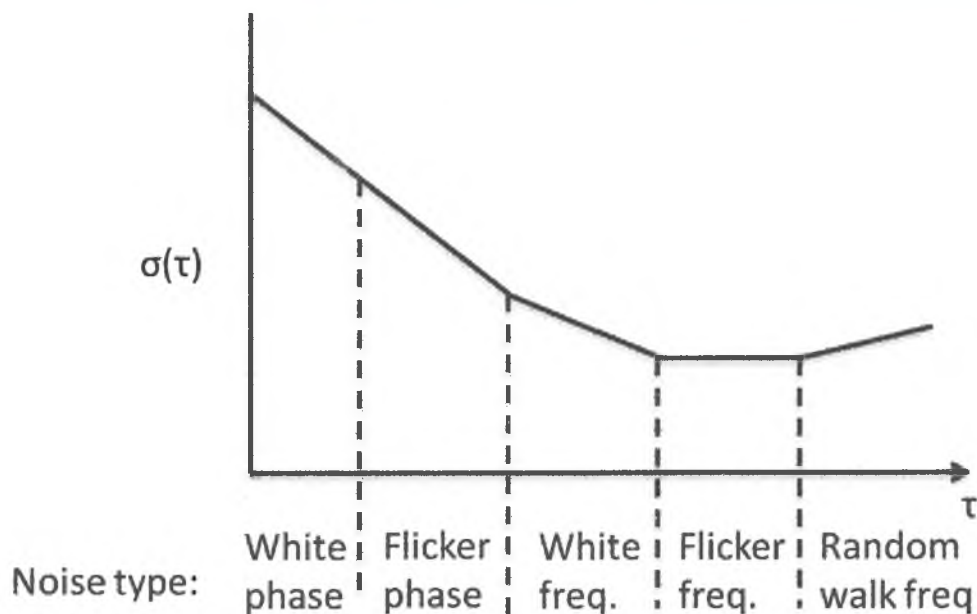


Figure 3.3: Allan deviation as a function of averaging time.

drifts become dominant, and the Allan deviation value for a given averaging time will provide a true estimate of the fluctuations of concentration averaged over this time interval. Additionally, the time after which the Allan deviation starts to increase, will indicate the stability time of the setup. This supports calibration procedures to achieve the highest accuracy, if they are realized within this time frame. Plotting the Allan deviation versus the averaging time  $\tau$  yields the Allan deviation curve, which gives information about the type and level of noise present in the system. The longer the measurement time for a given data point, the more accurate the result. A graph of the Allan deviation is shown in Fig. 3.3. It shows the improving stability of a system as the averaging time  $\tau$  gets longer, changing from the white phase noise ( $\tau^{-1}$ ) via the white frequency noise ( $\tau^{-1/2}$ ) and the pink noise ( $\tau^0$ ) to the random walk ( $\tau^{1/2}$ ). This explains, why the MDA (Eq. 3.1.7), normalized by the square root of time, will not change its value, if white frequency noise is the dominant type of noise in the system, because the increase in time will be compensated by the reduction in noise. It is evident from the graph that some noise types can be removed by averaging, however, at the so-called noise floor, more averaging no longer improves the results due to baseline drifts.

### 3.3 Cavity enhanced absorption spectroscopy

The sensitivity of the sensor introduced in Fig. 3.1 can be enhanced by replacing the direct absorption cell with an optical resonator. A optical resonator consists of two aligned highly reflective curved mirrors, where light interferes after it retraces its path between the mirrors. Constructive interference is obtained only in narrow, discrete spectral regions for which the total optical path lengths are approximately integer multiples of the wavelength of the light. These narrow spectral regions are so-called longitudinal modes, and their separation in frequency is known as the free spectral range (FSR) of the cavity. Once the laser frequency matches a longitudinal mode frequency, much of the incident laser field is coupled into the cavity. The coupling of the light into the cavity can be maximized by mode-matching the laser beam to the cavity. This means that the beam waist and the radius of curvature of the beam's wavefront are adjusted to spatially match one longitudinal cavity mode, which prevents the excitation of transverse modes. In cavity-enhanced measurements, a light beam is reflected between two mirrors with a small amount of radiation exiting through the mirrors at each reflection. The high reflectivity of the mirrors enables effectively thousands of round trips for the light, resulting in an effective cavity path length that is much greater than the cavity's physical length and in intra-cavity intensities thousands of times higher than that of the incident beam. The result is an instrument with a potentially improved sensitivity values compared to direct absorption spectroscopy, which allows for the detection of trace gases at low concentrations in small volumes, for example the detection of metabolites in breath. This section deals with the influence of an optical cavity on the sensitivity.

A spherical two-mirror cavity satisfies the following stability condition:

$$0 < (1 - L/r_1)(1 - L/r_2) < 1 \quad (3.3.1)$$

where  $L$  is the mirror spacing and  $r_1$  and  $r_2$  are the mirror curvatures. The ratio of power in the absence and presence of an absorber for a stable resonant optical cavity is [4]

$$\frac{I_t}{I_0} = C_p \frac{T^2}{[1 - R \cdot \exp(-\alpha L)]^2} \quad (3.3.2)$$

where  $T$  and  $R$  are the intensity transmission and reflection coefficients of both cavity mirrors and  $L$  is the interaction length in the gas sample. The factor  $C_p$  is

the fraction of the laser beam that is matched to the spatial profile of the optical cavity mode. Following a treatment similar to Gianfrani et al. [9, 10], if  $\alpha L$  is much less than one, then

$$\exp(-\alpha L) \approx 1 - \alpha L \quad (3.3.3)$$

and we can rewrite (3.3.2) as

$$\begin{aligned} \frac{I_t}{I_0} &\approx C_p \frac{T^2}{[1 - R + R\alpha L]^2} \\ &= C_p \frac{T^2}{(1 - R)^2} \frac{1}{[1 + \alpha L \frac{R}{1 - R}]^2} \end{aligned} \quad (3.3.4)$$

Normalizing by the empty cavity transmission intensity  $I_{t0}$ , we get

$$\frac{I_t}{I_{t0}} = \frac{1}{[1 + \alpha L \frac{R}{1 - R}]^2} \quad (3.3.5)$$

Equations 3.3.4 and 3.3.5 are valid for high intra-cavity absorption levels. However, if the intra-cavity losses are very small,  $\alpha L$  must be much less than  $1 - R$ . This allows us to use the binomial expansion to write

$$\frac{I_t}{I_{t0}} \approx \left[ 1 - \alpha L \frac{2R}{1 - R} \right] \quad (3.3.6)$$

From this, the relative change in transmission intensity, while scanning over such a weak absorption feature, is

$$\frac{\Delta I_t}{I_{t0}} \cong \alpha L \frac{2R}{1 - R} \quad (3.3.7)$$

which is identical to Eq. 3.1.5 for weak direct absorption, but enhanced by the factor  $2R/(1 - R)$ .

The finesse of an optical cavity is defined as the ratio of the free spectral range (FSR) to the full width at half maximum (FWHM) of a cavity mode and both are related to each other by

$$\mathcal{F} = \frac{\text{FSR}}{\text{FWHM}} = \frac{\pi}{2 \arcsin(1/\sqrt{F})} \quad (3.3.8)$$

where  $F = 4R/(1 - R)^2$  is the coefficient of finesse. Due to the small intra-cavity losses, we can approximate the finesse by:

$$\mathcal{F} \approx \frac{\pi R^{\frac{1}{2}}}{1 - R} \quad (3.3.9)$$

Since  $R \cong \sqrt{R} \cong 1$ , by substituting Eq. 3.3.9 into Eq. 3.3.7, we can write an expression for small relative fluctuations in cavity transmission:

$$\frac{\Delta I_t}{I_{t0}} \cong \alpha L \frac{2\mathcal{F}}{\pi} \quad (3.3.10)$$

where  $2\mathcal{F}/\pi$  is called the cavity enhancement factor on resonance compared to the single pass absorption  $\alpha L$ .

### Example

**Example:** Consider a resonant cavity with length of 30 cm and with a mirror reflectivity of 99,8%, then the finesse is 1569 and thus is the enhancement factor equal to 1000, yielding an effective optical path length of 300 m.

Following the derivation in Section 3.1, if we now consider the intensity fluctuations on the transmitted optical beam  $\Delta I$ , then the absorption sensitivity becomes

$$\alpha_{\min} = \left( \frac{\Delta I}{I_0} \right)_{\min} \cdot \frac{\pi}{2\mathcal{F}L} \quad (3.3.11)$$

and consequently, the NEAS per point for DAS derived in Eq. 3.1.8 becomes now

$$\text{NEAS}^{\text{CEAS}} = \frac{\pi}{2\mathcal{F}L} \cdot \text{NEAS}^{\text{DAS}} = \frac{\pi}{2\mathcal{F}L} \left( \frac{\Delta I}{I_0} \right)_{\min} \sqrt{\frac{nT}{N_p}} \quad (3.3.12)$$

In DAS, we considered the cell length  $L$  (in cm), whereas now we have to take the increased path length into account, therefore multiplying with the resonant cavity enhancement factor  $2\mathcal{F}/\pi$ . Again, we stress the fact that  $(\Delta I/I_0)_{\min}$  is the ratio of the noise on the baseline of the cavity transmission and the maximum transmission in the absence of an absorber and not the signal-to-noise ratio of the absorption line, because NEAS and MDA are gas-independent quantities.

Similarly to the treatment in Section 3.1.1, we can calculate the theoretical shot noise limited performance. Combining Eq. 3.3.12 and Eq. 3.1.14, we get the resonant cavity enhanced NEAS per point

$$\text{NEAS}_{\text{shot}}^{\text{CEAS}} = \frac{\pi}{2\mathcal{F}L} \sqrt{\frac{nT}{N_p}} \sqrt{\frac{2eB}{i_{\text{DC}}}} = \frac{\pi}{2\mathcal{F}L} \sqrt{\frac{2e}{\eta_c P N_p}} \quad (3.3.13)$$

Again, this noise level is highly unlikely to be achieved without any additional techniques due to the presence of  $1/f$ -noise. A possible solution to overcome this is presented in Chapter 8.

### Example

If the system in the example above gets cavity enhanced with an enhancement factor of 1000 due to mirrors of 99,8% reflectivity, the resulting shot noise limited NEAS will become a factor 1000 lower, yielding  $2,3 \cdot 10^{-13} \text{ cm}^{-1} \text{ Hz}^{-1/2}$ .

### 3.3.1 Off-axis integrated cavity output spectroscopy

Integrated cavity output spectroscopy (ICOS) has been developed independently by O'Keefe et al. [7] and Engeln et al. [8]. In off-axis ICOS (OA-ICOS), the light gets injected into an optical resonator under an angle with respect to the optical axis and multiple reflections occur before the light beam returns to its entry position [11]. Off-axis injection produces a dense or almost continuous cavity transmission pattern as a result of the excitation of high order transverse electromagnetic (TEM) modes of the cavity. Figure 3.4 summarizes the differences between on-axis and off-axis ICOS. The off-axis laser-cavity geometry has several advantages over other cavity based spectroscopic methods or a multipass cell approach:

1. No requirement of fast time-resolved measurements or high laser pulse energies
2. Alignment robustness
3. Reduced complexity and high versatility
4. Small cell volume

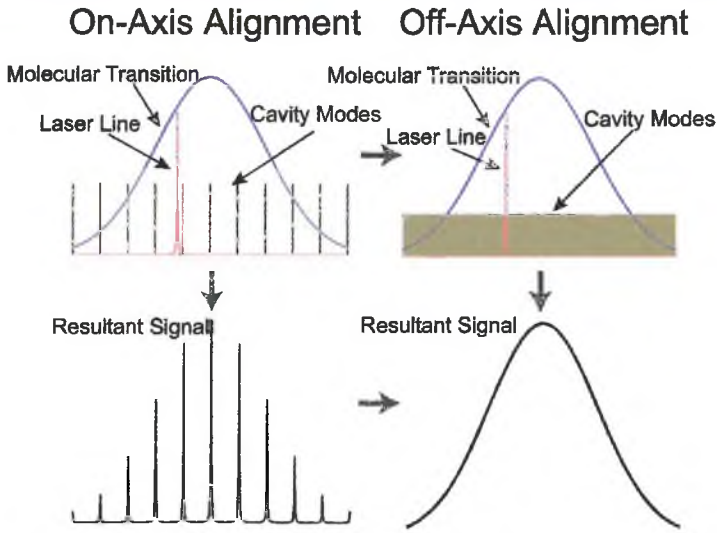


**Figure 3.4:** Comparison of the on-axis and off-axis mode structure. The top panels show how the transversal modes effectively merge into a continuum in off-axis alignment, such that the laser line width is broader than the free spectral range of the cavity, but narrow compared to the molecular transition. The resulting absorption signals are given in the two bottom panels [12].

Off-axis beam propagation in a stable two-mirror cavity was first analyzed in 1964 by Herriott, Kogelnik, and Kompfer [13]. For a spherical two-mirror cavity, which fulfills the stability condition given in Eq. 3.3.1, the spot pattern on the mirrors generally lies on an ellipse, or in a Lissajous spot pattern for astigmatic mirrors, which can further lengthen the re-entrant condition. The goal is to maximize the number of spots that before interference occurs, therefore taking the form of a circle near the edge of the mirrors. The angle  $2\theta$  of a round-trip rotation of a beam spot is determined solely by the geometry of the cavity, namely the mirror spacing  $L$  and curvature  $r$  (assumed equal):

$$\cos(\theta) = 1 - L/r \quad (3.3.14)$$

The re-entrant condition is satisfied if

$$2m\theta = 2n\pi \quad (3.3.15)$$

where  $m$  is the number of the beam round trips and  $n$  is an integer. The FSR is then compressed to  $c/2Lm$ . For OA-ICOS it is desirable to have the highest possible value of  $m$  that can be achieved without having overlapping

beams. The ideal case is achieved when the effective cavity FSR is significantly smaller than the laser line width. Once this condition is satisfied, the resonant cavity properties disappear and the cavity output does not depend on the laser frequency over a small range, which results in a smooth absorption curve yielding improved sensitivity values compared to on-axis ICOS. Alternatively, the laser frequency can be rapidly scanned through the cavity mode or one of the cavity mirrors can be dithered to generate random jittering of the cavity modes. Note that the ICOS cell (like any resonant cavity) has a low pass frequency response, with a cutoff frequency given by  $f_{3dB} = 1/(2\pi\tau)$ , where  $\tau$  is the cavity lifetime. This frequency response must be taken into account for the appropriate modulation frequency of the laser and the detection bandwidth.

The laser power transmitted through the cavity is given by [11]

$$I_t = I_0 C_p \frac{(1 - R)^2}{2[(1 - R) + \alpha L]} \quad (3.3.16)$$

where  $I_0$  is the laser power without being absorbed,  $C_p$  is a cavity coupling parameter (between 0 and 1) depending on the finesse of the cavity and the number of round trips, and  $\alpha$  is the absorption coefficient. For pulsed lasers,  $C_p$  often has low ( $\sim 0, 1$ ) values. The factor of 2 in the loss term accounts for the fact that the light leaves through both mirrors, whereas it enters through only one. In contrast to other methods, OA-ICOS is not sensitive to field interference inside the cavity, because the cross field terms average to zero due to the interference of incoherent fields, which explains the reduced cavity transmission for OA-ICOS (or broadband CEAS in general) in Eq. 3.3.16 by a factor of  $T/2$  as compared to resonant CEAS. This results in an effective non-resonant absorption path length  $L_{eff}^{nr}$  reduced by a factor 2

$$L_{eff}^{nr} = \frac{1}{1 - R} L \simeq \frac{\mathcal{F}}{\pi} L = \frac{L_{eff}^{res}}{2} \quad (3.3.17)$$

This difference in cavity enhancement comes from the fact that non-resonant CEAS is sensitive to the resonance profile surface, while resonant CEAS depends only on the peak transmission. When intra-cavity losses increase, the peak amplitude decreases faster than the mode profile area, because at the same time the width of the resonance increases half as fast.

## Info

The enhancement factor in CEAS does not depend only on the cavity, but also on the light source and the injection scheme. Here, we have studied static configurations in the two extreme limits, where analytical results are straightforward. In general, we may write the enhancement factor as  $\beta\mathcal{F}/\pi$  [20], where  $\beta$  ranges between 1 for non-resonant CEAS and 2 for monochromatic resonant CEAS. It should also be stressed that the dependence on intra-cavity absorption is modified, since the absorption law for resonant (Eq. 3.3.2) and non-resonant CEAS (Eq. 3.3.16) differ. Intermediate configurations may exist, though they are not common.

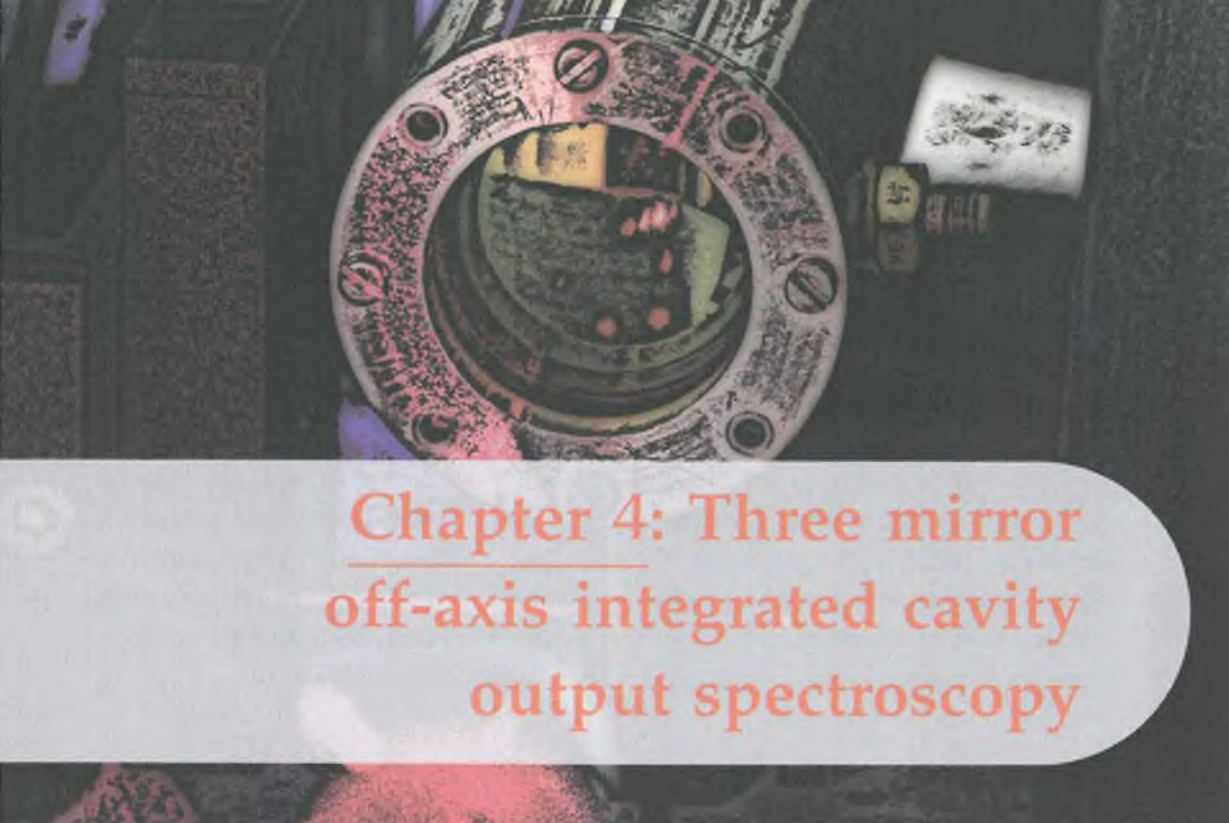
OA-ICOS has proven to be one of the most sensitive and robust laser-based techniques [14], making it technically less demanding and more cost effective than other laser-based methods and has been used in various applications in combination with a wide range of light sources [15–17]. A drawback of this technique is the significantly lower transmission power through the cavity compared with resonant-coupling methods. Therefore, either high-power sources have to be used, or the light reflected by the cavity has to be re-injected [18, 19]. Chapter 4 describes the employment of such a re-injection method using OA-ICOS and a pulsed QCL.

# References

- [1] L. S. Rothman, I. E. Gordon, A. Barbe, D. C. Benner, P. F. Bernath, M. Birk, V. Boudon, L. R. Brown, A. Campargue, J. P. Champion, *et al.*, "The HITRAN 2008 molecular spectroscopic database," *Journal of Quantitative Spectroscopy and Radiative Transfer*, vol. 110, no. 9, pp. 533–572, 2009.
- [2] N. Jacquinet-Husson, L. Crepeau, R. Armante, C. Boutammime, A. Chédin, N. Scott, C. Crevoisier, V. Capelle, C. Boone, N. Poulet-Crovisier, *et al.*, "The 2009 edition of the GEISA spectroscopic database," *Journal of Quantitative Spectroscopy and Radiative Transfer*, vol. 112, no. 15, pp. 2395–2445, 2011.
- [3] E. Moyer, D. Sayres, G. Engel, J. S. Clair, F. Keutsch, N. Allen, J. Kroll, and J. Anderson, "Design considerations in high-sensitivity off-axis integrated cavity output spectroscopy," *Applied Physics B*, vol. 92, no. 3, pp. 467–474, 2008.
- [4] C. C. Davis, *Lasers and Electro-Optics: Fundamentals and Engineering*. Cambridge University Press, 2014.
- [5] P. Ehlers, A. C. Johansson, I. Silander, A. Foltynowicz, and O. Axner, "Use of etalon-immune distances to reduce the influence of background signals in frequency-modulation spectroscopy and noise-immune cavity-enhanced optical heterodyne molecular spectroscopy," *JOSA B*, vol. 31, no. 12, pp. 2938–2945, 2014.
- [6] D. W. Allan, "Statistics of atomic frequency standards," *Proceedings of the IEEE*, vol. 54, no. 2, pp. 221–230, 1966.
- [7] A. O'Keefe, "Integrated cavity output analysis of ultra-weak absorption," *Chemical Physics Letters*, vol. 293, no. 5, pp. 331–336, 1998.
- [8] R. Engeln, G. Berden, R. Peeters, and G. Meijer, "Cavity enhanced absorption and cavity enhanced magnetic rotation spectroscopy," *Review of Scientific Instruments*, vol. 69, no. 11, pp. 3763–3769, 1998.
- [9] L. Gianfrani, R. W. Fox, and L. Hollberg, "Cavity-enhanced absorption spectroscopy of molecular oxygen," *JOSA B*, vol. 16, no. 12, pp. 2247–2254, 1999.
- [10] G. Gagliardi and L. Gianfrani, "Trace-gas analysis using diode lasers in the near-IR and long-path techniques," *Optics and Lasers in Engineering*, vol. 37, no. 5, pp. 509–520, 2002.
- [11] J. B. Paul, L. Lapson, and J. G. Anderson, "Ultrasensitive absorption spectroscopy with a high-finesse optical cavity and off-axis alignment," *Applied Optics*, vol. 40, no. 27, pp. 4904–4910, 2001.
- [12] G. S. Engel, W. S. Drisdell, F. N. Keutsch, E. J. Moyer, and J. G. Anderson, "Ultrasensitive near-infrared integrated cavity output spectroscopy technique for detection of CO at 1.57  $\mu\text{m}$ : New sensitivity limits for absorption measurements in passive optical cavities," *Applied Optics*, vol. 45, no. 36, pp. 9221–9229, 2006.

- [13] D. Herriott, H. Kogelnik, and R. Kompfner, "Off-axis paths in spherical mirror interferometers," *Applied Optics*, vol. 3, no. 4, pp. 523–526, 1964.
- [14] D. S. Sayres, E. Moyer, T. Hanisco, J. S. Clair, F. Keutsch, A. O'Brien, N. Allen, L. Lapson, J. Demusz, M. Rivero, *et al.*, "A new cavity based absorption instrument for detection of water isotopologues in the upper troposphere and lower stratosphere," *Review of Scientific Instruments*, vol. 80, no. 4, p. 044102, 2009.
- [15] P. Malara, P. Maddaloni, G. Gagliardi, and P. De Natale, "Combining a difference-frequency source with an off-axis high-finesse cavity for trace-gas monitoring around 3  $\mu\text{m}$ ," *Optics Express*, vol. 14, no. 3, pp. 1304–1313, 2006.
- [16] M. Silva, D. Sonnenfroh, D. Rosen, M. Allen, and A. O'Keefe, "Integrated cavity output spectroscopy measurements of NO levels in breath with a pulsed room-temperature QCL," *Applied Physics B*, vol. 81, no. 5, pp. 705–710, 2005.
- [17] S. Williams, M. Gupta, T. Owano, D. S. Baer, A. O'Keefe, D. R. Yarkony, and S. Matsika, "Quantitative detection of singlet O<sub>2</sub> by cavity-enhanced absorption," *Optics Letters*, vol. 29, no. 10, pp. 1066–1068, 2004.
- [18] R. Centeno, J. Mandon, S. Cristescu, and F. Harren, "Three mirror off-axis integrated cavity output spectroscopy for the detection of ethylene using a quantum cascade laser," *Sensors and Actuators B: Chemical*, vol. 203, pp. 311–319, 2014.
- [19] J. B. Leen and A. O'Keefe, "Optical re-injection in cavity-enhanced absorption spectroscopy," *Review of Scientific Instruments*, vol. 85, no. 9, p. 093101, 2014.
- [20] M. J. Thorpe and J. Ye, "Cavity-enhanced direct frequency comb spectroscopy," *Applied Physics B*, vol. 91, pp. 397–414, 2008.





## Chapter 4: Three mirror off-axis integrated cavity output spectroscopy

This chapter is based on:

R. Centeno, J. Mandon, S.M. Cristescu, F.J.M. Harren, *Three mirror off-axis integrated cavity output spectroscopy for the detection of ethylene using a quantum cascade laser*, *Sensors and Actuators B: Chemical*, 203, 311 – 319 (2014),

<http://dx.doi.org/10.1016/j.snb.2014.06.122>

## Abstract

We demonstrate the performance of a compact and robust gas sensor based on a pulsed distributed feedback quantum cascade laser (QCL, laser pulses 30 ns, repetition rate 1 MHz) in combination with off-axis integrated cavity output spectroscopy (OA-ICOS) in an improved three mirror configuration. The room temperature laser (wavelength  $915\text{ cm}^{-1}$ ) was wavelength tuned over  $\sim 0,25\text{ cm}^{-1}$  with a 4 kHz repetition frequency. A detection limit of 10 ppbv (part-per-billion volume) for regular OA-ICOS is demonstrated for ethylene in 2 min averaging time, which is equal to a noise equivalent absorption sensitivity (NEAS) per point of  $1,5 \cdot 10^{-7}\text{ cm}^{-1}\text{ Hz}^{-1/2}$ . An improved three mirror configuration OA-ICOS scheme showed a 4 times increase in sensitivity as compared to standard OA-ICOS. The sensor was used for ethylene detection from apples, stored under controlled atmosphere conditions.

## 4.1 Introduction

**E**THYLENE IS A GASEOUS HORMONE that plays an important role in many aspects of plant growth and development; it is revealing stress responses in plants, induces wilting in flowers and causes fruit ripening [1, 2]. As such, there is a strong demand for a compact and easy to operate ethylene detector to monitor and control its emission in growth chambers, greenhouses and fruit storage facilities. The concentration levels, at which ethylene is active, range from the single ppbv level to ppmv levels for flowers (carnations, orchids) and ripening fruit, respectively [1, 2]. The current standard of preventing ethylene levels from increasing in fruit storage facilities is the use of controlled atmosphere (CA) such that the storage life can be extended. CA storage uses an atmosphere that differs substantially from normal air in respect to CO<sub>2</sub> and O<sub>2</sub> levels. Several methods for measuring ethylene levels have been implemented in agricultural research and fruit storage facilities [3]. Gas chromatography (GC) is currently the standard technique, where ethylene concentrations down to a few ppbv can be measured [4]. Disadvantages are the slow response time and the use of consumables such as chromatography columns and carrier gases, which make GC's maintenance intensive and costly in manpower. Other ways to detect ethylene are via non-dispersive infrared detection [5], amperometric [6] or electrochemical [7] methods or they rely on changes in luminescence properties [8, 9]. However, in general, these methods are not sensitive and selective enough to detect ethylene at low ppbv concentration levels.

Nowadays laser-based detection of atmospheric trace gases can reach sub-ppbv levels on-line and at second timescale [10–12]. Such highly advanced laser systems can be costly and mostly operate under laboratory conditions. One approach is the detection of ethylene with tunable diode lasers in the NIR wavelength region [13]. As the absorption strength of ethylene in this region is weak, only high concentrations can be measured and long optical path lengths are needed to improve the sensitivity. Therefore, it is more favorable to measure ethylene in the MIR wavelength region, where it presents its strongest optical absorption spectra. Here, we present a sensor for the detection of ethylene that is compact, robust, cost effective and has a low maintenance level.

In the past, high power CO<sub>2</sub> lasers were used in combination with photoacoustic spectroscopy to reach sub-ppbv levels [14]. The main advantages

of the photoacoustic detection over other laser-based techniques are its high sensitivity and background free detection. Their disadvantage is that atmospheric CO<sub>2</sub> gas absorbs at the laser lines [15, 16]. Although this can be solved by using chemical scrubbers, this limit its use of CO<sub>2</sub> laser based ethylene detectors in fruit storage facilities of greenhouses, due to its consumables, manpower and operational costs.

Since two decades, room temperature quantum cascade lasers (QCLs), operating in the MIR wavelength region, have become available [17]. Due to their low laser power, other spectroscopic techniques besides photoacoustic spectroscopy became preferable such as cavity ring-down spectroscopy (CRDS) [18, 19] and off-axis integrated cavity output spectroscopy (OA-ICOS) [20, 21]. These techniques make use of optical cavities that enhance the optical path length largely, thereby increasing its sensitivity for trace gas detection. In CRDS the lifetime of a photon inside a high finesse cavity is measured, the latter directly connected to the absorption strength of a gas [18, 19]. Within OA-ICOS the total transmitted power through a high-finesse cavity is measured [20–23].

Several groups have reported on the detection of ethylene using QCL's [24–26]. Manne et al. showed a detection limit of 5 ppbv in 10 s with an astigmatic Herriot cell with 150 m path length [24] and have reported later on 20 ppbv in 5 s using a high-finesse cavity with an optical path length of 76 m [25]. Weidmann et al. obtained a detection limit of 30 ppbv in 80 s with path length of 100 m using a Herriot cell [26]. All these results were achieved in the mid-infrared with a thermoelectrically cooled pulsed QCLs and liquid nitrogen cooled detectors. Despite these results, laser-based OA-ICOS sensors are not yet in use for monitoring ethylene from plants and fruits.

Here, we use a pulsed distributed feedback (DFB)-QCL at room temperature in combination with an OA-ICOS cell for the detection of ethylene. The radiation from the QCL is coupled into a high finesse cavity and the spectroscopic information is extracted from a measurement of the time integrated light intensity that leaks out of the cavity. We discuss the optimization of the signal-to-noise ratio based on cavity and laser parameters and report on the implementation of an optical enhancement scheme using a third mirror to couple the rejected light back into the high finesse cavity. The suitability of such a system is demonstrated for apple storage under several conditions.

## 4.2 Materials and methods

### 4.2.1 OA-ICOS

We briefly highlight the most relevant aspects of OA-ICOS, since it has been extensively reviewed in Chapter 3 and in literature [20–23]. OA-ICOS is a laser-based spectroscopic method developed from cavity ring down spectroscopy. The laser light is injected into a closed optical cavity formed by a pair of high reflectivity mirrors, meanwhile tuning over a molecular gas absorption feature of interest. The absorption strength of the gas is extracted from the time-integrated light intensity that leaks out at the backside of the cavity onto the detector. If light enters the cavity on-axis, it is only transmitted at specific wavelengths determined by the free spectral range (FSR) of the cavity. If laser light is injected off-axis into a cavity, the effective FSR of the cavity becomes smaller, determined by the number of internal reflections, before the laser light is back on its initial position. This will result in a dense spectral mode structure of the optical cavity and with a typical laser line width of a few MHz, the laser light is transmitted through the cavity without any strong power fluctuations as it would be with the on-axis configuration [21, 22]. As such, OA-ICOS takes advantage of long path absorption spectroscopy without the need of active locking to a single longitudinal cavity mode. In addition, it is also free from field interference problems inside the cavity, such as can be observed in multipass-cells. OA-ICOS reduces the complexity of the setup and improves its alignment robustness [23]; it is easy to implement, offers great versatility and selectivity, and does not require fast time-resolved measurements (CRDS) or high laser pulse energies, making it technically less demanding and more cost effective than other laser-based methods. However, there are also disadvantages of this approach: reminiscent light source intensity fluctuations can decrease the signal-to-noise ratio, and the intensity at the detector is substantially reduced due to the low throughput by the high finesse cavity. Additionally, in the wavelength region around 10  $\mu\text{m}$ , Peltier cooled infrared detectors have a limited detectivity (typical  $D^* \approx 10^9 \text{ cm Hz}^{1/2} \text{ W}^{-1}$ ). Due to this low detectivity and the low power of QCLs, the optical cavity cannot use mirrors with very high reflectivity ( $> 99,98\%$ ) but only 99,8%, which reduces the optical path length considerably (effective optical path length 150 m). As a result, the overall sensitivity of the system is reduced.

By placing an additional high reflective mirror with a small entrance hole in front of the cavity, the light reflected from the entrance mirror of the cavity is

re-injected by the third mirror into the cavity. This is particularly advantageous in the case of a small cell diameter. The absorption signal and the performance of the system can be enhanced significantly depending on various parameters of the re-injection mirror, most importantly the entrance position and angle and its distance to the cavity. In addition, the optical power throughput of the complete system is improved, thereby counteracting the low detectivity of the detector.

#### 4.2.2 Experimental setup

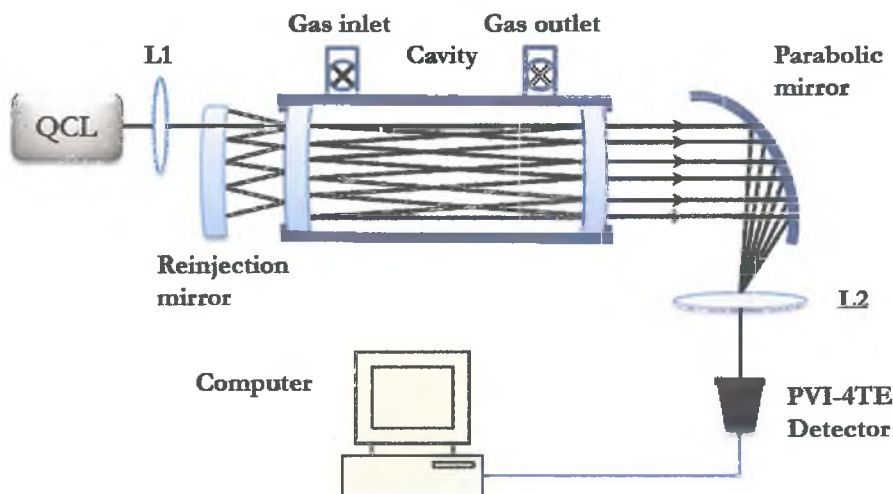


Figure 4.1: Schematic of the experimental setup. QCL: pulsed quantum cascade laser; L1, L2: focusing and collimating lens, respectively; PVI-4TE detector: four stages thermoelectrically cooled detector.

The experimental setup is shown in Fig. 4.1. A pulsed DFB-QCL with a center frequency at  $915 \text{ cm}^{-1}$  (Alpes Laser, Switzerland) was used. The room temperature laser emitted 30 ns pulses at a repetition rate of 1 MHz with a power of 3 mW. To scan the laser over  $\sim 0,25 \text{ cm}^{-1}$ , we applied the interpuls tuning method described in Section 2.2 with a bias current ramp of 4 kHz to the laser at sub-threshold level, while maintaining the pulse height. With the help of a focusing lens (ZnSe, anti-reflection coated, diameter 25,4 mm,  $f = 30 \text{ cm}$ ), the laser light was injected into the high finesse cavity formed by two spherical mirrors (diameter 50,8 mm, radius of curvature 0,5 m) with a reflectivity of  $R = 99,8\%$  at  $10,9 \text{ }\mu\text{m}$  (II-VI Infrared, Belgium). The cavity consisted of a vacuum-tight aluminum tube of 30 cm length (cell volume 0,6 l, free spectral range

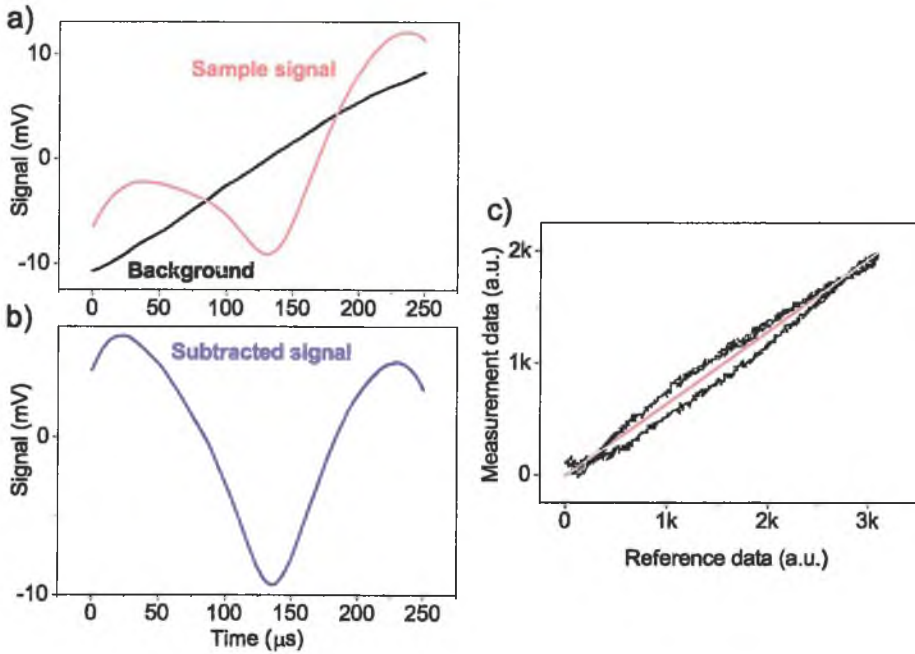


Figure 4.2: Data acquisition. Panel (a): Ethylene absorption spectrum recorded at a concentration of 1 ppmv at a cell pressure of 100 mbar. Panel (b): The background subtracted signal. Panel (c): XY-plot of the reference data against the measurement data and a subsequent linear fit (red). The slope of this fit multiplied by the reference concentration yielded the concentration of the sample.

500 MHz), which was mounted on two micrometer XY-translation stages to allow precise alignment. Gas inlet and outlet ports allowed a continuous gas exchange through the cell. Since OA-ICOS does not require an on-axis alignment, it eliminates the need for adjustable mirror mounts at both ends of the cell for parallel alignment. The optical alignment of the configuration was supported by a He-Ne laser, which was co-aligned with the QCL beam via a flip mirror.

Initially, the high finesse cell was aligned in its on-axis configuration and after that optimized for its off-axis position, using the He-Ne laser. A parabolic mirror behind the cell ( $f = 10$  cm) collected the light and a collimating lens (ZnSe, AR coated,  $f = 5$  cm) focused the light onto the thermoelectrically cooled detector (VIGO PVI-4TE-10.6, Poland, 100 MHz bandwidth,  $\tau = 6$  ns,  $D^* = 7,3 \cdot 10^9$  cm  $\text{Hz}^{1/2} \text{W}^{-1}$ ) with a built-in preamplifier. The signal of the detector was amplified by 40 dB (Femto DLPVA-100-BLN-S, Germany) and low-pass filtered at 100 kHz.

All data was sampled on a digital acquisition card (NI PCI-6259, Netherlands) and analyzed within a LabVIEW program.

To establish a background level, the cell was flushed with pure  $N_2$  gas at a pressure of 100 mbar with a flow rate of  $1 \text{ l h}^{-1}$  using a mass flow controller (Brooks Instruments, Netherlands). The response of the system was quantified using a calibrated mixture (Linde Gas Benelux, Netherlands) of 1 ppmv ( $\pm 0,05$  ppmv) of ethylene in a buffer gas of pure  $N_2$ . To obtain an absorption spectrum, the laser was scanned over  $0,2 \text{ cm}^{-1}$  of the ethylene absorption line at  $915,2 \text{ cm}^{-1}$  (Fig. 4.2(a)). A 1 ppmv reference spectrum was obtained by subtracting the  $N_2$  background from the calibrated mixture signal. To obtain the concentration from an unknown sample, the  $N_2$  background was first subtracted from the spectroscopic signal of the sample (Fig. 4.2(b)). This signal was then plotted against the 1 ppmv reference signal in a linear fit (Fig. 4.2(c)). The slope of this fit multiplied with the reference concentration gave the concentration of the sample. Since the  $N_2$  subtraction incorporates two spectra measured under identical conditions, this procedure was not particularly affected by any spectral distortion. Maintaining and monitoring the pressure of the cavity (100 mbar) ensured that the absorption line was not influenced by pressure broadening. Initially, all absorption spectra were recorded at an integration time of 1 s; at a scan frequency of 4 kHz this amounted to an average of 4000 scans. This approach allowed fast online measurement without any post-processing delay.

Ideally, for the detection of ethylene, one would target the strongest ethylene absorption line ( $8,41 \cdot 10^{-20} \text{ cm}^{-1} / (\text{molecule cm}^{-2})$ ) at  $949,65 \text{ cm}^{-1}$  [27]. However, to our present knowledge, DFB-QCLs that can access this wavelength in single mode are not commercially available. In earlier attempts, ethylene was detected at  $970 \text{ cm}^{-1}$  [24] or  $993,45 \text{ cm}^{-1}$  [25]. To avoid spectral interference with the two main constituents in air, water and  $CO_2$ , the targeted wavelength region should be chosen such that the absorption ratio  $C_2H_4/(H_2O + CO_2)$  is maximal. Therefore we chose the spectral region around  $915 \text{ cm}^{-1}$ , with low absorption of  $CO_2$  ( $2,390 \cdot 10^{-29} \text{ cm}^{-1} / (\text{molecule cm}^{-2})$ ) and  $H_2O$  ( $8,068 \cdot 10^{-27} \text{ cm}^{-1} / (\text{molecule cm}^{-2})$ ), respectively [27]. In this wavelength region, *in situ* detection of ethylene is feasible without any (chemical) pre-treatment of the sampling gas to remove interfering gases. Figure 4.3(a) shows the simulated absorption spectrum of a mixture of 1 ppmv ethylene, 3% water and 5% carbon dioxide for a path length of 1 cm and a pressure of 100 mbar at  $915 \text{ cm}^{-1}$ ,  $970 \text{ cm}^{-1}$  and  $993 \text{ cm}^{-1}$ . The chosen concentrations of water and  $CO_2$  are high, because of their typical values in greenhouses and fruit storage chambers. The calculation is based on

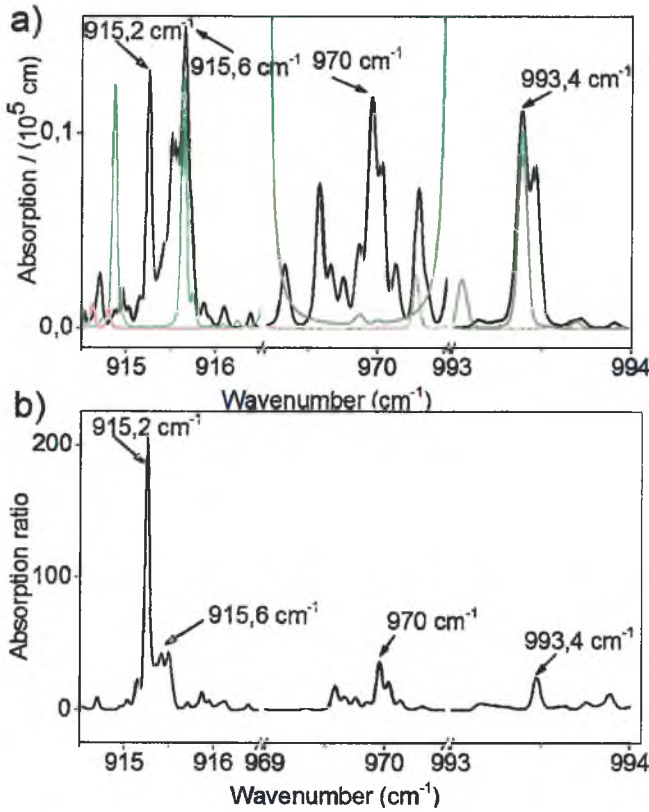


Figure 4.3: Panel (a): Simulated absorption spectra of 1 ppmv ethylene (black), 3% H<sub>2</sub>O (red) and 5% CO<sub>2</sub> (green) spectra at 915 cm<sup>-1</sup>, 970 cm<sup>-1</sup> and 993 cm<sup>-1</sup> for a path length of 1 cm at 100 mbar based on the HITRAN 2008 database. Panel (b): the absorption ratio of ethylene with H<sub>2</sub>O and CO<sub>2</sub> at these three wavelengths.

the HITRAN 2008 database [27]. The ethylene line at 915,2 cm<sup>-1</sup> (integrated line strength is  $1,929 \cdot 10^{-20}$  cm<sup>-1</sup> / (molecule cm<sup>-2</sup>)) has an absorption ratio of  $C_2H_4/(H_2O + CO_2) = 200$  (panel 4.3(b)), which is four times better than the ratio at the other wavelengths used in previous OA-ICOS experiments and thus adequate for our experiments. The absorption line of CO<sub>2</sub> at 914 cm<sup>-1</sup> was used for frequency calibration of the system.

### 4.2.3 Optical enhancement

To simulate the effect of the re-injection mirror on the throughput power of the system, we used a ray trace approach through all three mirrors, depending on

the initial position  $x, y$ , the incoming angle  $\alpha_x, \alpha_y$  and the distance  $d$  between the re-injection mirror and the cavity. The re-injection mirror had identical properties compared to the cavity mirrors and its radius of curvature was greater than the distance  $d$ . The re-injection mirror and the entrance mirror of the cavity comprised a second optical cavity formed by a positive and a negative mirror. The corresponding ray trace matrices for these optical elements were:

$$s = \begin{pmatrix} x \\ \alpha_x \\ y \\ \alpha_y \end{pmatrix}; \quad T(d) = \begin{pmatrix} 1 & d & 0 & 0 \\ 0 & 1 & 0 & 0 \\ 0 & 0 & 1 & d \\ 0 & 0 & 0 & 1 \end{pmatrix}; \quad T(r) = \begin{pmatrix} 1 & 0 & 0 & 0 \\ \frac{-2}{r} & 1 & 0 & 0 \\ 0 & 0 & 1 & 0 \\ 0 & 0 & \frac{-2}{r} & 1 \end{pmatrix} \quad (4.2.1)$$

where  $s$  represented the vector containing the position and angle of the beam in  $x$ - and  $y$ -direction,  $T(d)$  translated the beam over a distance  $d$  and  $T(r)$  reflected the beam off a mirror with radius of curvature  $r$ . Starting at the re-injection mirror at coordinates  $(x, \alpha_x, y, \alpha_y)$ , we first translated the beam towards the cavity entrance mirror over a distance  $d$  by  $s_1 = T(d) \cdot s_0$ . For each beam, which entered the cavity, the ray trace recursively calculated its path through the cavity until it either fulfilled the re-entrant condition or hit the walls of the cavity. A single pass through the cavity was calculated by  $s_2 = T(r_2) \cdot T(L) \cdot T(r_3) \cdot T(L) \cdot s_1$ , where  $L$  is the cavity length and  $r_2$  and  $r_3$  are the radii of curvature of the first and second cavity mirror, respectively. The total distance until reaching the re-entrant condition divided by the speed of light  $c$  yielded the round trip time. This number was then divided by the cavity ring down time  $\tau_0 = n/c \cdot L/(1 - R)$  ( $R$  the reflectivity of the mirrors and  $n$  the refractive index) yielding the number of round trips  $m$  inside of the cavity. The subsequent matrix calculations after one reflection off the entrance cavity mirror were  $s_2 = T(r_1) \cdot T(d) \cdot T(-r_2) \cdot s_1$ , where  $d$  is the distance between the re-injection mirror and the cavity and  $r_1$  and  $r_2$  are the radii of curvature of the re-injection mirror and the first cavity mirror, respectively. The minus sign occurs from the fact that the beam reflects off the back side of a concave mirror. To determine how many reflections  $n$  between these two mirrors occurred, this calculation ran recursively until the beam either exited through the incoming hole or did not enter the cavity. The average transmitted power by an off-axis cavity is given by Eq. 3.3.16 [23]:

$$I = I_0 C \frac{(1 - R)^2}{2[(1 - R) + kL]} \quad (4.2.2)$$

where  $I_0$  is the initial laser power,  $R$  the reflectivity of the mirrors (assuming  $R_1 = R_2 = R$ ),  $C$  is a cavity coupling parameter (between 0 and 1), and  $k$  is the absorption coefficient. The coupling parameter represents the ratio of the number of round trips and the cavity finesse  $\mathcal{F}$ :  $C_i = m_i/\mathcal{F}$ , where the round trips were determined by the ray trace as described above. Beams exiting the cavity towards the re-injection mirror were not taken into account for the power calculation as the power leaking out of the front of the cavity was below the microwatt region and once re-injected would not contribute significantly to the total transmitted power.

The re-injection can not only contribute to the signal, but also to the noise as the laser light contains noise by itself and additional noise from diffractions or etalons may arise. Including all possible noise sources would increase the calculation time and counter the practicality of this approach. We thus define the enhancement as the ratio of transmitted power in the presence and absence of the re-injection mirror. In this case, Eq. 4.2.2 changes only with respect to the coupling constant  $C$  and we linked it to the number of re-injections by giving it a superscript  $i$ , with zero being the case without enhancement. If we take the fraction from Eq. 4.2.2 and define it as a new constant  $K = (1 - R)^2 / [(1 - R) + kL]$ , the ratio of the total transmitted power of  $n$  injections compared to zero re-injections can be written as

$$P_{\text{enhanced}} = \frac{I^{i=n}}{I^{i=0}} = \frac{KI_0 \sum_{i=0}^n R^{2i} C_i}{KI_0 C_0} = \frac{\sum_{i=0}^n R^{2i} m_i}{m_0} \quad (4.2.3)$$

Since the absorption path length inside the cell did not change, we could calculate this ratio as if there was no absorber present in the cavity. This ratio only represents the enhancement in signal, since the noise may have increased as well as a result of increased laser noise or etalon effects.

#### 4.2.4 Application to apple storage

The conditions, under which apples are stored in CA, differ substantially from normal air (in respect to  $\text{CO}_2$  and  $\text{O}_2$  concentrations) and temperature levels. These conditions have been proven to be beneficial for maintaining harvested fruit quality and delaying ripening [28, 29]. For Elstar apples, typical CA conditions of 2%  $\text{O}_2$ , 5%  $\text{CO}_2$  and 0°C are used. In our set-up, the apples were stored individually in glass cuvettes. The cuvettes were connected to a valve system (VC-6, Sensor Sense, Netherlands), which provided a constant

gas flow over the apples and automatic switching between the cuvettes. The  $O_2$  and  $CO_2$  levels in the cuvettes were established by a flow-through system, mixing  $N_2$  (93%),  $O_2$  (2%) and  $CO_2$  (5%) at  $5\text{ l h}^{-1}$  via mass flow controllers (Brooks Instruments). Initial measurements were performed at  $0^\circ\text{C}$ . Each cuvette was measured for 20 minutes and the data averaged over the last 10 minutes. The experiment was repeated four times and averaged, where the resulting ethylene concentration was expressed in emission rate per weight,  $\mu\text{l h}^{-1}\text{ g}^{-1}$ . For comparison and validation was a commercial laser-based photoacoustic ethylene detector ETD-300 (Sensor Sense, Netherlands) used.

## 4.3 Results

### 4.3.1 Instrumental optimization

The scanning range capability of the pulsed QCL was measured with a Germanium etalon (free spectral range of  $\sim 0,049\text{ cm}^{-1}$ ) in between the laser and the detector. The resulting fringe pattern showed a frequency coverage of  $\sim 0,25\text{ cm}^{-1}$ . For the detection of ethylene, we investigated the improvement of the signal-to-noise ratio (SNR) as function of the off-axis distance of the entrance laser beam without re-injection mirror. To perform off-axis measurements, firstly the cell was aligned on-axis, after this both ends of the cell were translated vertically over a specific distance (in the same direction) and subsequently translated horizontally for double this distance (in opposite directions from each other). In such a way we achieved a circular pattern of laser spots on the high reflective mirrors of the optical cavity. Various off-axis alignment distances were applied and the results are shown in Fig. 4.4(a). For this study, a gas mixture of 10 ppmv of  $C_2H_4$  in  $N_2$  at 100 mbar pressure was used. Each data point was recorded with a scanning rate of 4 kHz and an integration time of 1 s. A  $3\sigma$  value calculated from the  $N_2$  measurements was used as noise level, while the calculated concentration was used as the signal value. Figure 4.4(a) depicts the SNR as a function of the off-axis diameter. At diameters larger than 45 mm, the injected light did not eject fully and thus determined the upper limit for off-axis alignment. The SNR could be improved by increasing the scan rate of the laser. Figure 4.4(b) illustrates the results of various scanning rates between 200 Hz and 4 kHz at a fixed off-axis diameter of 45 mm. The noise decreased clearly with higher scanning frequency within a fixed integration time of 1 s. Increasing the scanning rate to more than 4 kHz did not improve the SNR due to increasing

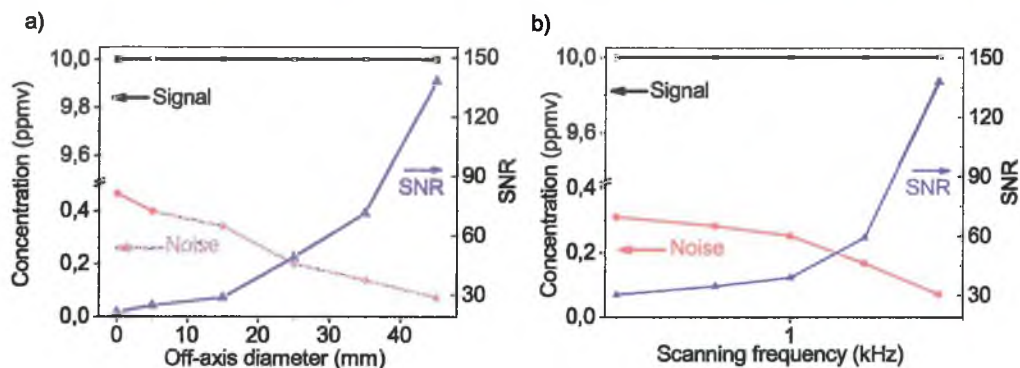


Figure 4.4: Optimization of signal-to-noise ratio (SNR). SNR (triangles, right scale) based on ratio of the signal (squares, left scale) and the noise (circles, left scale) depending on the off-axis alignment parameter at a fixed scanning rate of 4 kHz (panel (a)) and depending on the scanning rate at a fixed off-axis alignment parameter of 45 mm (panel (b)). Signal values were based on the measured concentrations and noise values were based on a  $3\sigma$  value calculated from the background measurements.

delays in the acquisition card. Based on these results, the optimal values for the systems were an off-axis diameter of 45 mm and a scanning rate of 4 kHz to achieve a SNR of 140.

To test the linearity of the system, various mixing ratios of ethylene were measured at a pressure of 100 mbar (each data point represents 10 averages with an acquisition time of 1 min); a linear fit of these measurements is displayed in Fig. 4.5. The measured concentrations agree with the calculated ones within an error of 3% and indicate a linear behavior in the dynamic range of 10 ppbv to 100 ppmv.

The influence of frequency chirp of the pulsed QCL on the sensitivity and accuracy of concentration measurements has been studied in detail [30–32]. In general, injected laser current causes heat during a pulse, which leads to an increased effective laser line width. This can be overcome by using an absorption feature, which is broader than the range covered by the laser pulse and by calibrating the system with a known concentration. Our QCL showed a chirp rate of  $0,005 \text{ cm}^{-1} \text{ ns}^{-1}$  measured with a Germanium etalon ( $\text{FSR} = 0,049 \text{ cm}^{-1}$ ) for pulses ranging from 25 ns to 100 ns (see Fig. 4.6). The total chirp was  $0,15 \text{ cm}^{-1}$  for a pulse of 30 ns, which was smaller than the absorption feature of interest, while the laser provided sufficient power. In addition, we performed a

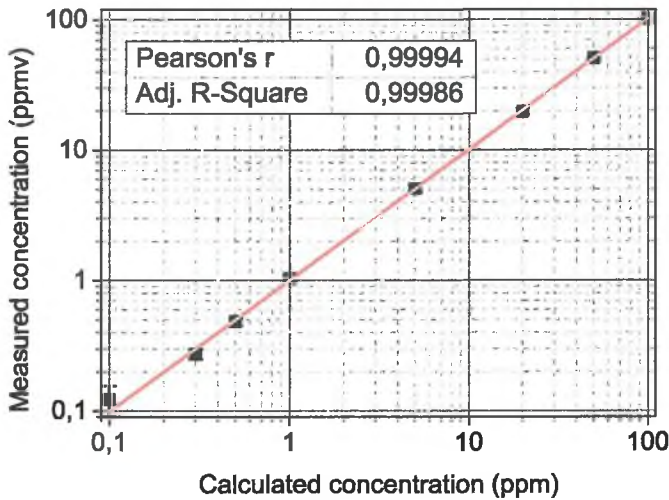


Figure 4.5: Calibration curve. Various calculated concentrations from the mixing ratios of ethylene with nitrogen are plotted against their measured counterpart (10 averages with 1 min acquisition time, pressure 100 mbar) and linearly fitted. The  $3\sigma$  values of the averaged concentration values are shown as error bars.

calibration before an experiment to overcome the influence of the chirp of the QCL.

#### 4.3.2 Optical enhancement and sensitivity

To verify the effect of the re-injection mirror, we measured the power ratio transmitted through the cavity in the absence and presence of a re-injection mirror in front of the cavity. The distance between the re-injection mirror and the cavity was 15 cm (radius of curvature 0,5 m). The initial light beam passed through a small hole (diameter 1,5 mm) in the re-injection mirror and only a fraction was coupled into the optical cavity. The remaining light was reflected back by the first cavity mirror and redirected to the cavity by the re-injection mirror. The light beam between the re-injection mirror and the first mirror of the cavity underwent a series of reflections, until it coupled back through the hole in the re-injection mirror or reached the edge of one of the mirrors. As such, the number of reflections was finite. A He-Ne laser was used to make the reflections optically visible and to confirm the multiple re-injections. This

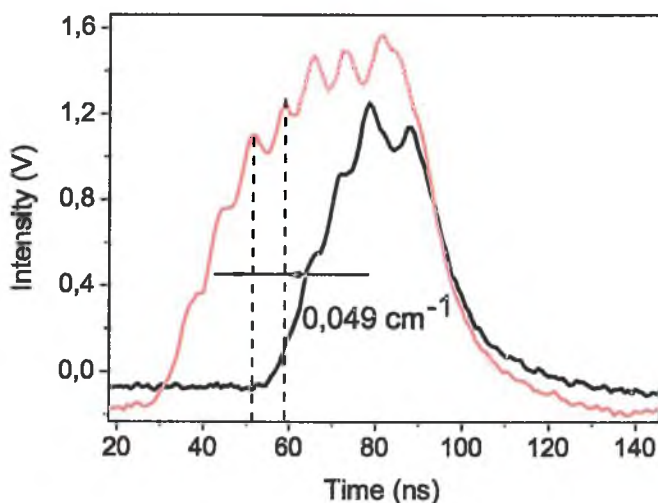


Figure 4.6: QCL chirp. For a pulse duration of 50 ns (red) and of 25 ns (black) using a Germanium etalon ( $\text{FSR} = 0,049 \text{ cm}^{-1}$ ). The chirp rate amounted to  $0,005 \text{ cm}^{-1} \text{ ns}^{-1}$ .

effectively increased the net optical power coupled into the cavity and greatly enhanced the output power using the off-axis design. Careful adjustment of the off-axis parameter and the optical feedback into the cavity gained an optimum trade-off between signal enhancement and noise increase.

To study the effect of the re-injection mirror on the overall sensitivity of the system, we used a QCL at a wavelength of  $965 \text{ cm}^{-1}$  with comparable line width and power to the one at  $915 \text{ cm}^{-1}$ ; at this wavelength ethylene has an integrated absorption line strength of  $5,10 \cdot 10^{-21} \text{ cm}^{-1} / (\text{molecule cm}^{-2})$ . Also, at this wavelength the mirror reflectivity reduced to 99,6%, which resulted in an effective optical path length of 75 m in the 30 cm long cavity. Figure 4.7(a) shows the calculated (circles) and measured (squares) data power ratio (transmission in the absence and presence of the re-injection mirror) calculated from Eq. 4.2.3 as a function of the off-axis parameter with a re-injection mirror. At each off-axis diameter, the re-injection mirror was repositioned and its angle adjusted to yield the maximum throughput. The experimental data agrees largely with the calculated data with a maximum of 20% difference around 30 mm. The re-injection mirror could not efficiently couple the re-injected light through the cavity at larger off-axis diameter, as a result the transmission dropped. In

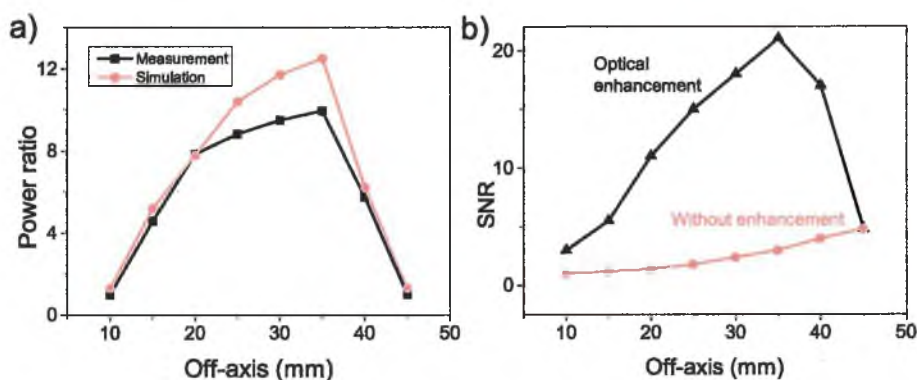


Figure 4.7: Optical enhancement. Panel (a): Comparison of calculated (circles) and measured (squares) power ratio based on different off-axis diameters. For small and large diameters the measurements agree with the predictions whereas they show a discrepancy of up to 20% between 25 mm and 35 mm. Panel (b): Comparison of SNR from the OA-ICOS system at  $965\text{ cm}^{-1}$  with optical enhancement (upper curve, diamonds) and without (lower curve, triangles). The sensitivity was increased by a factor 4 and was limited by the loss of transmitted re-injected light at larger off-axis diameter.

addition, there was a growing uncertainty in the number of reflected spots as this number increased due to partial overlap of the spots. The number of re-injections corresponding to the maximum transmission was estimated to be  $\sim 30$ . Figure 4.7(b) shows a comparison between the SNR of a measurement of 1 ppmv ethylene with and without optical enhancement. The two curves compare single-injection (triangles) of the light into the cavity and the improvement with optical enhancement (diamonds). Using a concentration of 1 ppmv at a wavelength of  $965\text{ cm}^{-1}$ , the maximum SNR was 4,8 in the case of standard OA-ICOS. Recalculated to the previously described wavelength of  $915\text{ cm}^{-1}$  this was equivalent to a SNR of 10. Using the re-injection mirror the SNR increased nearly linearly to a factor 21 at 30 mm. As the power ratio dropped off for larger off-axis diameter, the SNR reached its maximum at 30 mm and reached the same value for 45 mm as for standard OA-ICOS. Comparing the highest SNR in both cases independent of the off-axis parameter, we find that the overall gain in SNR was about a factor 4.

We estimated the stability of the system over time by calculating the Allan deviation [33]. In Fig. 4.8, the detection limit decreases as a function of averaging time. The detection limit of the QCL-based sensor at  $915\text{ cm}^{-1}$  was 108 ppbv of

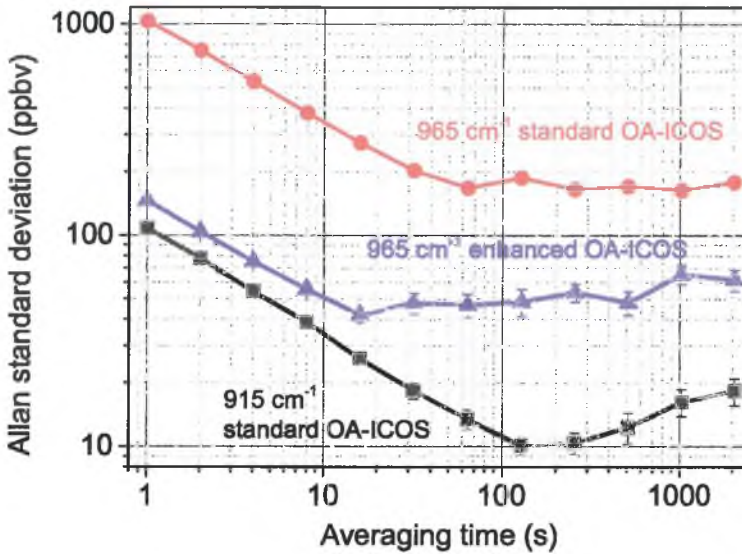
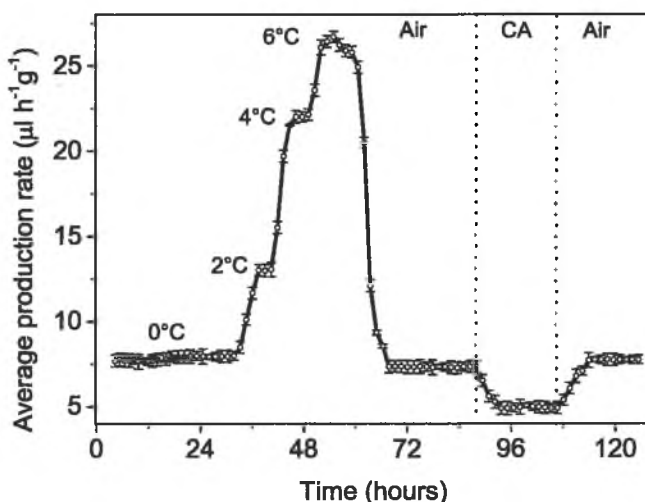


Figure 4.8: Allan deviation to determine the detection limit as a function of the integration time. A detection limit of 108 ppbv for a 1 s average was achieved for the laser at  $915\text{ cm}^{-1}$  (lower curve, squares). The best detection limit of 10 ppbv was reached for a 128 s acquisition time. The two other curves show the effect of the optical enhancement on the sensitivity for the laser at  $965\text{ cm}^{-1}$ . The upper curve (circles) show a detection limit of 180 ppbv in 128 s, which was enhanced by a factor 4 down to 45 ppbv in 16 s (middle curve, triangles).

ethylene for a 1 s average ( $3\sigma$ -value) in the case of no re-injection mirror (lower curve, squares). We achieved better sensitivity values using longer integration times, e.g., 10 ppbv for 128 s. This translates to a NEAS of about  $1,5 \cdot 10^{-7}\text{ cm}^{-1}\text{ Hz}^{-1/2}$ . To verify the enhancement in SNR by the modified OA-ICOS scheme, we also plotted the Allan deviations of the laser at  $965\text{ cm}^{-1}$  with and without re-injection mirror. The upper curve (circles) shows a detection limit of 180 ppbv in 128 s for standard OA-ICOS, whereas it reached 45 ppbv in 16 s in the case of enhancement (middle curve, triangles). The detection limit thus was enhanced by a factor 4 in agreement with the improvement in SNR and could not be further increased mainly due to noise and temperature fluctuations of the detector. It is possible to further increase the number of re-injections using differently shaped mirrors, for example astigmatic mirrors, before the optical

beam exits the hole in the re-injection mirror. Further investigations of optimal parameters and enhancement are subject to a future publication.

### 4.3.3 Application to apple storage



**Figure 4.9:** Dynamics of the average production rate of all Elstar apples over 120 h. The values are means of the production rate of four repeated experiments. The temperature was first kept constant at 0°C and then varied to 6°C in steps of 2°C and back to 0°C again. The emission levels reached three plateaus at these temperatures. The conditions were switched to CA after 86 h and back to air after 108 h.

The dynamics of the ethylene production of commercially available Elstar apples stored in glass cuvettes is shown in Fig. 4.9. Ethylene production was simultaneously measured by the QCL-based system and the commercial laser-based ethylene detector ETD-300. The apples were first kept in air at a temperature of 0°C for a period of 1 day. Constant emission of at a rate of  $7,8 \pm 0,8 \mu\text{l h}^{-1} \text{g}^{-1}$  was detected after 30 hours at the same temperature. When the temperature was raised to 6°C in steps of 2°C in the next 24 hours, the ethylene production rate increased from  $13,0 \pm 0,9 \mu\text{l h}^{-1} \text{g}^{-1}$  (2°C) to  $22 \pm 0,8 \mu\text{l h}^{-1} \text{g}^{-1}$  (4°C) and to  $26 \pm 0,9 \mu\text{l h}^{-1} \text{g}^{-1}$  (6°C), respectively. After 60 hours the temperature was again reduced to 0°C and the ethylene levels dropped to  $7,4 \pm 0,8 \mu\text{l h}^{-1} \text{g}^{-1}$  over a period of 10 hours. They even decreased more to

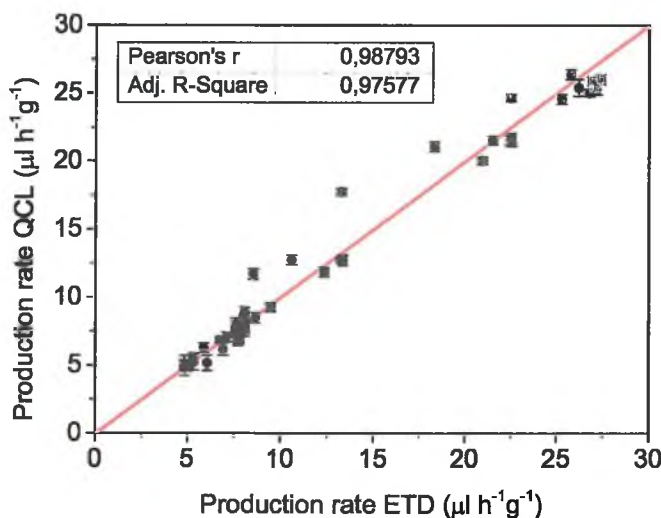


Figure 4.10: Correlation between QCL-based and photoacoustic system (ETD-300) as a function of the measured ethylene production rate. The linear fit provided a Pearson factor of  $r = 0,988$ .

$5 \pm 0,8 \mu\text{l h}^{-1} \text{g}^{-1}$ , when CA conditions were established (2%  $\text{O}_2$ , 5%  $\text{CO}_2$ ). Figure 4.10 shows a Pearson coefficient of  $r = 0,988$  and an adjusted R-square of  $\bar{R}^2 = 0,976$  for the level of agreement between the two laser based systems.

## 4.4 Discussion

Ideally, an ethylene sensor should be fast, sensitive and high selectivity, compact and maintenance free. Figure 4.11 shows a comparison between different sensors based on the data of Cristescu et al. [34]. Gas chromatographs, electrochemical sensors and laser-based sensors are compared in terms of sensitivity (x-axis), response time (y-axis) and price (z-axis), while the colors indicate the prices for existing commercial devices. The system presented here has measured ethylene in real time in agreement with a commercial ETD-300 device (see Fig. 4.10). This means that the system is insensitive to interfering gases such as  $\text{CO}_2$  and water. The ability to follow the emission of ethylene over several days strongly suggests that the combination of OA-ICOS and a QCL is especially suited for storage conditions over long time due to the robustness of the technique, the enhanced path length and the high absorption ratio.

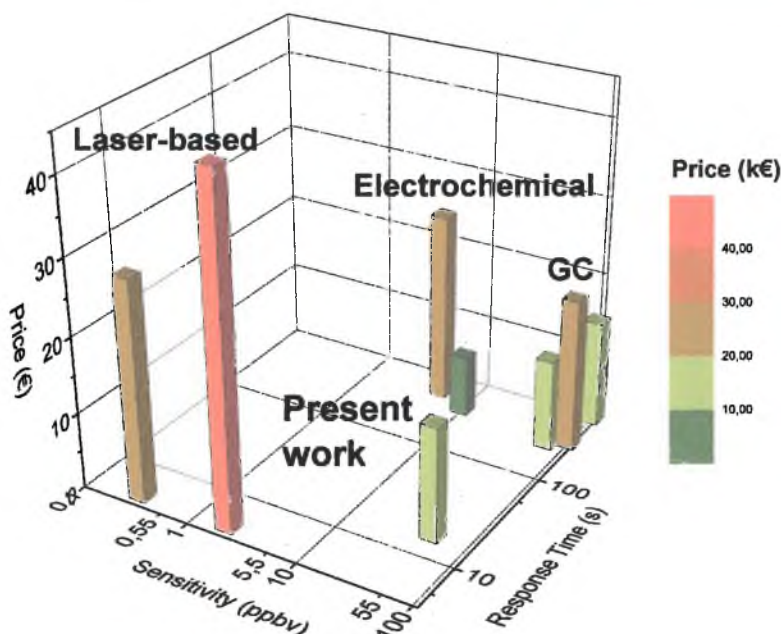


Figure 4.11: Comparison of the costs of commercial gas chromatographs (GC), electrochemical sensors and laser-based systems. These systems are compared in terms of sensitivity (x-axis), response time (y-axis) and price (z-axis) to the component price of the OA-ICOS system presented here.

We successfully implemented an optical enhancement scheme to overcome the low power output of the cavity enhanced spectroscopy technique. A gain of four times in SNR for the laser at  $965\text{ cm}^{-1}$  was achieved and the enhancement was found to be dependent on the laser power, off-axis diameter and relative position of the re-injection mirror to the cavity. This enables us to estimate the enhanced detection limit at  $915\text{ cm}^{-1}$ . Since this laser had comparable power and the absorption path length in the cell did not change, we should have reached at least an improvement of a factor 4, leading to a detection limit of  $\sim 2\text{ ppbv}$ .

As stated before, currently laser-based OA-ICOS sensors are not yet in use for monitoring ethylene from fruits and plants. This mainly arises from the practicality of such systems under the circumstances in field use, where for example ease-of-use, power consumption and response time are important next to sensitivity. Photoacoustics still surpasses the detection limits achieved with QCLs, but relies on the chemical removal of interfering gases. Previous studies with QCLs and multipass cells or OA-ICOS achieved sensitivities ranging

from 5 ppbv to 30 ppbv, which utilized liquid nitrogen cooling on both laser and detector. We have achieved a detection limit comparable to previously reported QCL-based systems for the detection of ethylene [24–26] due to the nearly identical path lengths and absorption strengths. More importantly, we succeeded in building a system with a significant reduction of requirements and complexity for *in situ* measurements, making it compact and usable in fruit storage conditions. The detection system was insensitive to interfering gases, required only external power and a gas calibration. The detector and the QCL did not require any water or liquid nitrogen cooling. The QCL remained the most expensive part of the setup, but was still significantly cheaper than other sensors like a gas chromatograph. Additionally, the small tuning range of the QCL limited the system to single gas detection. The limited availability of fast, sensitive and thermoelectrically cooled detectors at 10  $\mu\text{m}$  is another drawback compared to the near infrared or telecom region. The main limitation of our sensor was the fast photodiode, which picked up electronic noise and detects the individual pulses of the laser. We thus needed to electronically filter the signal in order to acquire the slope of the absorption line.

## 4.5 Conclusion

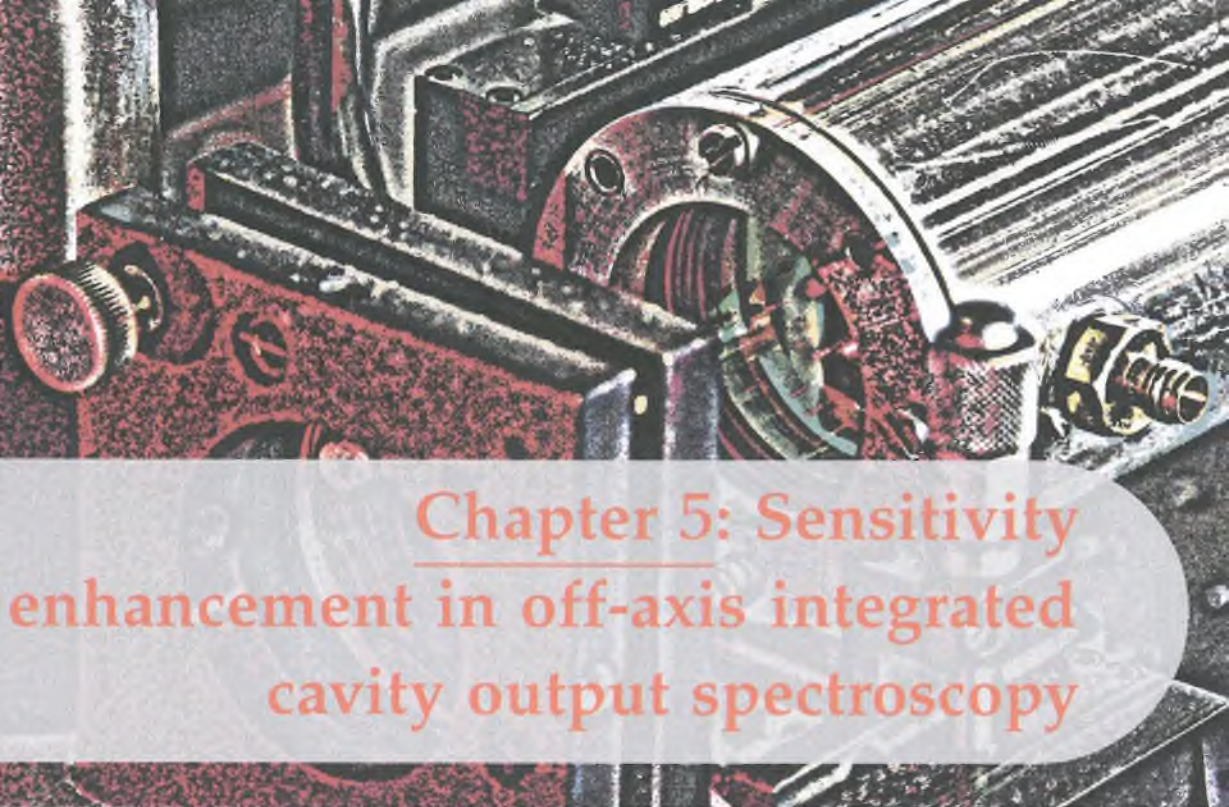
We have demonstrated that the combination of OA-ICOS with a pulsed QCL (at  $915\text{ cm}^{-1}$ ) provides an easy, robust, low maintenance and cost-effective tool for the measurement of low ethylene concentrations in the presence of high  $\text{CO}_2$  and water levels as present in storage facilities. In particular, we optimized the off-axis diameter of the cavity and the scanning rate of the laser and achieved a signal-to-noise ratio of 140. The system was a stand-alone unit independent of additional cooling liquids requiring only external power. When we compared our detection system to a commercial photoacoustic detector, the two systems showed a good agreement. Furthermore, our OA-ICOS system provided real-time measurements of ethylene with a high finesse cavity yielding 10 ppbv in 128 s averaging time, which is equal to a NEAS of  $1,5 \cdot 10^{-7}\text{ cm}^{-1}\text{Hz}^{-1/2}$ . The effect of controlled atmosphere conditions on the ethylene production of apples was successfully measured, showing its applicability to fruit storage. The sensitivity of the OA-ICOS system was enhanced by a factor 4 by using a re-injecting mirror to reflect the light into the cavity. An optimized re-injection approach will be published in a future paper.

# References

- [1] A. B. Bleecker and H. Kende, "Ethylene: A gaseous signal molecule in plants," *Annual Review of Cell and Developmental Biology*, vol. 16, no. 1, pp. 1–18, 2000.
- [2] A. A. Kader, *Postharvest technology of horticultural crops*, vol. 3311. UCANR Publications, 2002.
- [3] S. Cristescu, S. Persijn, S. te Lintel Hekkert, and F. Harren, "Laser-based systems for trace gas detection in life sciences," *Applied Physics B*, vol. 92, no. 3, pp. 343–349, 2008.
- [4] D. Arslanov, M. Spunei, A. Ngai, S. Cristescu, I. Lindsay, S. Persijn, K. Boller, and F. Harren, "Rapid and sensitive trace gas detection with continuous wave optical parametric oscillator-based wavelength modulation spectroscopy," *Applied Physics B*, vol. 103, no. 1, pp. 223–228, 2011.
- [5] A. A. Kosterev *et al.*, "Chemical sensors based on quantum cascade lasers," *Quantum Electronics, IEEE Journal of*, vol. 38, no. 6, pp. 582–591, 2002.
- [6] J. R. Gorny and A. Kader, "Ethylene monitoring equipment performance tests," *Perishables Handling Quarterly*, vol. 97, pp. 25–26, 1999.
- [7] H. Pham-Tuan, J. Vercammen, C. Devos, and P. Sandra, "Automated capillary gas chromatographic system to monitor ethylene emitted from biological materials," *Journal of Chromatography A*, vol. 868, no. 2, pp. 249–259, 2000.
- [8] A. Sklorz, S. Janßen, and W. Lang, "Detection limit improvement for NDIR ethylene gas detectors using passive approaches," *Sensors and Actuators B: Chemical*, vol. 175, pp. 246–254, 2012.
- [9] L. Jordan, P. Hauser, and G. Dawson, "Portable trap-sensor system for monitoring low levels of ethylene," *Analyst*, vol. 122, no. 8, pp. 811–814, 1997.
- [10] M. A. Zevenbergen, D. Wouters, V. A. T. Dam, S. H. Brongersma, and M. Crego-Calama, "Electrochemical sensing of ethylene employing a thin ionic-liquid layer," *Analytical Chemistry*, vol. 83, no. 16, pp. 6300–6307, 2011.
- [11] O. Green, N. A. Smith, A. B. Ellis, and J. N. Burstyn, "AgBF<sub>4</sub>-impregnated poly(vinyl phenyl ketone): An ethylene sensing film," *Journal of the American Chemical Society*, vol. 126, no. 19, pp. 5952–5953, 2004.
- [12] B. Esser and T. M. Swager, "Detection of ethylene gas by fluorescence turn-on of a conjugated polymer," *Angewandte Chemie*, vol. 122, no. 47, pp. 9056–9059, 2010.
- [13] J. Zhang, K. Song, *et al.*, "Tunable diode laser absorption spectroscopy system for trace ethylene detection," *Spectroscopy and Spectral Analysis*, vol. 32, no. 10, pp. 2875–2878, 2012.

- [14] H. De Vries, M. Wasono, F. Harren, E. Woltering, H. Van der Valk, and J. Reuss, "Ethylene and CO<sub>2</sub> emission rates and pathways in harvested fruits investigated, *in situ*, by laser photothermal deflection and photoacoustic techniques," *Postharvest Biology and Technology*, vol. 8, no. 1, pp. 1–10, 1996.
- [15] F. Harren, F. Bijnen, J. Reuss, L. Voesenek, and C. Blom, "Sensitive intracavity photoacoustic measurements with a CO<sub>2</sub> waveguide laser," *Applied Physics B*, vol. 50, no. 2, pp. 137–144, 1990.
- [16] E. J. Woltering, F. Harren, and H. A. Boerrigter, "Use of a laser-driven photoacoustic detection system for measurement of ethylene production in cymbidium flowers," *Plant Physiology*, vol. 88, no. 2, pp. 506–510, 1988.
- [17] J. Faist, F. Capasso, D. L. Sivco, A. L. Hutchinson, C. Sirtori, and A. Y. Cho, "Quantum cascade laser: A new optical source in the mid-infrared," *Infrared Physics & Technology*, vol. 36, no. 1, pp. 99–103, 1995.
- [18] J. Morville, S. Kassi, M. Chenevier, and D. Romanini, "Fast, low-noise, mode-by-mode, cavity-enhanced absorption spectroscopy by diode-laser self-locking," *Applied Physics B*, vol. 80, no. 8, pp. 1027–1038, 2005.
- [19] R. Engeln, G. Berden, R. Peeters, and G. Meijer, "Cavity enhanced absorption and cavity enhanced magnetic rotation spectroscopy," *Review of Scientific Instruments*, vol. 69, no. 11, pp. 3763–3769, 1998.
- [20] E. Moyer, D. Sayres, G. Engel, J. S. Clair, F. Keutsch, N. Allen, J. Kroll, and J. Anderson, "Design considerations in high-sensitivity off-axis integrated cavity output spectroscopy," *Applied Physics B*, vol. 92, no. 3, pp. 467–474, 2008.
- [21] G. S. Engel, W. S. Drisdell, F. N. Keutsch, E. J. Moyer, and J. G. Anderson, "Ultrasensitive near-infrared integrated cavity output spectroscopy technique for detection of CO at 1.57  $\mu\text{m}$ : New sensitivity limits for absorption measurements in passive optical cavities," *Applied Optics*, vol. 45, no. 36, pp. 9221–9229, 2006.
- [22] D. S. Baer, J. B. Paul, M. Gupta, and A. O'Keefe, "Sensitive absorption measurements in the near-infrared region using off-axis integrated cavity output spectroscopy," in *International Symposium on Optical Science and Technology*, pp. 167–176, International Society for Optics and Photonics, 2002.
- [23] J. B. Paul, L. Lapson, and J. G. Anderson, "Ultrasensitive absorption spectroscopy with a high-finesse optical cavity and off-axis alignment," *Applied Optics*, vol. 40, no. 27, pp. 4904–4910, 2001.
- [24] J. Manne, W. Jäger, and J. Tulip, "Sensitive detection of ammonia and ethylene with a pulsed quantum cascade laser using intra and interpulse spectroscopic techniques," *Applied Physics B*, vol. 94, no. 2, pp. 337–344, 2009.

- [25] J. Manne, A. Lim, W. Jäger, and J. Tulip, "Off-axis cavity enhanced spectroscopy based on a pulsed quantum cascade laser for sensitive detection of ammonia and ethylene," *Applied Optics*, vol. 49, no. 28, pp. 5302–5308, 2010.
- [26] D. Weidmann, A. A. Kosterev, C. Roller, R. F. Curl, M. P. Fraser, and F. K. Tittel, "Monitoring of ethylene by a pulsed quantum cascade laser," *Applied Optics*, vol. 43, no. 16, pp. 3329–3334, 2004.
- [27] L. S. Rothman, I. E. Gordon, A. Barbe, D. C. Benner, P. F. Bernath, M. Birk, V. Boudon, L. R. Brown, A. Campargue, J. P. Champion, *et al.*, "The HITRAN 2008 molecular spectroscopic database," *Journal of Quantitative Spectroscopy and Radiative Transfer*, vol. 110, no. 9, pp. 533–572, 2009.
- [28] Y. S. Wang, S. P. Tian, and Y. Xu, "Effects of high oxygen concentration on pro-and anti-oxidant enzymes in peach fruits during postharvest periods," *Food Chemistry*, vol. 91, no. 1, pp. 99–104, 2005.
- [29] S. P. Tian, B. Q. Li, and Y. Xu, "Effects of O<sub>2</sub> and CO<sub>2</sub> concentrations on physiology and quality of litchi fruit in storage," *Food Chemistry*, vol. 91, no. 4, pp. 659–663, 2005.
- [30] S. Welzel, G. Lombardi, P. Davies, R. Engeln, D. Schram, and J. Röpcke, "Trace gas measurements using optically resonant cavities and quantum cascade lasers operating at room temperature," *Journal of Applied Physics*, vol. 104, no. 9, p. 093115, 2008.
- [31] J. Manne, O. Sukhorukov, W. Jäger, and J. Tulip, "Pulsed quantum cascade laser-based cavity ring-down spectroscopy for ammonia detection in breath," *Applied Optics*, vol. 45, no. 36, pp. 9230–9237, 2006.
- [32] O. Sukhorukov, A. Lytkine, J. Manne, J. Tulip, and W. Jäger, "Cavity ring-down spectroscopy with a pulsed distributed feedback quantum cascade laser," in *Integrated Optoelectronic Devices 2006*, p. 61270A, International Society for Optics and Photonics, 2006.
- [33] D. W. Allan, "Statistics of atomic frequency standards," *Proceedings of the IEEE*, vol. 54, no. 2, pp. 221–230, 1966.
- [34] S. M. Cristescu, J. Mandon, D. Arslanov, J. De Pessemier, C. Hermans, and F. J. Harren, "Current methods for detecting ethylene in plants," *Annals of Botany*, vol. 111, no. 3, pp. 347–360, 2013.



## Chapter 5: Sensitivity enhancement in off-axis integrated cavity output spectroscopy

This chapter is based on:

R. Centeno, J. Mandon, S.M. Cristescu, F.J.M. Harren, *Sensitivity enhancement in off-axis integrated cavity output spectroscopy*, Optics Express, 22, 23, 27985 – 27991 (2014), <http://dx.doi.org/10.1364/OE.22.027985>

## Abstract

We report on a detailed model of an improved three mirror off-axis integrated cavity output spectroscopy (OA-ICOS) setup, which re-injects the light reflected by the optical cavity. The model simulates the impact of the design parameters on instrument sensitivity and can be used for any off-axis configuration. We demonstrate the application of this model for the real-time detection of ethylene with a pulsed quantum cascade laser. The three mirror OA-ICOS scheme provides a 10 times increase in signal-to-noise ratio as compared to standard OA-ICOS, resulting in a noise equivalent absorption sensitivity (NEAS) per point of  $1,5 \cdot 10^{-8} \text{ cm}^{-1} \text{ Hz}^{-1/2}$ .

## 5.1 Introduction

**I**N CAVITY-ENHANCED TECHNIQUES, the absorption path length can be increased up to several kilometers [1, 2], hence enhancing the sensitivity significantly. The development of off-axis integrated cavity output spectroscopy (OA-ICOS) [3–7] offered mechanical robustness and relatively simple alignment for field measurements [8], being used in numerous studies during the recent years, such as isotopic studies [9, 10] and breath analysis [4, 11, 12]. The method can straightforward be implemented into practical trace-gas detection schemes, offering great versatility and selectivity, making it less technically demanding and more cost effective than other laser-based methods. A major drawback of OA-ICOS is the significantly reduced cavity transmitted power due to highly reflective mirrors, which impact on the sensitivity of the sensor. It becomes critical, when low power lasers and room-temperature detectors with limited detectivity are the only suitable or available devices for the designed system.

To overcome this drawback, we described in Chapter 4 a improved three mirror OA-ICOS configuration, which recycles the light into a high-finesse cavity [13]. The setup consisted of a pulsed distributed feedback quantum cascade laser (QCL) at room temperature in combination with an OA-ICOS cell for the detection of ethylene. Light emitted from the QCL was coupled into a high finesse cavity and the spectroscopic information was extracted from a measurement of the time integrated light intensity leaking out of the cavity. Here, we present a detailed model on how the optimization process can be performed to achieve optical enhancement. The influence of different re-injection parameters and their effect on the signal-to-noise ratio (SNR) are presented and compared to the experimental results of real-time detection of ethylene. Practical considerations about the use of this simulation tool for other off-axis configurations are also discussed.

## 5.2 Materials and methods

### 5.2.1 OA-ICOS

The OA-ICOS technique has been extensively reviewed in literature [3–8]; here, we briefly highlight the most relevant aspects. It is a laser-based spectroscopic

method developed from cavity ring down spectroscopy. The laser light is injected into a closed optical cavity formed by a pair of high-reflectivity mirrors. The laser beam is tuned over the molecular gas absorption feature of interest. The absorption strength of the gas inside the cavity is extracted from the time-integrated light intensity that leaks out at the rear mirror of the cavity onto the detector. In on-axis configuration, the light is only transmitted at specific wavelengths determined by the free spectral range (FSR) of the cavity. If the laser light is injected off-axis into a cavity, a high number of cavity modes is excited, and the reflection spots on the mirrors either form a circle (spherical mirrors) or a Lissajous pattern (astigmatic mirrors) [14]. This reduces the FSR of the cavity proportional to the number of excited cavity modes. The angle between two adjacent spots on the mirror surface is determined solely by the geometry of the cavity. Based on the properties of the cavity, the re-entrant condition can be fulfilled after only a few passes or reach extremely high values. This will result in a dense spectral mode structure of the optical cavity reducing or even cancelling strong power fluctuations as the on-axis configuration [5]. As such, OA-ICOS takes advantage of long path absorption spectroscopy without active locking to a single longitudinal cavity mode.

An additional mirror with a small entrance hole placed in front of the optical cavity can re-inject the light reflected from the input mirror of the cavity. This is advantageous if the cavity can only slightly be aligned off-axis, thereby reducing the coupling to the cavity resonances and the optical noise only minimally. We demonstrate here that with the use of such a re-injection mirror, the absorption signal and the performance of the system were significantly enhanced depending on various parameters of the re-injection mirror, most importantly the entrance position, the angle and its distance to the cavity. In addition, the optical power transmission of the complete system was improved, thereby counteracting the low detectivity of the detector.

### 5.2.2 Re-injection model

To simulate the effect of the re-injection mirror on the transmission power of the system, we used a ray trace approach through all three mirrors with identical properties, varying the initial position  $(x, y)$ , the incoming angle  $(\alpha_x, \alpha_y)$  and the distance  $d$  between the re-injection mirror and the first cavity mirror. We used a thick lens approach instead of a paraxial approximation used in the model

in Chapter 4 [13] and corrected the matrices (see Eq. 5.2.2) for astigmatism of the mirrors [15]. In addition, the incoming laser beam was modeled by a ring of smaller beams which covered its cross-sectional surface with a waist  $\omega_0$  in the center of the cavity. The corresponding ray trace matrices for these optical elements were:

$$s = \begin{pmatrix} x \\ \alpha_x \\ y \\ \alpha_y \end{pmatrix}; \quad T(d) = \begin{pmatrix} 1 & d & 0 & 0 \\ 0 & 1 & 0 & 0 \\ 0 & 0 & 1 & d \\ 0 & 0 & 0 & 1 \end{pmatrix}; \quad T(r_e) = \begin{pmatrix} 1 & 0 & 0 & 0 \\ \frac{-2}{r_e} & 1 & 0 & 0 \\ 0 & 0 & 1 & 0 \\ 0 & 0 & \frac{-2}{r_e} & 1 \end{pmatrix}$$

$$T(n) = \begin{pmatrix} 1 & 0 & 0 & 0 \\ \frac{(n_1 - n_2)}{n_2 r} & \frac{n_1}{n_2} & 0 & 0 \\ 0 & 0 & 1 & 0 \\ 0 & 0 & \frac{n_1 - n_2}{n_2 r} & \frac{n_1}{n_2} \end{pmatrix} \quad (5.2.1)$$

where  $s$  was the vector containing the position and angle of the beam in  $x$ - and  $y$ -direction,  $T(n)$  represented the refraction of a convex surface with  $r > 0$  with refraction indexes  $n_1$  and  $n_2$ ,  $T(d)$  translated the beam over a distance  $d$  and  $T(r_e)$  reflected the beam off a mirror with radius of curvature  $r$ . The independent contributions of the radius of curvature in both the horizontal and sagittal plane were accounted for via

$$(r_e)_x = \frac{r_e}{\cos \alpha_y}$$

$$(r_e)_y = \frac{r_e}{\cos \alpha_x} \quad (5.2.2)$$

The relations between the different parameters are shown in Fig. 5.1(a), while the steps of the calculations for this model are visualized in Fig. 5.1(b). Starting at the re-injection mirror with coordinates  $(x, \alpha_x, y, \alpha_y)$ , we first translated the beam towards the cavity entrance mirror by

$$s_1 = T(d) \cdot s_0 \quad (5.2.3)$$

The beam then refracted on the front surface of the entrance mirror, propagated through its thickness  $t$  and refracted again, according to

$$s_2 = T(n) \cdot T(t) \cdot T(n) \cdot s_1 \quad (5.2.4)$$

For each beam, which entered the cavity, the ray trace recursively calculated its path through the cavity until it either fulfilled the re-entrant condition (Eq. 3.3.15) or hit the walls of the cavity. A cavity round trip was calculated using

$$s_3 = T(r_2) \cdot T(L) \cdot T(r_3) \cdot T(L) \cdot s_2 \quad (5.2.5)$$

where  $L$  is the cavity length and  $r_2$  and  $r_3$  are the radii of curvature of the first and second cavity mirror, respectively. The number of round trips  $m$  inside of the cavity was calculated according to  $m2\theta = q2\pi$  (Eq. 3.3.15), where  $q$  is an integer,  $m$  the number of round trips inside of the cavity and  $2\theta$  the angle between two adjacent spots on the mirror surface. The subsequent reflections and refractions occurring after the first cavity transmission were calculated by

$$s_4 = T(r_1) \cdot T(d) \cdot T(n) \cdot T(t) \cdot T(-r_2) \cdot T(t) \cdot T(n) \cdot s_1 \quad (5.2.6)$$

with  $r_1$  the radius of curvature of the re-injection mirror. The minus sign in  $T(-r_2)$  occurs due to the fact that the beam reflects off the back side of a concave mirror. To determine how many re-injections occurred between these two mirrors, this calculation ran recursively until the beam either exited through the entrance hole or did not enter the cavity. The corresponding calculation of the enhancement ratio in power as a function of round trips has been introduced in Chapter 4 (Eq. 4.2.3) [13]. Note that only the power enhancement was calculated, as the optical noise may increase due to increased laser noise or etalon effects.

### 5.2.3 Experimental setup

The experimental setup is shown in Fig. 5.1(c) and has been described in detail in Chapter 4 and elsewhere [13]. A pulsed QCL with a center frequency of  $965 \text{ cm}^{-1}$  (Alpes Laser, Switzerland) at room temperature was used for ethylene detection. The laser emitted 30 ns pulses with a repetition rate of 1 MHz with an average power of 10 mW. To scan over the ethylene absorption line, we applied the interpuls tuning method described in Section 2.2 with a bias current ramp of 7 kHz to the laser at sub-threshold level, while maintaining the pulse height. With the help of a focusing lens (ZnSe, diameter 25,4 mm,  $f = 30 \text{ cm}$ ) the laser light was injected into the high finesse cavity formed by two spherical mirrors (ZnSe, diameter 50,8 mm,  $r = 50 \text{ cm}$ ) with a reflectivity of  $R = 99,6\%$  at  $10,3 \text{ }\mu\text{m}$  (II-VI Infrared, Belgium) and a refractive index of  $n = 2,4$ . The cavity consisted of a vacuum-tight aluminum tube of 30 cm length (cell volume 0,6 l, free spectral range of 500 MHz) mounted on two micrometer XY-translation stages for precise

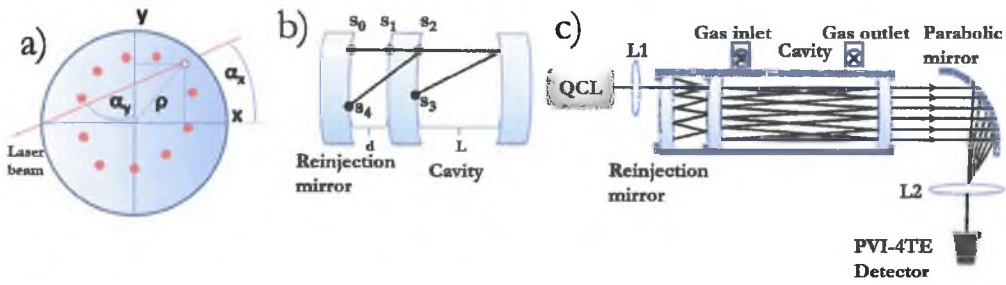


Figure 5.1: Panel (a): Geometric relations for the re-injection model.  $\alpha_y$  and  $\alpha_x$  represent the angles of the laser beam with the y- and x-axis, respectively. Red dots indicate a typical elliptical spot pattern on the mirror. Panel (b): Schematic of the steps during the ray trace calculations. Panel (c): Experimental setup. QCL: quantum cascade laser; L1, L2: focusing and collimating lens, respectively; PVI-4TE detector: four stages thermoelectrically cooled detector.

alignment. The mechanical movement of the translation stages was converted into an angular shift of the cavity, which was measured using a digital spirit level. The third mirror was mounted parallel to the cavity and on its axis. A parabolic mirror behind the cell ( $f = 10$  cm) collected the light and a lens (ZnSe,  $f = 5$  cm) focused it onto the thermoelectrically cooled detector (VIGO PVI-4TE-10.6, Poland, 100 MHz bandwidth,  $D^* = 7,3 \cdot 10^9$  cm Hz<sup>1/2</sup> W<sup>-1</sup>). The signal from the detector was amplified by 40 dB (Femto DLPVA-100-BLN-S, Germany) and low-pass filtered at 100 kHz. All data was sampled on a digital acquisition card (NI PCI-6259, Netherlands) and analyzed with a LabVIEW program.

## 5.3 Results

The model considers only entrance points on the re-injection mirror such that  $x = y$  starting from  $\rho = 0$  to the maximum of  $\rho = 24$  mm with  $\rho^2 = x^2 + y^2$  for constant  $L$ ,  $\omega_0$  and  $r$  for all mirrors. Due to symmetry, only entrance points in the positive quarter of the entrance mirror needed to be considered. A measured beam waist of  $\omega_0 = 0,21$  mm at the center of the cavity was used as input for the model. We simulated the angular distribution of the transmission power as a function of off-axis radius  $\rho$  and the ratio  $d/r$  for an incident laser power of 1 mW.

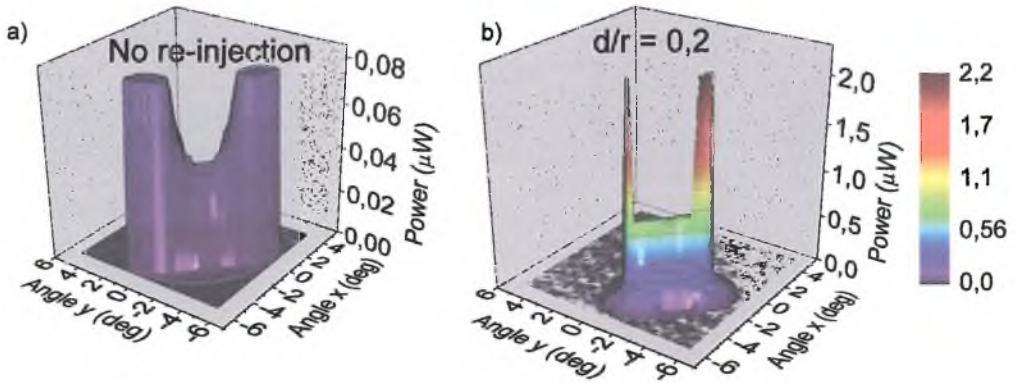


Figure 5.2: Angular distribution of cavity transmission power (shown in color) without re-injection mirror (panel (a)) and with it for  $d/r = 0,2$  (panel (b)) for an off-axis radius of  $\rho = 24$  mm.

For  $\rho = 24$  mm in the case of no re-injection, two symmetrical plateaus for the highest power are formed around  $1^\circ$  in  $x$ - and  $4^\circ$  in  $y$ -direction and vice versa in Fig. 5.2(a), where the color indicates the transmission power. For angles around  $0^\circ$ , the transmission power drops as the light travels close to the cavity's axis inside the cavity with only a few reflections. The transmission with re-injection mirror for  $d/r = 0,2$  was 28 times higher than without, only achieved in a small range around the same angles as in panel (a). The sets of angles for maximum transmission differed for all  $\rho$  and  $d/r$ , where the most insensitive case was a  $\rho = 6$  mm and  $d/r = 0,1$  and the most sensitive for  $\rho = 24$  mm and  $d/r = 1$ .

To verify the enhancement effect of the re-injection mirror, the SNR ratio of the ethylene absorption peak was measured in the absence and presence of the re-injection mirror. The distance  $d$  between the re-injection mirror and the cavity was varied in steps of 5 cm from  $d = 5$  cm ( $d/r = 0,1$ ) to  $d = 50$  cm ( $d/r = 1$ ) with a fixed  $r = 50$  cm. At each  $\rho$ , all three mirrors were optimized according to the simulated data to yield the maximum transmission. The ratio of the measured SNR's in Fig. 5.3(a) (symbols, left axis) decreased with larger  $d/r$  and increased with larger radius. They agree largely with the corresponding calculated transmission powers (dashed lines, right axis). A ratio of 10 in SNR before and after re-injection was achieved for  $d/r = 0,2$  for the largest radius  $\rho = 24$  mm, which corresponds to a simulated power ratio of 28. The decrease in SNR in all curves occurred due to the presence of etalons. In Fig. 5.3(b) simulated data for effect of the reflectivity of the re-injection mirror on the power

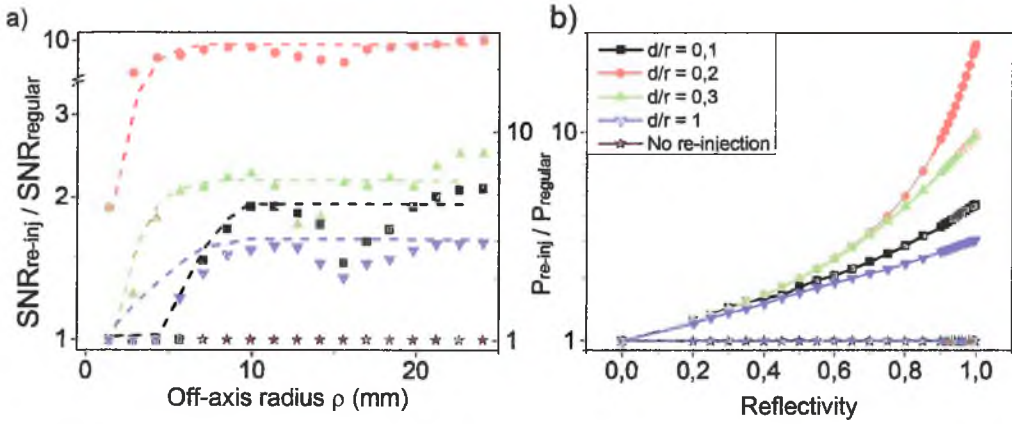


Figure 5.3: Simulated and experimental data. Panel (a): Ratio of measured SNR (symbols, left axis) and calculated transmission power (dashed lines, right axis) versus off-axis radius at optimum angles for various  $d/r$  ratios. Panel (b): Simulated power enhancement versus reflectivity of the re-injection mirror for the same  $d/r$  ratios.

enhancement is shown for different  $d/r$  at a fixed radius of  $\rho = 24$  mm. Until a reflectivity of 30%, the power ratio shows no significant difference. At 70% reflectivity, the power ratio amounts to 4 for both  $d/r = 0,2$  and  $d/r = 0,3$ . The highest ratio of 29 was calculated for  $d/r = 0,2$  and  $r = 99,8\%$ .

In order to demonstrate the improved sensitivity values using re-injection, we measured the spectrum of 200 ppbv ethylene at 100 mbar with and without re-injection with optimal settings. The result is shown in Fig. 5.4(a), showing an increase in SNR of one magnitude. We estimated the stability of the system over time by calculating the Allan deviation [16]. In Fig. 5.4(b) the detection limit of the QCL-based sensor is shown for both the optimum three mirror configuration and to the regular scheme without re-injection. The detection limit for the latter was 1033 ppbv of ethylene for 1 s averaging ( $3\sigma$ -value) and reached the minimum value of 183 ppbv in 128 s. Using the light re-injection technique, a detection limit of 18 ppbv in 32 s was achieved, which translates to a NEAS per point of  $1,5 \cdot 10^{-8} \text{ cm}^{-1} \text{ Hz}^{-1/2}$ . This represents an enhancement by a factor 10, in agreement with the improvement in SNR. The number of re-injections can be further increased using differently shaped mirrors (e.g. astigmatic mirrors), before the optical beam exits the hole in the re-injection mirror.

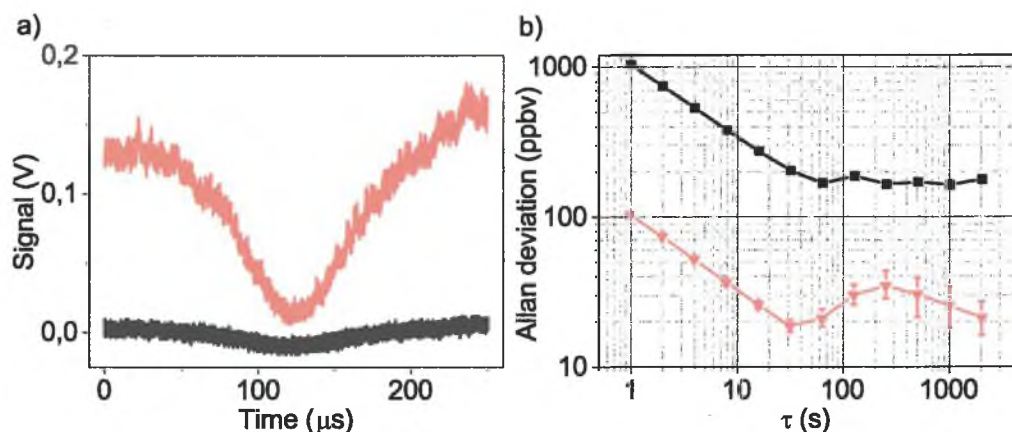


Figure 5.4: (a) Absorption spectra of 200 ppbv ethylene at 100 mbar measured with the re-injection mirror (upper curve, red) and without (lower curve, black). (b) Comparison of Allan deviations to determine the detection limit as a function of the integration time. Regular OA-ICOS reached a minimum detection limit of 183 ppbv within 128 s acquisition time (black squares). With the optical enhancement, a detection limit of 18 ppbv in 32 s was obtained (red triangles).

## 5.4 Discussion

An off-axis system should be optimized before applying the re-injecting technique [17], as the optical enhancement may also increase the optical noise and subsequently reducing the SNR. For example, spurious resonant couplings that produce optical noise increase, when beams overlap in the optical cavity, as shown in Fig. 5.3(a), and the light might be partially lost, when focusing on the detector. The noise-related factors have been excluded from the simulation, as the purpose of this work was to provide a fast and reliable prediction tool for the optimum performance of an enhanced spectrometer. These effects can be minimized by changing other parameters of the setup than the simulated ones. In our case, the scanning rate was increased from 4 kHz as in the previous experiment [13] described in Chapter 4 to 7 kHz.

The re-injection model presented here can predict the sensitivity enhancement of an existing system with one additional mirror compared to standard OA-ICOS and it can readily be applied to any off-axis configuration. Two routes can be

exploited: (1) existing setups can be improved based on their fixed parameters (i.e. laser power, cavity length, mirror reflectivity, etc.) or (2) new systems may be designed for an enhanced scheme depending on the user's requests to gain maximum transmission efficiency. Moreover, using our experimental system as reference, a theoretical prediction of the expected sensitivity and the corresponding optimum conditions can be obtained. Compared to standard OA-ICOS, although the angular dependency was more critical in the enhanced configuration shown in Fig. 5.2, the technique preserved the robustness and rather simple alignment, thus ensuring its practicality for field measurements. Potentially, different setups than the one presented here might provide an even higher enhancement.

## 5.5 Conclusion

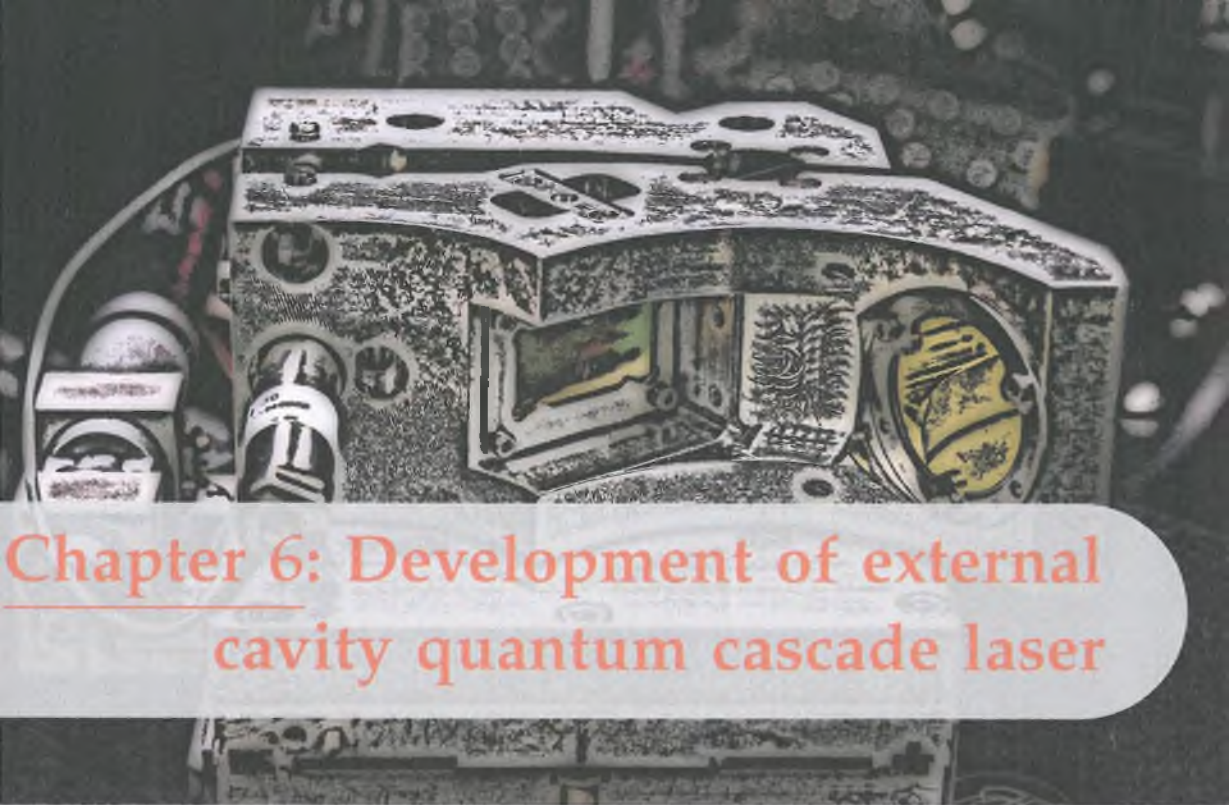
We have demonstrated a versatile simulation tool of an improved three mirror OA-ICOS instrument, which re-injects the light reflected by an optical cavity, and have shown good agreement with experimental results with a QCL at  $965\text{ cm}^{-1}$  for the detection of ethylene. In particular, we optimized the distance between the cavity and the third mirror with respect to the off-axis radius of the cavity and achieved a gain a factor 10 in SNR. Furthermore, our enhanced OA-ICOS system provides real-time measurements of ethylene with a high finesse cavity yielding 18 ppbv in 32 s averaging time, which is equal to a NEAS of  $\sim 1,5 \cdot 10^{-8}\text{ cm}^{-1}\text{ Hz}^{-1/2}$ .

# References

- [1] A. O'Keefe, J. J. Scherer, and J. B. Paul, "Cw integrated cavity output spectroscopy," *Chemical Physics Letters*, vol. 307, no. 5, pp. 343–349, 1999.
- [2] R. Engeln, G. Berden, R. Peeters, and G. Meijer, "Cavity enhanced absorption and cavity enhanced magnetic rotation spectroscopy," *Review of Scientific Instruments*, vol. 69, no. 11, pp. 3763–3769, 1998.
- [3] D. S. Baer, J. B. Paul, M. Gupta, and A. O'Keefe, "Sensitive absorption measurements in the near-infrared region using off-axis integrated cavity output spectroscopy," in *International Symposium on Optical Science and Technology*, pp. 167–176, International Society for Optics and Photonics, 2002.
- [4] Y. A. Bakhrkin, A. A. Kosterev, C. Roller, R. F. Curl, and F. K. Tittel, "Mid-infrared quantum cascade laser based off-axis integrated cavity output spectroscopy for biogenic nitric oxide detection," *Applied Optics*, vol. 43, no. 11, pp. 2257–2266, 2004.
- [5] G. S. Engel, W. S. Drisdell, F. N. Keutsch, E. J. Moyer, and J. G. Anderson, "Ultrasensitive near-infrared integrated cavity output spectroscopy technique for detection of CO at 1.57  $\mu\text{m}$ : New sensitivity limits for absorption measurements in passive optical cavities," *Applied Optics*, vol. 45, no. 36, pp. 9221–9229, 2006.
- [6] D. Herriott, H. Kogelnik, and R. Kompfner, "Off-axis paths in spherical mirror interferometers," *Applied Optics*, vol. 3, no. 4, pp. 523–526, 1964.
- [7] J. B. Paul, L. Lapson, and J. G. Anderson, "Ultrasensitive absorption spectroscopy with a high-finesse optical cavity and off-axis alignment," *Applied Optics*, vol. 40, no. 27, pp. 4904–4910, 2001.
- [8] E. Moyer, D. Sayres, G. Engel, J. S. Clair, F. Keutsch, N. Allen, J. Kroll, and J. Anderson, "Design considerations in high-sensitivity off-axis integrated cavity output spectroscopy," *Applied Physics B*, vol. 92, no. 3, pp. 467–474, 2008.
- [9] Y. A. Bakhrkin, A. Kosterev, R. Curl, F. Tittel, D. Yarekha, L. Hvozdar, M. Giovannini, and J. Faist, "Sub-ppbv nitric oxide concentration measurements using cw thermoelectrically cooled quantum cascade laser-based integrated cavity output spectroscopy," *Applied Physics B*, vol. 82, no. 1, pp. 149–154, 2006.
- [10] P. Sturm and A. Knohl, "Water vapor  $\delta^2\text{H}$  and  $\delta^{18}\text{O}$  measurements using off-axis integrated cavity output spectroscopy," *Atmospheric Measurement Techniques*, vol. 3, no. 1, pp. 67–77, 2010.
- [11] D. Marchenko, J. Mandon, S. Cristescu, P. Merkus, and F. Harren, "Quantum cascade laser-based sensor for detection of exhaled and biogenic nitric oxide," *Applied Physics B*, vol. 111, no. 3, pp. 359–365, 2013.

- [12] M. Silva, D. Sonnenfroh, D. Rosen, M. Allen, and A. O'Keefe, "Integrated cavity output spectroscopy measurements of NO levels in breath with a pulsed room-temperature QCL," *Applied Physics B*, vol. 81, no. 5, pp. 705–710, 2005.
- [13] R. Centeno, J. Mandon, S. Cristescu, and F. Harren, "Three mirror off-axis integrated cavity output spectroscopy for the detection of ethylene using a quantum cascade laser," *Sensors and Actuators B: Chemical*, vol. 203, pp. 311–319, 2014.
- [14] D. S. Sayres, E. Moyer, T. Hanisco, J. S. Clair, F. Keutsch, A. O'Brien, N. Allen, L. Lapson, J. Demusz, M. Rivero, *et al.*, "A new cavity based absorption instrument for detection of water isotopologues in the upper troposphere and lower stratosphere," *Review of Scientific Instruments*, vol. 80, no. 4, p. 044102, 2009.
- [15] E. Hecht, "Optics, 4th," *International edition, Addison-Wesley, San Francisco*, 2002.
- [16] D. W. Allan, "Statistics of atomic frequency standards," *Proceedings of the IEEE*, vol. 54, no. 2, pp. 221–230, 1966.
- [17] C. Dyroff, "Optimum signal-to-noise ratio in off-axis integrated cavity output spectroscopy," *Optics Letters*, vol. 36, no. 7, pp. 1110–1112, 2011.





## Chapter 6: Development of external cavity quantum cascade laser

This chapter is based on:

R. Centeno, D. Marchenko, J. Mandon, S.M. Cristescu, G. Wulterkens, F.J.M. Harren, *High power, widely tunable, mode-hop free, continuous wave external cavity quantum cascade laser for multi-species trace gas detection*, Applied Physics Letters, 105, 261907 (2014),

<http://dx.doi.org/10.1063/1.4905281>

## Abstract

We present a high power, widely tunable, continuous wave external cavity quantum cascade laser (EC-QCL) designed for infrared vibrational spectroscopy of molecules exhibiting broadband and single line absorption features. The laser source exhibits single mode operation with a tunability up to  $303\text{ cm}^{-1}$  ( $\sim 24\%$  of the center wavelength) at  $8\text{ }\mu\text{m}$ , with a maximum optical output power of 200 mW. In combination with off-axis integrated output spectroscopy, trace-gas detection of broadband absorption gases such as acetone was performed and a noise equivalent absorption sensitivity of  $\text{NEAS} = 3,7 \cdot 10^{-8}\text{ cm}^{-1}\text{ Hz}^{-1/2}$  was obtained.

## 6.1 Introduction

**C**ONTINUOUS WAVE QUANTUM CASCADE LASERS (cw-QCLs) have become popular in recent years for a large number of applications such as military and security purposes, medical research, environmental studies, industrial processes, analytical chemistry, and metrology [1–5]. Nowadays, operating at ambient temperatures with high output powers and excellent spectral quality, thermoelectrically cooled cw-QCLs have created a range of MIR gas sensors, offering high sensitivity, selectivity and fast-response time. Moreover, they triggered new applications for gas sensing due to their compact size, narrow line width and high spectral density.

It is known that a large number of compounds in exhaled breath represent products of the metabolism taking place in the human body. Examples of gases in exhaled breath of healthy persons are acetone, ammonia, acetaldehyde, isoprene, ethanol, methanol, and other alcohols [6–9]. Previously, it has been shown that elevated levels of a number of these compounds can be considered as indicators of certain disease conditions. For instance, elevated levels of isoprene or ammonia in breath can indicate renal impairment [10–12], meanwhile acetone is related to diabetes [8, 13, 14] and ethanol to serum glucose levels [15]. In diabetic patients the level of acetone in exhaled breath can increase up to 12 ppmv [16]. Monitoring of exhaled breath acetone can be useful in diabetic patients, since breath analysis is fast, reliable and non-invasive [17].

For spectroscopic applications, single mode operation of the laser source is required. Generally, this is achieved by implementing a distributed feedback (DFB) structure on the laser chip. However, DFB-QCLs are mostly designed for narrow band operation and can be typically current tuned over a spectral range of  $0.1 - 2 \text{ cm}^{-1}$ . The scanning spectral region can be extended up to  $15 - 20 \text{ cm}^{-1}$  by temperature tuning of the laser [18]. This tuning occurs with slow speed, which is disadvantageous for trace gas monitoring. In most cases, the wavelength tuning range at a specific temperature is only sufficient to resolve a single ro-vibrational absorption line of a molecule. Therefore, for each specific wavelength (and for each molecule), a different DFB-QCL has to be designed and manufactured, with relatively low yield for the specific targeted wavelength at room temperature operation. This limits the range of applications and is not cost-effective. In addition, the technical characteristics of the DFB-QCLs make detection of molecules with broadband absorption features impossible.

Within a vibrational band, the spacing between rotational lines of higher mass molecules will become negligible and the lines will start to overlap, such that the vibrational absorption bands will become complex and broad and widely tunable lasers are required for the detection of these gases. For this, external cavity QCLs (EC-QCLs) have been proposed [19–25] and have proven to be suitable for these purposes [19, 26, 27]. A typical EC design consists of a gain chip offering a broadband emission and a reflection grating as spectral selective element to operate the laser in a single mode regime. The wavelength tuning is therefore achieved by rotating the grating. The two most common EC configurations are the Littrow [28–30] and Littman-Metcalf [31, 32] configuration introduced in Chapter 2, both having their own advantages and drawbacks, although the Littrow configuration offers higher power and a simpler design and is mostly preferred [33].

Here, we report on the development and performance of a widely tunable EC-QCL with 200 mW output power. The laser was characterized and applied to high resolution spectroscopy and wide tunability for trace gas detection in the mid infrared wavelength region between 7 and 8.8  $\mu\text{m}$ .

## 6.2 Experimental details

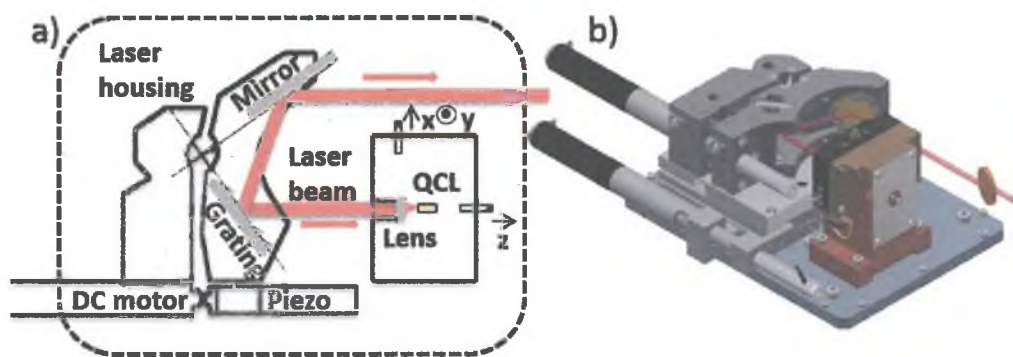


Figure 6.1: A schematic view of the EC-QCL showing the arrangement of the laser components. The laser was mounted vertically on a copper block due to polarization, in front of which a 3D lens positioning system was installed (panel (a)). The full configuration, including the grating, mirror, and step motors, is shown in panel (b).

A schematic view of the external cavity arrangement employing a broadband thermoelectrically cooled QC gain chip, an aspheric lens and a Littrow configuration is shown in Fig. 6.1. The QC gain chip (Alpes Lasers, Switzerland) was anti-reflective (AR) coated for  $8\text{ }\mu\text{m}$  on one facet (reflectivity  $< 0,1\%$  at the center wavelength) and high reflective (HR) coated on the other facet. The collimating aspheric lens was AR coated for  $8 - 12\text{ }\mu\text{m}$  (Lighpath, USA) and the aluminum diffraction grating had over 93% reflectivity (blazed at  $10,6\text{ }\mu\text{m}$ , Optometrics, USA). In this configuration, two QCL chips have been tested, both having gain profiles centered at  $8\text{ }\mu\text{m}$ . To operate at low temperatures, the gain chip was mounted on a copper block, which in turn was placed on top of a Peltier element. The collimating lens was aligned in front of the laser head with a 3-axis manually adjusted stage integrated into the copper block. The collimated laser beam was reflected back from the grating in 1<sup>st</sup> order diffraction, providing optical feedback for lasing, while the 0<sup>th</sup> order diffraction generated an optical output beam. This beam was guided out of the laser housing using a gold mirror placed at  $90^\circ$  with respect to the grating. In this configuration, the angle of the grating and the external cavity length could be tuned independently. The grating and gold mirror were mounted on a home-made rotational stage, which rotated around the intersection point of their respective planes. This arrangement ensured a fixed alignment (angular and spatial) of the output beam during wavelength tuning. The rotation was controlled by a DC motor (M-227.10, Physik Instrumente, Germany) for wide angle tuning and a piezo actuator (P-840.60, Physik Instrumente) for fast scanning over a small wavelength range, allowing a maximum tuning speed of 50 Hz. A translation stage (M-014.DP1, Physik Instrumente) was used to adjust the cavity length using a piezo actuator (P-840.60, Physik Instrumente) and a DC motor (M-227.25, Physik Instrumente). To ensure long-term stability, the overall system was maintained at constant temperature by means of a second stage thermo-electrical cooling system consisting of four Peltier elements. All components were placed into a  $30 \times 20\text{ cm}$  aluminum housing (15 cm high), which was continuously flushed with a low flow of nitrogen to avoid water condensation. The laser beam exited the housing via a ZnSe window placed at Brewster angle.

To achieve mode-hop free tuning, a mode tracking system has been developed as proposed by Wysocki et al. [19]. Here, the laser current and the EC length are modulated with phase-matched triangular voltage ramps during the tuning

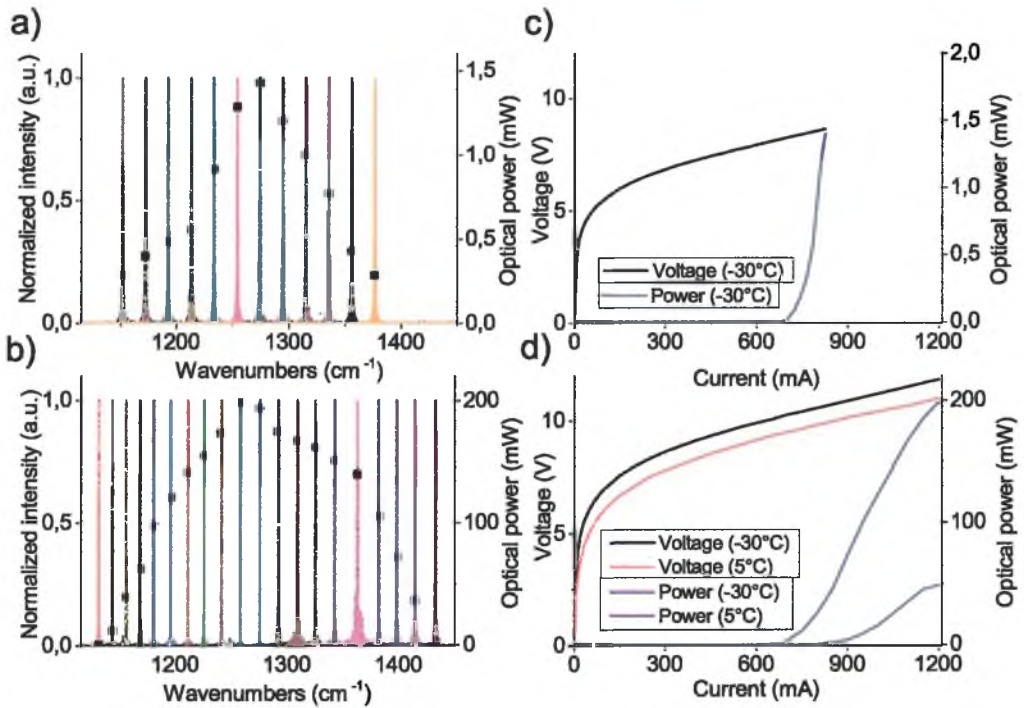


Figure 6.2: Normalized FTIR spectra of the EC-QCL1 (panel (a)) and EC-QCL2 (panel (b)) and the corresponding optical output power (black squares). Panel (c) and (d) show the corresponding voltage-current characteristics and output power for EC-QCL1 and EC-QCL2, respectively.

process. This allows mode-hop-free tuning of  $\sim 1 \text{ cm}^{-1}$  at any wavelength inside the full tuning range of the EC-QCL.

### 6.3 Results and discussion

Prior to spectroscopic measurements, the performance of the EC-QCL in two configurations was determined. Table 6.3 shows the performance of two gain chips in two different configurations and Fig. 6.2 shows the corresponding normalized spectra of EC-QCL1 and 2 (panel 6.2(a) and 6.2(b), respectively) acquired by angle-tuning of the grating, the optical output power (depicted with black squares), and the corresponding voltage-current characteristics (panel (c) and (d), respectively). Both lasers were manufactured from the same wafer in the same run, however, the Sb4425 was 50% longer and 10% wider than the Sb4421.

Single mode performance and wavelength scanning range were measured by a Germanium etalon (free spectral range = 1,5 GHz) and a FTIR spectrometer (Nicolet Magna 560, France, spectral resolution 0,125  $\text{cm}^{-1}$ ). EC-QCL1 reached a maximum tuning range of 230  $\text{cm}^{-1}$  (1150 – 1380  $\text{cm}^{-1}$ ) producing maximum output power of 1,4 mW ( $T = -30^\circ\text{C}$ ). This performance was enhanced in EC-QCL2 mainly by replacing the laser focusing lens and the diffraction grating, resulting in a maximum tuning range of 303  $\text{cm}^{-1}$  (1129 – 1432  $\text{cm}^{-1}$ ) with a maximum output power of 200 mW. EC-QCL1 operated above threshold only at  $T = -30^\circ\text{C}$ , while EC-QCL2 also operated at  $5^\circ\text{C}$  with a maximum power 50 mW.

Table 6.3: Comparison of laser components and performances of both EC-QCLs.

Alpes Laser	EC-QCL1, Sb4421	EC-QCL2, Sb4425
Focusing lens	NA: 0,56; $f = 4$ mm	NA: 0,72; $f = 3$ mm
Grating	Silver coated, 150 lines/mm	Gold coated, 135 lines/mm
Tuning range	230 $\text{cm}^{-1}$ , 1150 – 1380 $\text{cm}^{-1}$	303 $\text{cm}^{-1}$ , 1129 – 1432 $\text{cm}^{-1}$
Max. output power	1,4 mW@ $I_{\text{max}} = 0,82$ A	200 mW@ $I_{\text{max}} = 1,19$ A
Threshold current densities at $T = -30^\circ\text{C}$	$J_{\text{th}}(\text{HR}) = 1,57$ kA/ $\text{cm}^2$ , $J_{\text{th}}(\text{AR/HR}) = 2,6$ kA/ $\text{cm}^2$	$J_{\text{th}}(\text{HR}) = 1,31$ kA/ $\text{cm}^2$ , $J_{\text{th}}(\text{AR/HR}) = 1,7$ kA/ $\text{cm}^2$

Even though both lasers showed similar performances in their uncoated and AR/HR coated state, the output power of EC-QCL1 was significantly lower than of EC-QCL2. This could be attributed to the combination of relative small numerical aperture of the laser focusing lens, its long focal length and the high grating constant, resulting in a low coupling efficiency. In addition, we observed multi-mode behavior of EC-QCL1 at high current, such that the laser consisted of two coupled cavities, namely that of the QC chip itself (FSR  $\sim 15$  GHz) and the external cavity (FSR  $\sim 2$  GHz). Furthermore, the nitrogen flow (needed to operate in a water free environment) inside the housing disturbed

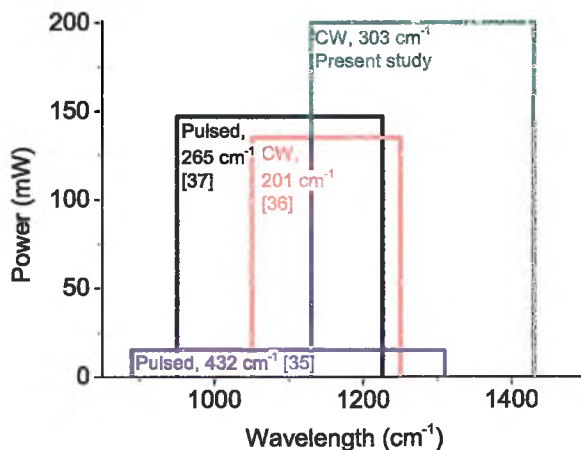


Figure 6.3: Comparison of EC-QCL tuning and output power reported previously using different active region designs.

the laser operation due to a temperature gradient. Replacing the grating and the focusing lens proved a necessity, as we initially built EC-QCL2 with identical components, with no laser action as a result. The main improvement of EC-QCL2 was achieved by choosing a grating with a lower spectral resolution, which enabled immediate lasing with a power output up to 100 mW. The output power was then optimized by replacing the focusing lens with one of a higher numerical aperture.

Previously reported developments on EC-QCLs in the mid infrared wavelength regions are compared with the present study in terms of tuning range and power in Fig. 6.3 [21, 34, 35]. This suggests that the present work combines a wide tuning range with the highest strongest output power in cw lasers up to date.

The wide wavelength tunability of the EC-QCLs along with their suitability for high resolution spectroscopy was demonstrated by performing spectroscopic absorption measurements of acetone, ethanol, dimethyl sulfide and water. Initially, EC-QCL1 was used in combination with a 76 m multipass cell (Aerodyne, USA), whereas later on, due to the high power performance of the second configuration, off-axis integrated cavity output spectroscopy (OA-ICOS) was used [36–38]. For OA-ICOS, the optical cavity had a length of 30 cm with two high reflective mirrors (radius of curvature 1 m, diameter 25 mm, R = 99.97%, CRD Optics, USA), which resulted in an effective path length of 1000 m.

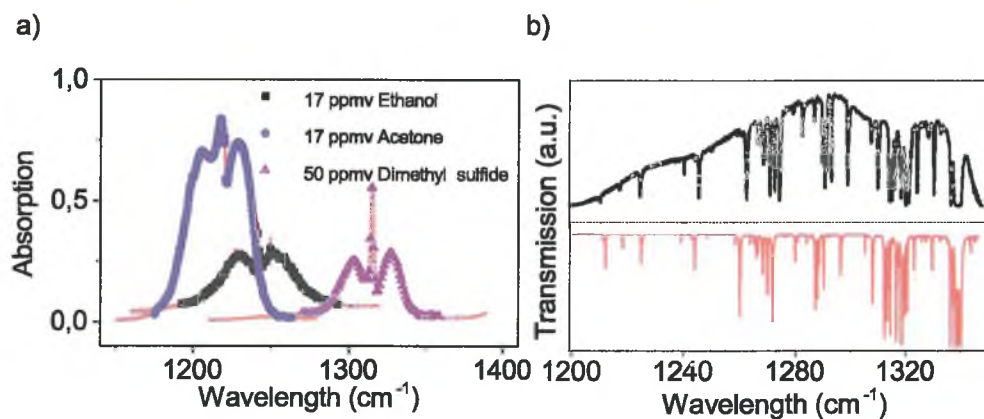


Figure 6.4: Spectra of broadband and narrowband absorption molecules. Panel (a): Spectra of acetone, ethanol and dimethyl sulfide measured at 200 mBar; blue, black and purple: measurement; red and green: PNNL simulation. Panel (b): Spectra of water measured at 1 Bar.

A sinusoidal current modulation of 116 kHz (amplitude of 100 mV) was applied to the laser. The light after the cavity was collected with a lens (ZnSe,  $f = 5$  cm, diameter 25 mm) and directed onto a sensitive infrared detector (VIGO PVI-4TE-10.6, Poland, bandwidth 100 MHz,  $D^* = 1,8 \cdot 10^{10}$  cm Hz<sup>1/2</sup>/W). Spectra were obtained either by coarse tuning of the grating with the DC motor or fine tuning with the piezo. Detector signals were sent to a lock-in amplifier, after which each data point was averaged  $10^4$  times and processed via a data acquisition card (NI PCI-6259, Netherlands) for further computer analysis.

The molecular gas was introduced into the cell with a flow rate of 1 l/h via a mass flow controller (Brooks Instruments, Netherlands). For accurate measurements, the system was calibrated with home-made gas mixtures of  $17 \pm 0,06$  ppmv of acetone in N<sub>2</sub>,  $17 \pm 0,06$  ppmv ethanol in N<sub>2</sub>, and  $50 \pm 0,06$  ppmv dimethyl sulfide in N<sub>2</sub>. Background signals were established by flushing the cell with pure nitrogen gas. Figure 6.4 shows absorption spectra measured in combination with OA-ICOS (panel (a)) and the multipass cell (panel (b)). Panel 6.4(a) shows three measured spectra at 200 mbar pressure of 17 ppmv of acetone measured in 10 seconds with a spectral resolution of  $0,3$  cm<sup>-1</sup>, 17 ppmv ethanol in nitrogen and 50 ppm dimethyl sulfide, both measured with a resolution of 1 cm<sup>-1</sup> in 6 s. The measurements of broadband absorption molecules were neither sensitive to mode-hops nor to narrowband absorption molecules like water and CO<sub>2</sub> due to the moderate pressure in the absorption cell and the low resolution.

In addition, the lasers could perform high resolution spectroscopy, shown by a water absorption spectra at a pressure of 1 bar measured within 2 min with a resolution of  $0,01 \text{ cm}^{-1}$  (panel 6.4(b)).

The noise-equivalent absorption sensitivity (NEAS) per point of EC-QCL2 was calculated by Eq. 3.3.12 following Moyer et al. [36]:

$$\text{NEAS} = \left( \frac{\Delta I}{I_0} \right)_{\min} \frac{1}{L_{\text{eff}}} \sqrt{\frac{nT}{N_p}} \quad (6.3.1)$$

where  $(\Delta I/I_0)_{\min}$  is ratio of the noise on the baseline of the cavity transmission signal and the maximum transmission in the absence of an absorber,  $L_{\text{eff}}$  is the effective optical path length,  $n$  is the number of scans integrated,  $T$  the acquisition time per scan and  $N_p$  the number of data points per spectrum. The  $(\Delta I/I_0)_{\min}$  value was determined from a background measurement and an absorption sensitivity for acetone of  $4,8 \cdot 10^{-9} \text{ cm}^{-1}$  in 60 s was calculated, resulting in a NEAS per point of  $3,7 \cdot 10^{-8} \text{ cm}^{-1} \text{ Hz}^{-1/2}$ .

Scanning was performed up to tens of wavenumber per second, as the coarse tuning of the grating occurred via the step motor. However, during the rotation the aluminum block holding the grating and the mirror showed slight mechanical instability, which resulted in less accurate measurements as power signals shifted. As a consequence, the baseline noise increased and reduced the overall sensitivity for trace gas detection. The sensitivity of the system can be further enhanced using optical re-injection techniques [38, 39] introduced in Chapter 4 and 5 and by minimizing optical feedback into the external cavity. Furthermore, the EC-QCL was not continuously mode-hop free over the full scan range of the laser, but the set of parameters for mode-hop free operation needed to be adjusted for each specific wavelength range. Future work thus concerns mostly the increase of tuning speed without mechanical instabilities and a mode-hop free operation over the full scan range of the laser.

## 6.4 Conclusion

In conclusion, we present a 200 mW high performance EC-QCL for both broadband and narrowband mid-infrared vibrational spectroscopy of molecular gases. The laser source combined a single mode operation with a wide tunability ( $303 \text{ cm}^{-1}$ ), which is the highest tunability and power up to date. In combination with OA-ICOS, trace-gas detection of several gases was demonstrated and a NEAS of  $3,7 \cdot 10^{-8} \text{ cm}^{-1} \text{ Hz}^{-1/2}$  was obtained.

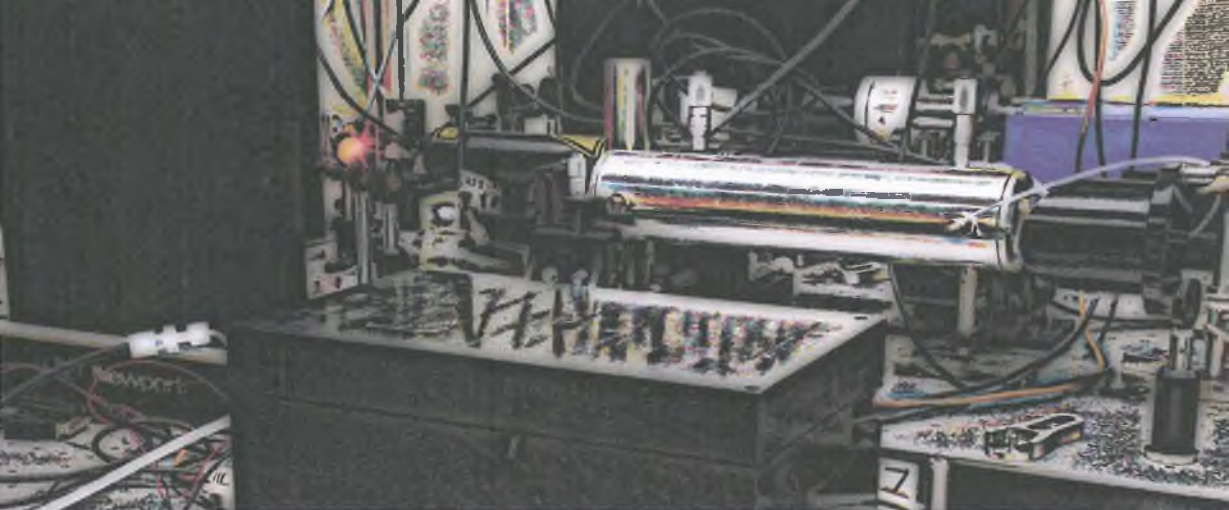
# References

- [1] R. F. Curl, F. Capasso, C. Gmachl, A. A. Kosterev, B. McManus, R. Lewicki, M. Pusharsky, G. Wysocki, and F. K. Tittel, "Quantum cascade lasers in chemical physics," *Chemical Physics Letters*, vol. 487, no. 1, pp. 1–18, 2010.
- [2] J. B. McManus, J. H. Shorter, D. D. Nelson, M. S. Zahniser, D. E. Glenn, and R. M. McGovern, "Pulsed quantum cascade laser instrument with compact design for rapid, high sensitivity measurements of trace gases in air," *Applied Physics B*, vol. 92, no. 3, pp. 387–392, 2008.
- [3] S. Cristescu, S. Persijn, S. te Lintel Hekkert, and F. Harren, "Laser-based systems for trace gas detection in life sciences," *Applied Physics B*, vol. 92, no. 3, pp. 343–349, 2008.
- [4] V. Spagnolo, A. Kosterev, L. Dong, R. Lewicki, and F. Tittel, "NO trace gas sensor based on quartz-enhanced photoacoustic spectroscopy and external cavity quantum cascade laser," *Applied Physics B*, vol. 100, no. 1, pp. 125–130, 2010.
- [5] L. Dong, V. Spagnolo, R. Lewicki, and F. K. Tittel, "Ppb-level detection of nitric oxide using an external cavity quantum cascade laser based QEPAS sensor," *Optics Express*, vol. 19, no. 24, pp. 24037–24045, 2011.
- [6] M. E. Wechsler, H. Grasemann, A. Deykin, E. K. Silverman, C. N. Yandava, E. Israel, M. Wand, and J. M. Drazen, "Exhaled nitric oxide in patients with asthma: association with NOS1 genotype," *American Journal of Respiratory and Critical Care Medicine*, vol. 162, no. 6, pp. 2043–2047, 2000.
- [7] P. Paredi, S. A. Kharitonov, D. Leak, P. L. Shah, D. Cramer, M. E. Hodson, and P. J. Barnes, "Exhaled ethane is elevated in cystic fibrosis and correlates with carbon monoxide levels and airway obstruction," *American Journal of Respiratory and Critical Care Medicine*, vol. 161, no. 4, pp. 1247–1251, 2000.
- [8] M. J. Henderson, B. Karger, and G. Wrenshall, "Acetone in the breath," *Diabetes*, vol. 1, no. HS-039 615, 1952.
- [9] T. King, M. Elia, and J. Hunter, "Abnormal colonic fermentation in irritable bowel syndrome," *The Lancet*, vol. 352, no. 9135, pp. 1187–1189, 1998.
- [10] S. Davies, P. Španel, and D. Smith, "Quantitative analysis of ammonia on the breath of patients in end-stage renal failure," *Kidney International*, vol. 52, pp. 223–228, 1997.
- [11] S. Davies, P. Španel, and D. Smith, "A new 'online' method to measure increased exhaled isoprene in end-stage renal failure," *Nephrology Dialysis Transplantation*, vol. 16, no. 4, pp. 836–839, 2001.
- [12] J. King, H. Koc, K. Unterkofler, P. Mochalski, A. Kupferthaler, G. Teschl, S. Teschl, H. Hinterhuber, and A. Amann, "Physiological modeling of isoprene dynamics in exhaled breath," *Journal of Theoretical Biology*, vol. 267, no. 4, pp. 626–637, 2010.

- [13] B. Buszewski, M. Kęsy, T. Ligor, and A. Amann, "Human exhaled air analytics: biomarkers of diseases," *Biomedical Chromatography*, vol. 21, no. 6, pp. 553–566, 2007.
- [14] M. Storer, J. Dummer, H. Lunt, J. Scotter, F. McCartin, J. Cook, M. Swanney, D. Kendall, F. Logan, and M. Epton, "Measurement of breath acetone concentrations by selected ion flow tube mass spectrometry in type 2 diabetes," *Journal of Breath Research*, vol. 5, no. 4, p. 046011, 2011.
- [15] P. R. Galassetti, B. Novak, D. Nemet, C. Rose-Gottron, D. M. Cooper, S. Meinardi, R. Newcomb, F. Zaldivar, and D. R. Blake, "Breath ethanol and acetone as indicators of serum glucose levels: An initial report," *Diabetes Technology & Therapeutics*, vol. 7, no. 1, pp. 115–123, 2005.
- [16] W. Mueller, J. Schubert, A. Benzing, and K. Geiger, "Method for analysis of exhaled air by microwave energy desorption coupled with gas chromatography–flame ionization detection–mass spectrometry," *Journal of Chromatography B: Biomedical Sciences and Applications*, vol. 716, no. 1, pp. 27–38, 1998.
- [17] D. Samudrala, G. Lammers, J. Mandon, L. Blanchet, T. H. Schreuder, M. T. Hopman, F. J. Harren, L. Tappy, and S. M. Cristescu, "Breath acetone to monitor life style interventions in field conditions: An exploratory study," *Obesity*, vol. 22, no. 4, pp. 980–983, 2014.
- [18] A. Baranov and E. Tournié, *Semiconductor lasers: Fundamentals and Applications*. Elsevier, 2013.
- [19] G. Wysocki, R. F. Curl, F. K. Tittel, R. Maulini, J. M. Bulliard, and J. Faist, "Widely tunable mode-hop free external cavity quantum cascade laser for high resolution spectroscopic applications," *Applied Physics B*, vol. 81, no. 6, pp. 769–777, 2005.
- [20] C. Peng, G. Luo, and H. Q. Le, "Broadband, continuous, and fine-tune properties of external-cavity thermoelectric-stabilized mid-infrared quantum-cascade lasers," *Applied Optics*, vol. 42, no. 24, pp. 4877–4882, 2003.
- [21] R. Maulini, A. Mohan, M. Giovannini, J. Faist, and E. Gini, "External cavity quantum-cascade laser tunable from 8.2 to 10.4  $\mu\text{m}$  using a gain element with a heterogeneous cascade," *Applied Physics Letters*, vol. 88, no. 20, p. 201113, 2006.
- [22] M. J. Weida, D. Arnone, and T. Day, "Tunable QC laser opens up mid-IR sensing applications," *Laser Focus World*, vol. 42, no. 7, p. S13, 2006.
- [23] A. Mohan, A. Wittmann, A. Hugi, S. Blaser, M. Giovannini, and J. Faist, "Room-temperature continuous-wave operation of an external-cavity quantum cascade laser," *Optics Letters*, vol. 32, no. 19, pp. 2792–2794, 2007.
- [24] G. Luo, C. Peng, H. Le, S. Pei, W. Y. Hwang, B. Ishaug, J. Um, J. N. Baillargeon, and C. H. Lin, "Grating-tuned external-cavity quantum-cascade semiconductor lasers," *Applied Physics Letters*, vol. 78, no. 19, pp. 2834–2836, 2001.
- [25] G. Totschnig, F. Winter, V. Pustogov, J. Faist, and A. Müller, "Mid-infrared external-cavity quantum-cascade laser," *Optics Letters*, vol. 27, no. 20, pp. 1788–1790, 2002.

- [26] M. C. Phillips, T. L. Myers, M. D. Wojcik, and B. D. Cannon, "External cavity quantum cascade laser for quartz tuning fork photoacoustic spectroscopy of broad absorption features," *Optics Letters*, vol. 32, no. 9, pp. 1177–1179, 2007.
- [27] R. Lewicki, G. Wysocki, A. A. Kosterev, and F. K. Tittel, "QEPAS based detection of broadband absorbing molecules using a widely tunable, cw quantum cascade laser at 8.4  $\mu\text{m}$ ," *Optics Express*, vol. 15, no. 12, pp. 7357–7366, 2007.
- [28] A. Arnold, J. Wilson, and M. Boshier, "A simple extended-cavity diode laser," *Review of Scientific Instruments*, vol. 69, no. 3, pp. 1236–1239, 1998.
- [29] L. Ricci, M. Weidemüller, T. Esslinger, A. Hemmerich, C. Zimmermann, V. Vuletic, W. König, and T. W. Hänsch, "A compact grating-stabilized diode laser system for atomic physics," *Optics Communications*, vol. 117, no. 5, pp. 541–549, 1995.
- [30] T. Hof, D. Fick, and H. Jansch, "Application of diode lasers as a spectroscopic tool at 670 nm," *Optics Communications*, vol. 124, no. 3, pp. 283–286, 1996.
- [31] K. Harvey and C. Myatt, "External-cavity diode laser using a grazing-incidence diffraction grating," *Optics Letters*, vol. 16, no. 12, pp. 910–912, 1991.
- [32] S. Lecomte, E. Fretel, G. Milet, and P. Thomann, "Self-aligned extended-cavity diode laser stabilized by the Zeeman effect on the cesium  $D_2$  line," *Applied Optics*, vol. 39, no. 9, pp. 1426–1429, 2000.
- [33] C. Hawthorn, K. Weber, and R. Scholten, "Littrow configuration tunable external cavity diode laser with fixed direction output beam," *Review of Scientific Instruments*, vol. 72, no. 12, pp. 4477–4479, 2001.
- [34] A. Hugi, R. Terazzi, Y. Bonetti, A. Wittmann, M. Fischer, M. Beck, J. Faist, and E. Gini, "External cavity quantum cascade laser tunable from 7.6 to 11.4  $\mu\text{m}$ ," *Applied Physics Letters*, vol. 95, no. 6, p. 061103, 2009.
- [35] A. Wittmann, A. Hugi, E. Gini, N. Hoyler, and J. Faist, "Heterogeneous high-performance quantum-cascade laser sources for broad-band tuning," *Quantum Electronics, IEEE Journal of*, vol. 44, no. 11, pp. 1083–1088, 2008.
- [36] E. Moyer, D. Sayres, G. Engel, J. S. Clair, F. Keutsch, N. Allen, J. Kroll, and J. Anderson, "Design considerations in high-sensitivity off-axis integrated cavity output spectroscopy," *Applied Physics B*, vol. 92, no. 3, pp. 467–474, 2008.
- [37] D. Marchenko, J. Mandon, S. Cristescu, P. Merkus, and F. Harren, "Quantum cascade laser-based sensor for detection of exhaled and biogenic nitric oxide," *Applied Physics B*, vol. 111, no. 3, pp. 359–365, 2013.
- [38] R. Centeno, J. Mandon, S. Cristescu, and F. Harren, "Three mirror off axis integrated cavity output spectroscopy for the detection of ethylene using a quantum cascade laser," *Sensors and Actuators B: Chemical*, vol. 203, pp. 311–319, 2014.

- [39] J. B. Leen and A. O'Keefe, "Optical re-injection in cavity-enhanced absorption spectroscopy," *Review of Scientific Instruments*, vol. 85, no. 9, p. 093101, 2014.



## Chapter 7: Influence of ethanol on breath acetone measurements

This chapter is based on:

R. Centeno, J. Mandon, S.M. Cristescu, F.J.M. Harren, *Influence of ethanol on breath acetone measurements using an external cavity quantum cascade laser*, submitted, 2015

## Abstract

Broadly tunable external cavity quantum cascade lasers (EC-QCLs) in combination with cavity enhanced spectroscopy provide high molecular gas sensitivity and selectivity. The latter are essential for the accurate determination of acetone in breath in the mid-infrared wavelength region, which is influenced by interfering gases from breath such as water or carbon dioxide. In particular, ethanol in breath has been shown to have levels up to parts-per-million volume range and affects the accurate determination of acetone in breath. We investigate this influence of ethanol on the acetone concentration in breath utilizing a EC-QCL in combination with off-axis integrated cavity output spectroscopy. We compare the results to previously reported narrowband absorption measurements and increase the accuracy of the measurements by probing the full acetone and ethanol absorption bands between  $1150 - 1300 \text{ cm}^{-1}$ .

## 7.1 Introduction

**T**HE HUMAN BREATH can be quantitatively analyzed for non-invasive disease diagnosis and metabolic status monitoring. The accurate determination of concentration levels of metabolites in breath offers a valuable non-invasive method for the correlation to a variety of pathological conditions [1]. Normal human breath contains common atmospheric gases such as  $\text{H}_2\text{O}$ ,  $\text{CO}_2$ ,  $\text{N}_2$  and  $\text{O}_2$  in relatively high concentrations, and thousands of volatile organic compounds (VOCs), among which acetone and ethanol are most abundant and reach parts-per-billion volume (ppbv) to parts-per-million volume (ppmv) levels [1, 2]. To date, some VOCs have been established as indicators for specific diseases or metabolic disorders. For instance, the presence of isoprene in human breath is related to blood cholesterol levels [3] and patients with Type-1 diabetes have elevated acetone levels in their breath [4]. Such knowledge suggests that breath analysis is useful for human disease diagnosis and/or metabolic status monitoring. However, due to the low concentrations and large quantity of trace compounds in exhaled breath, breath analysis requires a highly sensitive and highly selective sensor in order to identify and determine concentrations of specific biomarkers.

Acetone ( $\text{C}_3\text{H}_6\text{O}$ ) is an endogenous substance and is always abundant in human breath. Elevated breath acetone has been reported in exhaled breath of children on a high-fat diet for the treatment of epilepsy [5]. Acetone concentrations in human breath can also be an indicator of congestive heart failure and cardiac index [6]. Wang et al. demonstrated acetone measurements from human breath using cavity ring-down spectroscopy at 266 nm [7], showing levels between 0,80 and 3,97 ppmv. In another study, Diskin et al. measured the common breath metabolites such as acetone, isoprene and ethanol, among others, in the breath of five healthy subjects over a period of 30 days using selected-ion flow-tube mass spectrometry (SIFT-MS) [8, 9]. Turner et al. performed studies of acetone and endogenous ethanol, i.e. produced within the body and unrelated to ingestion of alcohol, among others, in the breath of 30 healthy volunteers over a six-month period using SIFT-MS. The variation and distribution in concentration was assessed and acetone was found to be a major breath metabolite with levels ranging from 100 ppbv to more than 1 ppmv, while ethanol ranged from 0 to 380 ppbv. Generally, the reported acetone concentrations in breath in literature vary from 0,39 to 0,85 ppmv with an overall mean of  $\sim 0,49 \pm 0,20$  ppmv [10] and for

ethanol from 0,01 to 0,38 ppmv and with a mean of  $\sim 0,13 \pm 0,20$  ppmv [17].

Laser absorption spectroscopy has advanced over the last few decades such that it allows highly sensitive, selective, real-time, and accurate measurements of breath for clinical testing [2, 12]. Many breath metabolites have been detected by laser-based methods with detection sensitivities in the sub-ppbv range. Mid-infrared (MIR) spectroscopy (3 – 25  $\mu\text{m}$ ) provides a powerful method for chemical identification and detection by probing fundamental ro-vibrational molecular transitions, which possess strong and unique absorption pattern. Laser-based spectroscopy can be performed either via narrow frequency scanning or broadband tuning. When performing the former, external cavity lasers are used in the same manner as distributed feedback (DFB) lasers: The laser frequency scans over a single spectral absorption line of the molecule of interest within a limited wavelength range ( $\sim 2 \text{ cm}^{-1}$ ). The use of external cavity lasers (ECL) in such a narrow-scan mode offers some advantages over DFB lasers, because the overall tuning range of the ECL ( $> 150 \text{ cm}^{-1}$ ) is much larger than a single DFB laser ( $\sim 5 \text{ cm}^{-1}$ ) and allows the easy selection of molecular interference free regions. In addition, detection of multi-species absorbers is possible by changing the ECL center wavelength. For sensing applications, external cavity quantum cascade lasers (EC-QCLs) [13–17] provide a light source with high power, broad tuning range, narrow line width, and rapid wavelength tuning for the sensitive and accurate detection of trace gases [18, 19]. One application, for which EC-QCL spectroscopy can provide rapid and sensitive trace-gas sensing, is breath analysis. Examples of using EC-QCLs in narrowband absorption for breath analysis include detection of acetone [20, 21], ammonia [22] and nitric oxide [23].

Broadband tuning allows the detection of larger molecules with dense ro-vibrational transitions as well as complex shape and broader spectral features. In these cases, a measurement of the detailed shape of the absorption spectrum over a wider wavelength range provides the ability to distinguish between different molecules based on comparison to reference library spectra. For spectroscopy of larger molecules, a EC-QCL can be operated in a wide-scan mode to provide a high selectivity for the proper identification of molecules. Combining a QCL with an external cavity offers a substantially enlarged tuning range compared to a DFB-QCL and facilitates the evaluation of broader absorption features, thereby minimizing the effect of line-broadening during the quantitative data evaluation. While the tuning range of a single EC-QCL is much smaller than that of a Fourier-transform infrared (FTIR) spectrometer, it is still sufficient to capture

enough detail in the absorption spectra to allow reliable identification of large molecules in the gas-phase or many condensed-phase materials. Examples of EC-QCLs measuring broadband absorption spectra include the detection of acetone using wavelength modulation spectroscopy with a sensitivity of 100 ppbv [24], Freon 125 with quartz enhanced photoacoustic spectroscopy (QEPAS) [15] and fluorocarbons at low ppbv levels in real-time [17].

In laser spectroscopy, acetone was recently measured in the near-IR [21] and mid-IR wavelength region [15, 20]. In both regions, ethanol and acetone both have strong absorption bands, which interfere with each other. So far, ethanol has been excluded in spectroscopic studies of breath acetone. Figure 7.1 shows a simulated absorption profile of 500 ppbv acetone and 200 ppbv ethanol in the region of  $1150 - 1300 \text{ cm}^{-1}$  for a path length of 1 km at a pressure of 300 mbar. The inset in the top right corner shows the region of  $1216,5 \text{ cm}^{-1}$  and  $1220 \text{ cm}^{-1}$ , for breath acetone analysis as was proposed earlier [20]. This wavelength region was chosen, because of the minimal spectroscopic interference from water and  $\text{CO}_2$ . However, the contribution of ethanol in this region results in an elevated absorption line without any significant lineshape change. The relative error for these chosen concentrations is only 4%; however, we have seen that ethanol and acetone in breath vary greatly depending on the person and the circumstances such that the resulting error may become significant. Consequently, this motivates the aim of the present study to quantitatively determine breath acetone levels taking the contribution from ethanol in breath into account.

The present work combines a continuous-wave (cw) external cavity quantum cascade laser (EC-QCL), described in detail in Chapter 6 and elsewhere [19], operating between 6,9 and 8,9  $\mu\text{m}$  with off-axis integrated cavity output spectroscopy (OA-ICOS) to determine the effect of ethanol on the quantification of acetone levels in breath using the strong absorption band of acetone in the MIR region. This region is well suited for monitoring breath acetone given the relative low spectral influence of other substances in exhaled human breath, such as carbon dioxide, water vapor, methane, and ethanol at endogenous levels [25].

The experimental setup has been described in detail in Chapter 6 and elsewhere [19]. In short, a home-made widely tunable EC-QCL ( $1129 - 1432 \text{ cm}^{-1}$ ) with a maximum power output of 200 mW was combined with off-axis integrated cavity output spectroscopy (OA-ICOS) [23, 26–29]. The optical cavity had a length of 30 cm with two high reflective mirrors (radius of curvature 1

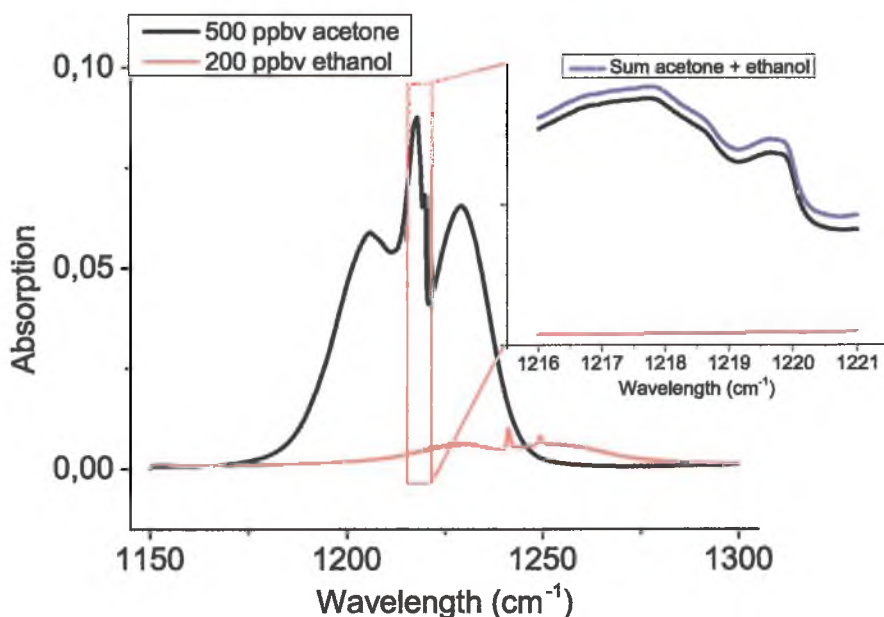


Figure 7.1: Simulation of absorption of 500 ppbv acetone and 200 ppbv ethanol at a pressure of 300 mbar and a path length of 1 km from the PNNL database. The inset shows a zoom of the  $1216\text{ cm}^{-1}$  region, showing the contribution of ethanol in this region, which results in an elevated absorption signal without significant lineshape variation for both contributions (upper curve, blue).

m, diameter 25 mm, reflectivity 99,97%, CRD Optics, USA), which resulted in an effective path length of 1 km. A sinusoidal current modulation of 116 kHz (amplitude of 100 mV) was applied to the laser. The light after the cavity was collected with a lens (ZnSe,  $f = 5\text{ cm}$ , diameter 25 mm) and directed onto a sensitive infrared detector (PVI-4TE-10.6, Vigo, Poland, bandwidth 100 MHz,  $D^* = 1,8 \cdot 10^{10}\text{ cm Hz}^{1/2}/\text{W}$ ). Spectra were obtained by a 50 Hz scan of the grating piezo of the laser covering  $0,3\text{ cm}^{-1}$  for a total integration time of 1 s and rapid coarse tuning of the grating with a DC motor, covering the acetone and ethanol absorption bands between  $1150 - 1300\text{ cm}^{-1}$  in 3 s. Each broadband spectrum was scanned 10 times, where each data point per spectrum was averaged  $10^3$  times. The detector signal for all measurements was sent via a lock-in amplifier ( $\tau = 100\text{ ms}$ ) to a data acquisition card (NI PCI-6259, National Instruments, USA) for processing in LabView for further computer analysis.

Samples of end-tidal breath from healthy subjects were collected and stored

in Tedlar bags [30] for 1 h prior to measurements. Breath samples were guided through a CO<sub>2</sub> scrubber and a cold trap at  $-30^{\circ}\text{C}$  for water removal from the breath. The molecular gas was introduced into the cell (pressure 300 mbar) with a flow rate of 1 l/h via a mass flow controller (Brooks Instruments, Netherlands). For accurate measurements, the system was calibrated with a  $1 \pm 0,06$  ppmv acetone in N<sub>2</sub> (Linde Gas Benelux, Netherlands) and home-made gas mixtures of  $17 \pm 0,06$  acetone in N<sub>2</sub> as well as  $17 \pm 0,06$  and  $1,1 \pm 0,06$  ppmv of ethanol in N<sub>2</sub>. Background signals were established by flushing the cell with pure nitrogen gas. The individual contributions from acetone and ethanol were determined in post-processing by decomposing the measured absorption spectrum and fitting it to the reference measurements containing the full absorption profiles of water, ethanol and acetone. For comparison and validation were the bags also measured with a proton-transfer reaction mass spectrometer (PTR-MS) described elsewhere [31, 32].

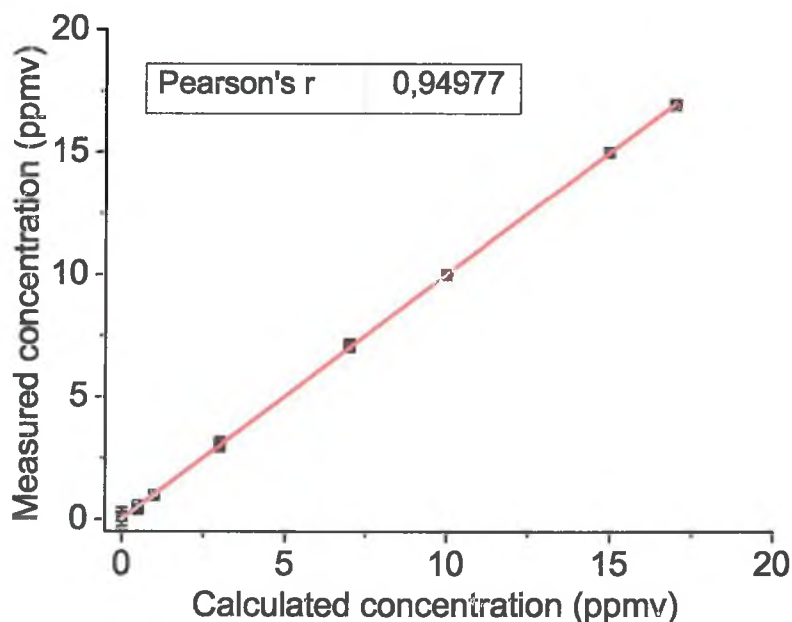


Figure 7.2: Measurements of different acetone concentrations at 200 mbar plotted as a function of calculated acetone concentrations from the mixing ratio with N<sub>2</sub> (10 averaged spectra in 30 s) and a linear fit to them. The  $1\sigma$  values of the averaged concentration values are shown as error bars.

## 7.2 Results and discussion

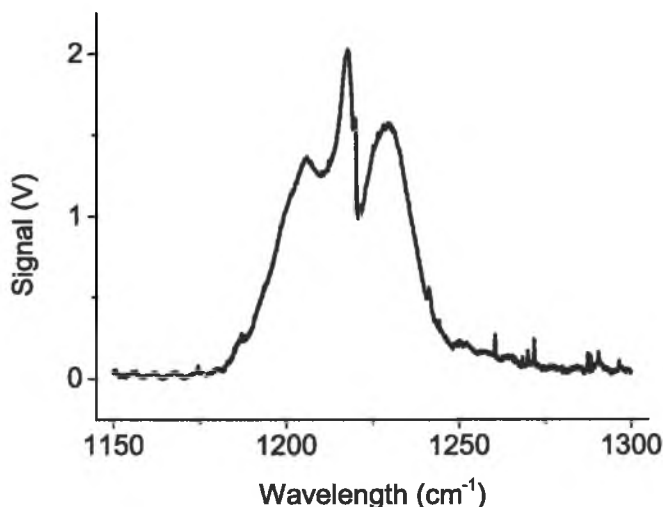


Figure 7.3: Typical measured absorption spectrum of a breath sample consisting of a combined spectrum of acetone, ethanol and water.

Initially, calibration measurements for various concentrations of water, acetone and ethanol in  $N_2$  were performed. The resulting calibration curve for acetone is shown in Fig. 7.2, where the measured concentration is plotted against the calculated one from the mixing ratio with  $N_2$ . The linear fit yields a Pearson coefficient of  $r = 0,95$ . Based on these results, we calculated the noise equivalent absorption sensitivity (NEAS) per point based on the expression given by Eq. 3.3.12, resulting a slightly smaller NEAS value of  $8,4 \cdot 10^{-9} \text{ cm}^{-1} \text{ Hz}^{-1/2}$  as compared to the previously reported one of  $3,7 \cdot 10^{-8} \text{ cm}^{-1} \text{ Hz}^{-1/2}$  [19] in Chapter 6. This translated to a sensitivity of  $\sim 30$  ppbv acetone in 30 s.

A typical absorption spectrum of the breath from a healthy human subject is given in Fig. 7.3. Here, the acetone band is clearly visible; however, the lineshape is distorted and a number of additional peaks appear. The change in lineshape arises from the contribution of ethanol, whereas the small peaks on both ends of the spectrum represent the small fraction of water still present in the sample. To verify the effect of ethanol on breath acetone measurements, we determined the concentration of acetone at  $1216,5 \text{ cm}^{-1}$  using a wavelength range of  $0,3 \text{ cm}^{-1}$ . The bar plot in Fig. 7.4 compares the ethanol corrected breath acetone

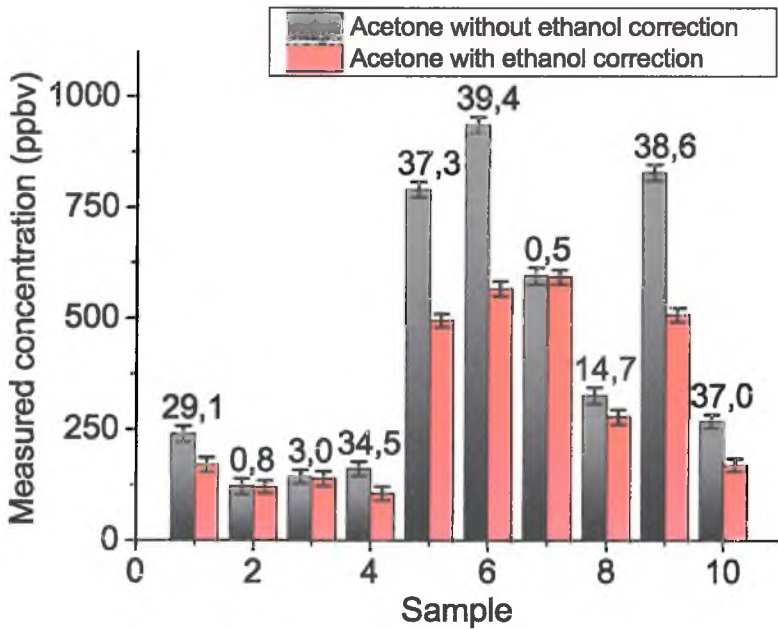


Figure 7.4: Comparison of measured acetone concentration at  $1216,5 \text{ cm}^{-1}$  from 10 breath samples without correction for ethanol (left bars, black) and with (right bars, red). Numbers on top give the relative error of acetone concentrations if the presence of ethanol is not considered.

concentrations with the uncorrected ones, the latter determined directly from a fit to the acetone reference. In each pair of bars, the left (black) bar represents the acetone concentration determined without ethanol correction and the right (red) bar after separating the spectrum and correcting for the ethanol contribution. The error bars were derived from the  $1\sigma$  standard deviation of five consecutive measurements and the numbers on top of the bars represent the relative error in the determined acetone concentration. The error in acetone concentration from all 10 samples ranged from 0% to 39%. This significant contribution to the amount of acetone found in breath can have a profound impact on the determination of the health status of a subject as acetone is an indicator of diabetes and congestive heart failure.

The determination of gas concentrations is more accurate, when the absorption profile over a wide range is measured, as the fit of the broadband spectrum to a database reference spectrum will become more reliable due to the distinction of multiple components in the spectrum. Thus as a next step, we

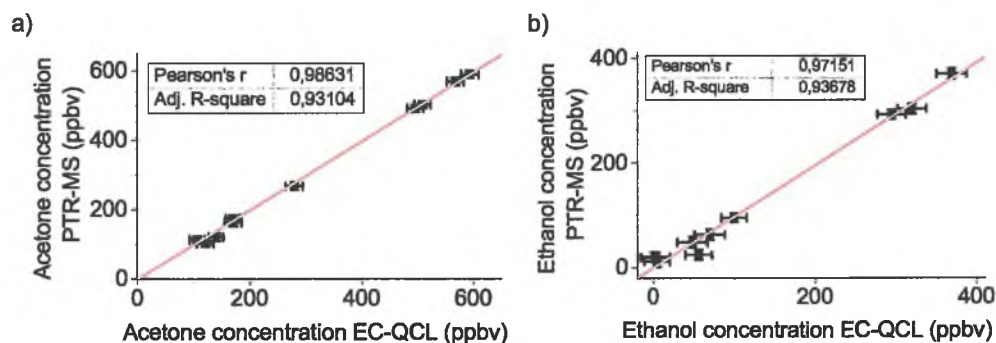


Figure 7.5: Correlation of EC-QCL and PTR-MS data of the measured acetone and ethanol concentrations in human breath. The linear fit provides a Pearson factor of  $r = 0.986$  in the case of acetone and  $r = 0.972$  for ethanol.

performed measurements on the same breath samples using the full absorption spectrum between  $1150 - 1300 \text{ cm}^{-1}$ . The combined absorption spectrum was separated into individual spectra of ethanol and acetone using reference gas mixtures and a PNNL database simulation of water, yielding the individual contributions of each gas. The resulting concentrations of acetone and ethanol were correlated to the measurements taken with the PTR-MS. Acetone levels ranged from 100 ppbv to 600 ppbv, while the detectable amount of ethanol in breath ranged from 0 to 400 ppbv. Figure 7.5 presents two linear fits of this correlation between the EC-QCL and the PTR-MS for both compounds, which yields a Pearson factor of  $r = 0.986$  for acetone and  $r = 0.971$  for ethanol. Despite the good agreement of both data sets, several points lie below the detection limit of the EC-QCL, but could still be measured with the PTR-MS. In contrast, the single outlier most likely comes from the fact that ethanol is prone to fragmentation in the PTR-MS and the measured concentration was thus significantly lower [33].

## 7.3 Conclusions

In this work we demonstrated the strong effect of ethanol in breath on breath acetone measurements ( $\sim 39\%$  error) using a EC-QCL in the region of  $1150 - 1300 \text{ cm}^{-1}$  in combination with off-axis integrated cavity output spectroscopy. In addition, we showed that performing high sensitivity broadband molecular spectroscopy accurately determines the concentrations

of both gases avoiding interference between them. We observed an excellent agreement between measured spectra of ethanol and acetone in comparison to reference measurements from a proton-transfer reaction mass spectrometer. This clearly demonstrates the importance of considering ethanol concentrations for the assessment of acetone in human breath in the spectral region of  $1220\text{ cm}^{-1}$ . In addition, many molecules exhibit broadband features in this region and can be detected with a widely tunable laser to avoid large errors in the precision of their concentrations.

# References

- [1] T. H. Risby, "Volatile organic compounds as markers in normal and diseased states," *Disease markers in exhaled breath: Basic mechanisms and clinical applications*, vol. 284, pp. 113–122, 2002.
- [2] T. H. Risby and F. K. Tittel, "Current status of midinfrared quantum and interband cascade lasers for clinical breath analysis," *Optical Engineering*, vol. 49, no. 11, p. 111123, 2010.
- [3] I. Ueta, A. Mizuguchi, M. Okamoto, H. Sakamaki, M. Hosoe, M. Ishiguro, and Y. Saito, "Determination of breath isoprene and acetone concentration with a needle-type extraction device in gas chromatography-mass spectrometry," *Clinica Chimica Acta*, vol. 430, no. 0, pp. 156 – 159, 2014.
- [4] Z. Wang and C. Wang, "Is breath acetone a biomarker of diabetes? A historical review on breath acetone measurements," *Journal of Breath Research*, vol. 7, no. 3, p. 037109, 2013.
- [5] K. Musa-Veloso, S. S. Likhodii, E. Rarama, S. Benoit, Y. M. C. Liu, D. Chartrand, R. Curtis, L. Carmant, A. Lortie, F. J. Comeau, and S. C. Cunnane, "Breath acetone predicts plasma ketone bodies in children with epilepsy on a ketogenic diet," *Nutrition*, vol. 22, no. 1, pp. 1–8, 2006.
- [6] M. Kupari, J. Lommi, M. Ventilä, and U. Karjalainen, "Breath acetone in congestive heart failure," *The American Journal of Cardiology*, vol. 76, no. 14, pp. 1076–1078, 1995.
- [7] C. Wang and A. B. Surampudi, "An acetone breath analyzer using cavity ringdown spectroscopy: An initial test with human subjects under various situations," *Measurement Science and Technology*, vol. 19, no. 10, p. 105604, 2008.
- [8] A. M. Diskin, P. Španěl, and D. Smith, "Time variation of ammonia, acetone, isoprene and ethanol in breath: A quantitative SIFT-MS study over 30 days," *Physiological Measurement*, vol. 24, no. 1, p. 107, 2003.
- [9] D. Smith, C. Turner, and P. Španěl, "Volatile metabolites in the exhaled breath of healthy volunteers: Their levels and distributions," *Journal of Breath Research*, vol. 1, no. 1, p. 014004, 2007.
- [10] J. C. Anderson, W. J. Lamm, and M. P. Hlastala, "Measuring airway exchange of endogenous acetone using a single-exhalation breathing maneuver," *Journal of Applied Physiology*, vol. 100, no. 3, pp. 880–889, 2006.
- [11] P. R. Galassetti, B. Novak, D. Nemet, C. Rose-Gottron, D. M. Cooper, S. Meinardi, R. Newcomb, F. Zaldivar, and D. R. Blake, "Breath ethanol and acetone as indicators of serum glucose levels: An initial report," *Diabetes Technology & Therapeutics*, vol. 7, no. 1, pp. 115–123, 2005.
- [12] D. D. Arslanov, K. Swinkels, S. M. Cristescu, and F. J. Harren, "Real-time, subsecond, multicomponent breath analysis by optical parametric oscillator based off-axis integrated cavity output spectroscopy," *Optics Express*, vol. 19, no. 24, pp. 24078–24089, 2011.

- [13] R. Maulini, A. Mohan, M. Giovannini, J. Faist, and E. Gini, "External cavity quantum-cascade laser tunable from 8.2 to 10.4  $\mu\text{m}$  using a gain element with a heterogeneous cascade," *Applied Physics Letters*, vol. 88, no. 20, p. 201113, 2006.
- [14] C. Peng, G. Luo, and H. Q. Le, "Broadband, continuous, and fine-tune properties of external-cavity thermoelectric-stabilized mid-infrared quantum-cascade lasers," *Applied Optics*, vol. 42, no. 24, pp. 4877–4882, 2003.
- [15] R. Lewicki, G. Wysocki, A. A. Kosterev, and F. K. Tittel, "QEPAS based detection of broadband absorbing molecules using a widely tunable, cw quantum cascade laser at 8.4  $\mu\text{m}$ ," *Optics Express*, vol. 15, no. 12, pp. 7357–7366, 2007.
- [16] G. Wysocki, R. Lewicki, R. Curl, F. Tittel, L. Diehl, F. Capasso, M. Troccoli, G. Hofler, D. Bour, S. Corzine, R. Maulini, M. Giovannini, and J. Faist, "Widely tunable mode-hop free external cavity quantum cascade lasers for high resolution spectroscopy and chemical sensing," *Applied Physics B*, vol. 92, no. 3, pp. 305–311, 2008.
- [17] M. C. Phillips, M. S. Taubman, B. E. Bernacki, B. D. Cannon, R. D. Stahl, J. T. Schiffern, and T. L. Myers, "Real-time trace gas sensing of fluorocarbons using a swept-wavelength external cavity quantum cascade laser," *Analyst*, vol. 139, no. 9, pp. 2047–2056, 2014.
- [18] R. F. Curl, F. Capasso, C. Gmachl, A. A. Kosterev, B. McManus, R. Lewicki, M. Pusharsky, G. Wysocki, and F. K. Tittel, "Quantum cascade lasers in chemical physics," *Chemical Physics Letters*, vol. 487, no. 1, pp. 1–18, 2010.
- [19] R. Centeno, D. Marchenko, J. Mandon, S. M. Cristescu, G. Wulterkens, and F. J. M. Harren, "High power, widely tunable, mode-hop free, continuous wave external cavity quantum cascade laser for multi-species trace gas detection," *Applied Physics Letters*, vol. 105, no. 26, p. 261907, 2014.
- [20] L. Ciaffoni, G. Hancock, J. J. Harrison, J. P. H. van Helden, C. E. Langley, R. Peverall, G. A. Ritchie, and S. Wood, "Demonstration of a mid-infrared cavity enhanced absorption spectrometer for breath acetone detection," *Analytical Chemistry*, vol. 85, no. 2, pp. 846–850, 2012.
- [21] G. Hancock, C. E. Langley, R. Peverall, G. A. Ritchie, and D. Taylor, "A laser based method and sample handling protocol for measuring breath acetone," *Analytical Chemistry*, 2014.
- [22] G. Wysocki, R. F. Curl, F. K. Tittel, R. Maulini, J. M. Bulliard, and J. Faist, "Widely tunable mode-hop free external cavity quantum cascade laser for high resolution spectroscopic applications," *Applied Physics B*, vol. 81, no. 6, pp. 769–777, 2005.
- [23] D. Marchenko, J. Mandon, S. Cristescu, P. Merkus, and F. Harren, "Quantum cascade laser-based sensor for detection of exhaled and biogenic nitric oxide," *Applied Physics B*, vol. 111, no. 3, pp. 359–365, 2013.
- [24] K. R. Parameswaran, D. I. Rosen, M. G. Allen, A. M. Ganz, and T. H. Risby, "Off-axis integrated cavity output spectroscopy with a mid-infrared interband cascade laser for real-time breath ethane measurements," *Applied Optics*, vol. 48, no. 4, pp. B73–B79, 2009.

- [25] C. Turner, P. Španěl, and D. Smith, "A longitudinal study of ethanol and acetaldehyde in the exhaled breath of healthy volunteers using selected-ion flow-tube mass spectrometry," *Rapid Communications in Mass Spectrometry*, vol. 20, no. 1, pp. 61–68, 2006.
- [26] E. Moyer, D. Sayres, G. Engel, J. S. Clair, F. Keutsch, N. Allen, J. Kroll, and J. Anderson, "Design considerations in high-sensitivity off-axis integrated cavity output spectroscopy," *Applied Physics B*, vol. 92, no. 3, pp. 467–474, 2008.
- [27] J. B. Paul, L. Lapson, and J. G. Anderson, "Ultrasensitive absorption spectroscopy with a high-finesse optical cavity and off-axis alignment," *Applied Optics*, vol. 40, no. 27, pp. 4904–4910, 2001.
- [28] D. S. Baer, J. B. Paul, M. Gupta, and A. O'Keefe, "Sensitive absorption measurements in the near-infrared region using off-axis integrated cavity output spectroscopy," in *International Symposium on Optical Science and Technology*, pp. 167–176, International Society for Optics and Photonics, 2002.
- [29] R. Centeno, J. Mandon, S. Cristescu, and F. Harren, "Three mirror off-axis integrated cavity output spectroscopy for the detection of ethylene using a quantum cascade laser," *Sensors and Actuators B: Chemical*, vol. 203, pp. 311–319, 2014.
- [30] P. Mochalski, J. King, K. Unterkofler, and A. Amann, "Stability of selected volatile breath constituents in Tedlar, Kynar and Flexfilm sampling bags," *Analyst*, vol. 138, no. 5, pp. 1405–1418, 2013.
- [31] E. Crespo, S. Cristescu, H. de Ronde, S. Kuijper, A. Kolk, R. Anthony, and F. Harren, "Proton transfer reaction mass spectrometry detects rapid changes in volatile metabolite emission by mycobacterium smegmatis after the addition of specific antimicrobial agents," *Journal of Microbiological Methods*, vol. 86, no. 1, pp. 8–15, 2011.
- [32] M. Steeghs, H. P. Bais, J. de Gouw, P. Goldan, W. Kuster, M. Northway, R. Fall, and J. M. Vivanco, "Proton-transfer-reaction mass spectrometry as a new tool for real time analysis of root-secreted volatile organic compounds in arabidopsis," *Plant Physiology*, vol. 135, no. 1, pp. 47–58, 2004.
- [33] E. Boamfa, M. Steeghs, S. Cristescu, and F. Harren, "Trace gas detection from fermentation processes in apples; an intercomparison study between proton-transfer-reaction mass spectrometry and laser photoacoustics," *International Journal of Mass Spectrometry*, vol. 239, no. 2, pp. 193–201, 2004.



## Chapter 8: The NICE- OHMS technique

NICE-OHMS is an acronym for noise immune cavity enhanced optical heterodyne molecular spectroscopy. This technique combines cavity enhancement for a long absorption path length with frequency modulation (FM) for the reduction of noise. This method employs a laser, which needs to be locked to a cavity mode of an external cavity via the Pound-Drever-Hall (PDH) method. Furthermore, an additional modulation frequency matches the frequency of the free spectral range of this cavity to suppress the introduction of additional noise. In this chapter, the individual methods are explained, starting with the background theory on FM and the PDH method as well as their subsequent implementation into the NICE-OHMS detection scheme.

## 8.1 Frequency modulation spectroscopy

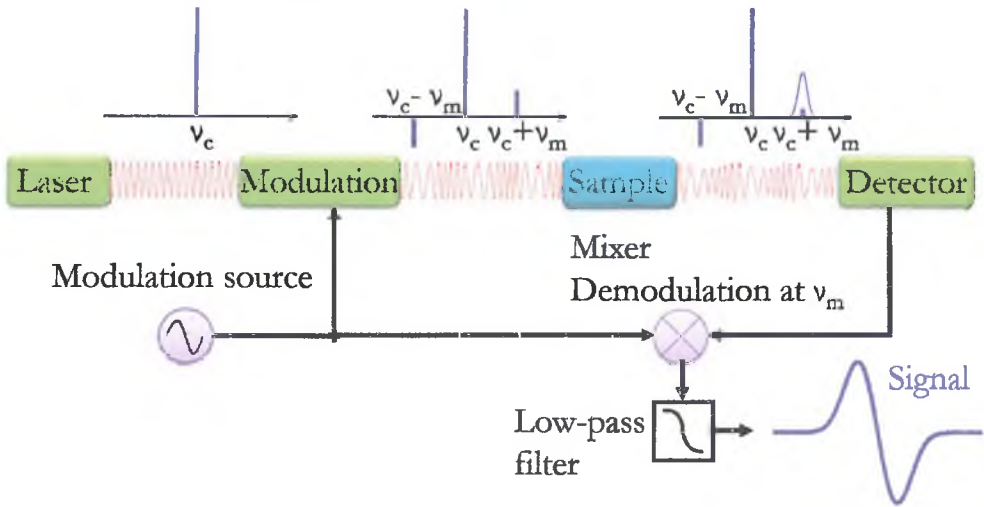
**F**REQUENCY MODULATION SPECTROSCOPY was independently described in the 1980's by Björklund [1, 2] and Hall [3, 4]. The goal of FM spectroscopy is to sensitively detect weak absorption features by actively locking a tunable laser to a high finesse cavity [5]. Both works were closely related to the method developed by Pound for the microwave region in the 1940's [6]. The theory of FM spectroscopy was developed from general control theory. There, a controller compares signals from sensors and drives actuators to reference signals to keep a physical value stable in a desired state. The main benefit of FM modulation is to reduce the effect of  $1/f$ -noise and allows the phase-sensitive detection of spectral features, giving access to both absorption and dispersion information from the analyte. The choice of the FM frequency depends on several factors: 1) The frequency range, where the noise density will be lowest; 2) the width of the molecular line width; and 3) the density of the molecular spectral lines. Thus, the signal-to-noise ratio (SNR) of the system can be significantly improved by encoding the signal at a radio frequency (RF). The modulation of the optical field creates a broadening of the laser spectrum, characterized by the creation of sidebands, equally spaced in frequency by the modulation frequency. Below, the basics of the general optical FM spectroscopy theory is presented [5, 7, 8].

Figure 8.1 depicts a basic setup for phase-sensitive FM spectroscopy. The output of a single-mode laser with carrier frequency  $\nu_c$  gets modulated sinusoidally, either by passing through an electro-optic modulator (EOM) or by current modulation. For this, an electric field with a modulation frequency  $\nu_m$  is applied with a modulation index  $\beta$ . This modulation index  $\beta$  is a measure of how much energy is going into the sidebands, thus it is the ratio of the modulation amplitude  $\delta\nu$ , and the modulation frequency  $\nu_m$ :

$$\beta = \frac{2\pi\delta\nu}{\nu_m} \quad (8.1.1)$$

In FM spectroscopy, the modulation index is mostly chosen such that the light spectrum consists of a strong carrier and only one significant pair of sidebands. The intensity,  $I_1$ , of the sideband relative to that of the carrier,  $I_0$ , for  $\beta \leq 1$  is approximately given by

$$\frac{I_1}{I_0} \approx \left(\frac{\beta}{2}\right)^2 \quad (8.1.2)$$



**Figure 8.1:** Schematic of a basic frequency modulation setup. The laser light with a carrier frequency  $\nu_c$  gets modulated with a frequency  $\nu_m$ . This creates two sidebands in the frequency spectrum, which get attenuated and phase shifted, if passed through an absorber. Demodulating the transmission signal yields the FM signal.

The modulated field can then be described by

$$E(t) = E_0 \exp \left[ i(\nu_c t + \beta \sin \nu_m t) \right], \quad (8.1.3)$$

where  $E_0$  is the electric field amplitude and  $\nu_c$  is the angular optical frequency. We can expand this using Bessel functions of the first kind to give

$$E(t) = E_0 \exp(i\nu_c t) \sum_{n=-\infty}^{\infty} J_n(\beta) \exp(in\nu_m t). \quad (8.1.4)$$

This result indicates that the field consists not only of one frequency, but one carrier  $\nu_c$  with multiple sidebands separated by the modulation frequency  $\nu_m$ .

Next, the effect of the absorption gas on each individual sideband of the optical field has to be formulated as it passes through a cavity of length  $L$ . We represent the absorbing medium by a complex transmission function

$$T(\nu_n) = \exp(-\delta_n - i\phi_n), \quad (8.1.5)$$

the real part representing the absorption over  $L$  and the imaginary part representing the dispersion of the medium. Here,  $\delta_n$  is the amplitude attenuation

$$\delta_n = \frac{\alpha}{2}(\nu_c + n\nu_m)L \quad (8.1.6)$$

with  $\alpha$  the absorption coefficient (see Eq. 3.1.3). The optical phase shift  $\phi_n$  for frequency component  $\nu_n$  can be written as

$$\phi_n = n(\nu_c + n\nu_m)\frac{L}{c} \quad (8.1.7)$$

with  $c$  the speed of light in vacuum [2]. Because each sideband differs in frequency, the magnitude and phase of this transfer function are different for each sideband. The field transmitted through the medium can thus be written

$$E(t) = E_0 \exp(i\nu_c t) \sum_{n=-\infty}^{\infty} T(\nu_n) J_n(\beta) \exp(in\nu_m t) \quad (8.1.8)$$

Still, the field consists of a carrier and a number of sidebands. For  $\beta < 1$ , the higher order terms can be neglected and this sum simplifies to

$$E(t) = E_0 \exp(i\nu_c t) \left[ T(\nu_c) J_0(\beta) + T(\nu_1) J_1(\beta) \exp(i\nu_m t) - T(\nu_1) J_1(\beta) \exp(i\nu_m t) \right] \quad (8.1.9)$$

where the identity  $J_{-n}(\beta) = (-1)^n J_n(\beta)$  has been used. This shows that the spectrum consists of an FM triplet (see Fig. 8.1), namely a carrier and only one pair of sidebands at  $\nu_c \pm \nu_m$ , which are  $180^\circ$  out of phase, but are matched in amplitude. The intensity of the undisturbed FM field does not contain any component at the modulation frequency. This says that if there is no absorption or dispersion feature, the only term that the detector sees is a DC term from a perfect cancellation of the RF signal due to the upper and lower sidebands beating against the carrier. Moreover, this DC term is exactly the same as that of the unmodulated optical intensity, since the normalized value is unity. In other words, without an absorber or some other frequency discriminator, FM yields no signal, which makes it a background free method. With an absorptive feature present, the balance is broken and the effect of attenuation and phase shift experienced differently by each sideband leads to a disturbance of the phase modulated light, resulting in a time varying intensity. The overall power in the optical field is conserved by a corresponding reduction in signal at DC.

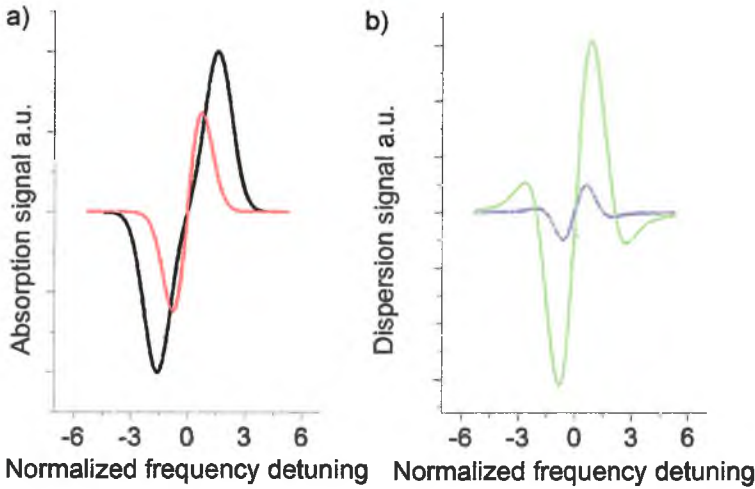


Figure 8.2: Absorption (panel (a)) and dispersion signals (panel (b)) for a Doppler width of 470 MHz and a modulation frequency of 230 MHz for two modulation indexes  $\beta = 0.4$  and  $\beta = 1.6$ . Both absorption and dispersion signals broaden and enlarge with greater modulation index.

FM spectroscopy mostly employs modulation frequencies comparable to or greater than the absorption linewidth (often hundreds of MHz till GHz range). If it is greater than the absorption linewidth, each spectral feature can be probed by an isolated sideband during a frequency scan of the carrier. Phase sensitive detection occurs after demodulation with a mixer and a phase shifter to isolate both absorption ( $\sim \cos \nu_m t$ ) and dispersion ( $\sim \sin \nu_m t$ ). Choosing the detector signal as one input and the modulation signal of the local oscillator at  $\nu_m$  as a reference, the demodulation process will contain a signal at the sum and difference frequencies of the input signals. The difference frequency signal, which will be at DC, can be further filtered out with a low pass filter. The amplitude attenuation  $\delta_n$  and the phase shift  $\phi_n$  can be expressed in terms of the absorption and dispersion lineshape function  $f^{\text{abs}}$  and  $f^{\text{disp}}$  [9]. The expression for the FM spectroscopy signal after demodulation is given by [1, 2, 7, 9]

$$S^{\text{FM}} = S_0 \left\{ \left[ f^{\text{abs}}(\nu_c - \nu_m) - f^{\text{abs}}(\nu_c + \nu_m) \right] \sin(\theta_{\text{FM}}) + \left[ f^{\text{disp}}(\nu_c - \nu_m) - 2f^{\text{disp}}(\nu_c) + f^{\text{disp}}(\nu_c + \nu_m) \right] \cos(\theta_{\text{FM}}) \right\} \quad (8.1.10)$$

where  $S_0$  is the FM signal strength containing information about the absorption sensitivity and detector responsivity,  $\theta_{\text{FM}}$  represents the detection phase and  $f^{\text{disp}}$  and  $f^{\text{abs}}$  are peak normalized dispersion and absorption lineshape profiles of an absorber, respectively.

The influence of the modulation index on the shape of FM signals is shown in Fig. 8.2, where the absorption and dispersion FM lineshapes for  $\beta = 0.4$  and  $\beta = 1.6$  for a Doppler width of 470 MHz and a modulation frequency of 230 MHz are plotted. Both the absorption and dispersion lineshapes become broader and larger as the modulation index increases. To achieve the largest lineshapes, both the detection phase and the modulation frequency have to be optimized.

## 8.2 Laser frequency stabilization with an optical cavity

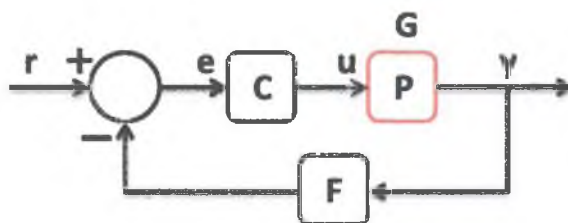


**Figure 8.3:** Block diagram of a negative feedback control loop. The output of the system  $y$  is sent through a sensor  $F$  to the reference  $r$ . The controller  $C$  adjusts the input  $u$  of the controlled system  $P$  with gain  $G$  according to the difference  $e$  between the reference and the output.

In general, feedback loops are useful for stabilizing certain parameters based on the inputs of their environment, such as a thermostat. In Fig. 8.3, such a system is depicted. Here,  $F$  measures the output of the system  $y(\nu)$  and feeds it to the reference value  $r(\nu)$ . The controller  $C$  then takes the error  $e(\nu)$  between the reference and the output to change the inputs  $u(\nu)$  of the controlled system  $P$  with a certain gain  $G(\nu)$ .

The basic goal of locking the frequency of a laser to a cavity is to reduce the frequency fluctuations between the laser and cavity to avoid intensity noise in the transmitted signal due to coupling of frequencies. The noise spectrum of the laser's frequency fluctuations leads to an effective line width of the laser, which conceptually describes the broadening of the laser's spectrum around its central frequency. In order to reduce the laser line width, one needs a stable frequency

reference suitable for measuring the laser's frequency fluctuations, which will be an optical cavity in our case. A general locking scheme involving negative feedback is presented in Fig. 8.3. The first step in the locking procedure is to generate an electronic error signal from a reference (the optical cavity in this case) that can be further processed for locking. Electronic feedback is used to control the laser frequency and minimize its deviations relative to the cavity mode. There are various methods for locking a frequency stabilize a laser to an optical cavity using current modulation such as mode locking to the side of a cavity mode, the Pound-Drever-Hall method and phase detection to reduce the line width of the laser [10].

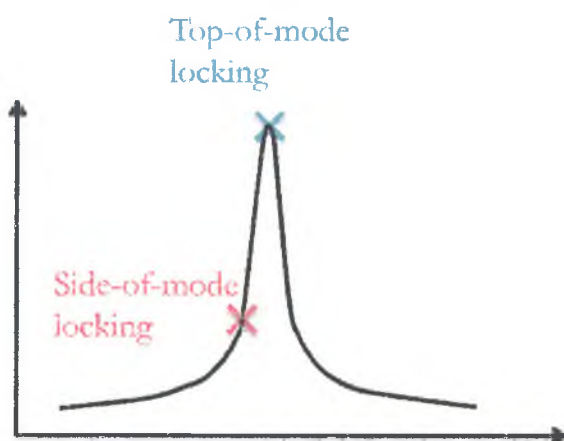


**Figure 8.4:** Schematic of side-of-mode and top-of-mode lock. A cavity mode translates frequency variations into intensity changes. These can be used to lock the laser to either the side of the cavity mode (red cross) or to the top of the mode (blue cross).

With side-locking (shown in Fig. 8.4), the laser is stabilized to the side of the cavity mode without any modulation, where the change in intensity indicates the direction of frequency adjustment. While this technique is straightforward to implement and the modulation-free approach is advantageous, it has a number of drawbacks. The error signal gets detected at DC, thus it is significantly influenced by amplitude noise and as a result less robust. In addition, the signal-to-noise ratio is not optimal, because one locks to the side of the resonance rather than the top, which results in a reduced buildup of optical power inside the cavity.

## Info

In the context of the effective path length calculated in Chapter 3, we consider now the case in CEAS with a laser frequency locked to resonance, but not tightly enough to reduce its linewidth below that of the resonance. The average intensity transmitted will then be sensitive to the distribution of the laser spectrum across the resonance profile, which changes both in width and peak transmission as a function of cavity loss. This case will thus produce an intermediate  $\beta$  value (from the cavity enhancement factor  $\beta\mathcal{F}/\pi$ ) that will vary when adjusting the locking loop. In addition, the absorption law in this case will also be intermediate between that for the resonant and non-resonant CEAS, and will depend on the laser lineshape.

The Pound-Drever-Hall (PDH) method employs frequency modulation as described in the previous section and combines it with cavity enhancement. The sample shown in Fig. 8.1 is now replaced with an optical cavity, while the rest of the setup remains. With the PDH method, the resulting demodulated error signal is more stable than with side locking, since it has a higher signal-to-noise ratio and a larger detection bandwidth. Furthermore, this error signal has odd symmetry about the line center that enables fast locking to the top of a cavity mode. In addition, it allows for the reduction of the laser line width due to high modulation frequency (MHz range).

An error signal is created by sending a modulated laser light at frequency  $\nu_{\text{PDH}}$  through the cavity and by detecting its reflection signal. Because the light consists of a carrier with two sidebands, one in phase relative to the carrier and one out of phase by  $180^\circ$ , the beating of one sideband with the carrier is canceled by the beating of the other one with the carrier in the absence of an absorber. As mentioned before, once this balance gets perturbed (in this case a cavity mode), the phase and amplitude will get attenuated and the detector signal will contain a component at the modulation frequency.

Frequency modulation is used to extract the laser frequency fluctuations around the modulation frequency by demodulating the error signal down to DC. This demodulation process is accomplished by electronically combining the error signal from the detector with a phase-shifted reference signal from the voltage controlled oscillator in a double balanced mixer (see Fig. 8.1). When this signal is demodulated, the result is a frequency discriminator with odd

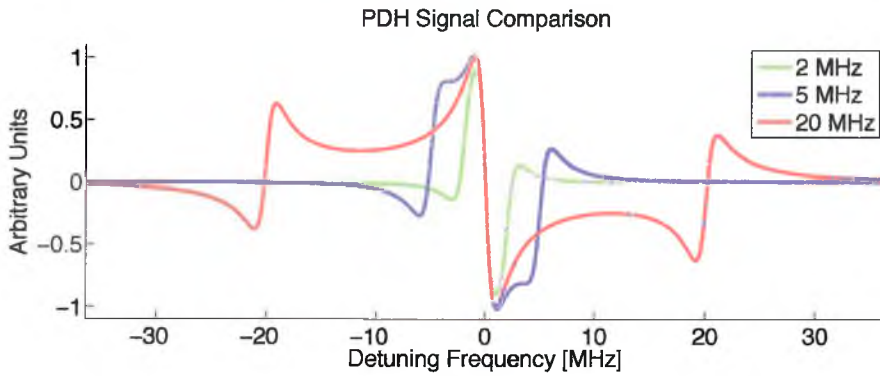


Figure 8.5: Pound-Drever-Hall error signals for modulation frequencies of 2 MHz (green), 5 MHz (blue) and 20 MHz (red) for a cavity line width of 5 MHz and a modulation index of  $\beta = 0.53$ . The largest and steepest error signal is achieved with a modulation frequency in the range of the cavity line width.

symmetry that may be used to correct the frequency of the laser. A simulation of a normalized PDH error signal for modulation frequencies of 2, 5 and 20 MHz for a cavity line width of 5 MHz is shown in Figure 8.5. The largest and steepest error signal is achieved with a modulation frequency in the range of the cavity line width. This error signal is the strongest of all, but has a limited bandwidth. Larger modulation frequencies increase the locking bandwidth as the sidebands move away from the carrier bandwidths.

Note that the error signal observed, when current modulation is employed, contains a large DC component. This is attributable to the strong intensity modulation (RAM) that must be compensated for. The optimum locking will be obtained for the highest possible signal-to-noise ratio (SNR) of the error signal. The error signal's discriminator will have a linear slope measured in units of volts per laser frequency, i.e. V/MHz. The factors that determine this slope include the cavity's line width, the sideband amplitude, the power on the detector, the detector gain (V/A), the postdetector amplification and the mixing process. The noise on this discriminator should be attributable to the laser frequency noise and ultimately at a much lower level by shot noise and detector noise. Locking of the laser frequency to the center of a cavity mode occurs then through an electronic feedback loop (or 'servo' loop) by negative feedback. There are two basic determining factors in the final performance of the lock: the initial noise spectrum of the laser and the electronic bandwidth achievable in the feedback system.

Either the laser or the cavity can be locked to the error signal. In many cavity locking setups, the error signal is used to correct the laser's frequency, matching it to the cavity resonance [11–14]. The best performance can be achieved, if the system is shot noise limited, however, this depends on whether the laser intensity fluctuations at the modulation frequency are at the shot noise limit. Often this is not the case and other techniques have to be implemented to reduce any residing noise.

### 8.3 Electronic feedback

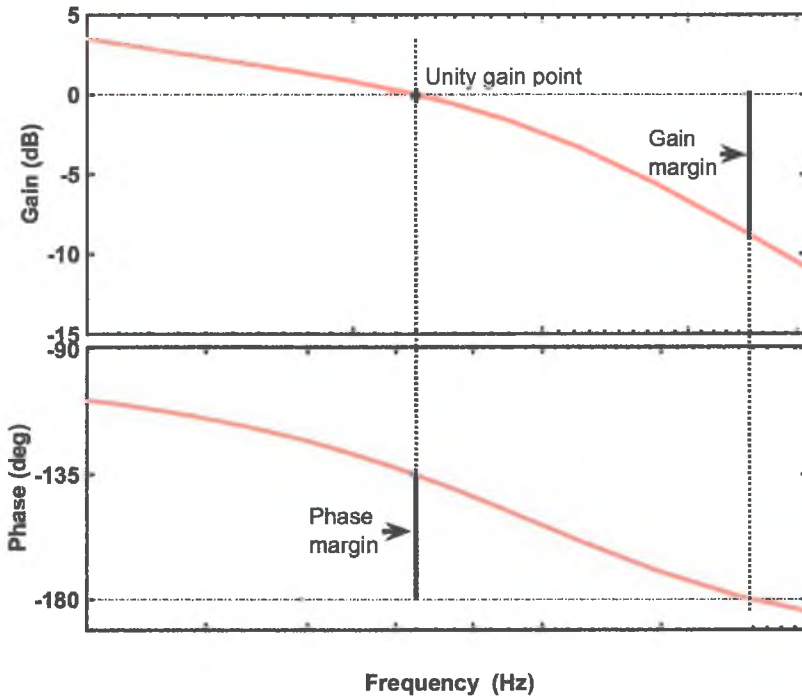


Figure 8.6: Bode plot of an open-loop system. The unity gain point, the phase and the gain margin are indicated by dotted lines.

The goal of the feedback electronics is to supply enough gain to reduce the frequency fluctuations of the laser, preferably over the full servo bandwidth. A feedback loop, plotted in Fig. 8.3, is created from a signal path that goes from the

laser to the cavity, via a detector to an electronics gain stage and back to the laser. The system has an overall gain  $G(\nu)$  at the frequency  $\nu$ . Periodical perturbations introduced in this system will be reduced by a factor of  $[1 + G(\nu)]^{-1}$  in gain. The phase of the system will shift depending on the frequency, such that the resultant phase shift increases until it is  $180^\circ$  out of phase [10]. The latter gives positive feedback and causes an oscillation. The bandwidth of the servo loop refers to the frequency at which the gain falls to zero dB, also called the unity-gain point. A few rules-of-thumb should be considered for an appropriate design:

1. The bandwidth of the loop should be maximized.
2. At the unity-gain point (dotted line at zero dB in Fig. 8.6), the slope of the loop transfer function should have a slope of 20 dB per decade of frequency to ensure enough gain margin.
3. The open-loop gain should be maximized to ensure stability at low frequencies.
4. The cavity acts as a low pass filter, which will affect the phase and has to be compensated for with a phase-lead controller.

The gain margin is defined as the change in open-loop gain required to make the system unstable. Systems with greater gain margins can withstand greater changes in system parameters, before becoming unstable in the closed-loop situation. The phase margin, in turn, is defined as the change in open-loop phase shift required to make a closed-loop system unstable. To avoid this, the loop gain has to be less than zero dB close to a phase shift of  $180^\circ$ . The servo should be designed such that there is sufficient gain  $G(\nu)$  at low frequencies, while maintaining the unity-gain frequency to keep the loop stable. Bode plots are a convenient way to illustrate the gain and phase of a system. They plot the dependency of both gain and phase of the frequency in a log-log plot, which allows a simple check of the above mentioned points. An example of such a plot is shown in Fig. 8.6.

In order to determine the phase and amplitude transfer function of the laser, the amplitude and relative phase of the reflected (or transmitted) laser intensity modulation can be measured. This occurs by comparing the phase difference between the reflected beam and the reference for a given frequency. The amplitude of the modulation has to be set such that a given difference in frequency (i.e. carrier-sideband or carrier-carrier difference) is always equal

for a given frequency, for instance by taking the edges of an oscilloscope as reference points. This will result in a Hz/V and a Hz/degree measurement in order to produce two corresponding Bode plots, one for the phase and one for the amplitude. Any RAM on the laser field may cause a phase shift, leading to inaccuracies, when designing the servo. It is therefore of great prominence to remove any RAM from the system, which will be discussed in the next section.

## 8.4 Residual amplitude modulation

Residual amplitude modulation (RAM) was introduced in Section 3.1.1 as the amount of FM converted into AM during the modulation of an optical field. The importance of RAM arises from the fact that it re-couples  $1/f$ -noise back into measurements, even though the use of FM is to prevent exactly this from happening. This is because RAM produces signals unrelated to the absorption signals on the detector, hence produces false signals, mostly resulting in a signal offset. When used in a locking servo system, this offset causes the laser to be locked to the side of the cavity resonance rather than the peak. As this effect causes periodically varying offsets in the error signal, the locking point of the cavity undergoes periodic variations as well. There are different reasons, why these offsets vary, i.e. optical fringing or impure modulation frequency. This results in periodic noise in the measurements.

RAM can be dealt with in different ways. First is to optimize the PDH modulation frequency and the detection phase to lower the relative contribution of RAM. This possibility depends strongly on the properties of the laser in response to a modulation. Another method is to reduce the optical fringing by placing most optical components at so-called etalon-immune distances [15]. Here, if the FSR of an etalon matches the modulation frequency, the modes of the FM spectrum are equally affected by the etalon and do not give rise to any residuals. Additionally, RAM can be removed electronically. Hobbs patented a noise canceler, which electronically combines three signals: 1) an undisturbed portion of the beam, 2) the cavity reflected beam and 3) the cavity transmission. By combining both the transmission and the reflection signal and comparing it to the undisturbed signal, tuning-insensitive measurements of the intensity are possible and therefore highly efficient extinction of RAM down to the shot-noise level [16]. Furthermore, it allows the tight locking of a laser to a reference cavity [17]. Recently, Zhang et al. showed that an active servo loop involving both DC electric field and temperature corrections applied to an EOM can

remove RAM close to the cavity thermal noise limit [18]. Alternatively, RAM can be optically removed [19] by splitting the modulated laser output power into two paths, one directed through a gas cell and the other through a fiber delay line, and by recombining them before the detector. The sinusoidal modulation frequency and delay arrive with a phase separation of  $\pi$  at the re-combiner. The amplitudes of the anti-phase intensity modulated signals are balanced using a variable optical attenuator in the delay line arm. In the absence of an absorber, these signals cancel at the combiner output. The resulting DC signal is rejected by a lock-in amplifier, making the output zero and thus eliminating the RAM signal. In the presence of gas the imbalance at the output directly reflects the concentration dependent absorption of the gas.

## 8.5 NICE-OHMS

NICE-OHMS stands for Noise-Immune Cavity-Enhanced Optical Heterodyne Molecular Spectroscopy [9, 11–15]. This technique is based on FM spectroscopy and the Pound-Drever-Hall method for laser frequency stabilization and is depicted in Fig. 8.7. Additionally, a modulation frequency, set to be equal to the cavity free spectral range (FSR), is employed in the setup, equalizing the interval between adjacent modulation sidebands and adjacent cavity modes [20]. When locked to the cavity, both the carrier and sidebands of the laser field pass into the cavity, thus allowing phase-sensitive detection to be carried out, while benefiting from the sensitivity enhancement of the optical cavity. Commonly, the FSR lies in the MHz to GHz range for cavities in the order of tens of cm. Due to this high frequency is the optimum modulation index  $\beta$  small. Therefore, only one spectral component of the modulated field interacts with an absorption feature at any one time during a scan. By using an optical cavity, the absorption path length is greatly enhanced, which contributes positively to the sensitivity of the technique. During a scan over an absorption line, the cavity mode shifts in frequency and the resulting detuning with the optical carrier (or sideband) produces a detectable intensity signal. The 'noise-immune' part of the name refers to relative frequency noise between the laser and the optical cavity. A change in this relative frequency will change the amplitude and phase of the sidebands both passing through and reflected from the cavity. However, in NICE-OHMS the carrier and sidebands are all passed into the cavity via identical adjacent cavity modes. Any fluctuations due to relative frequency noise between the laser and the cavity will thus be common to all sidebands,

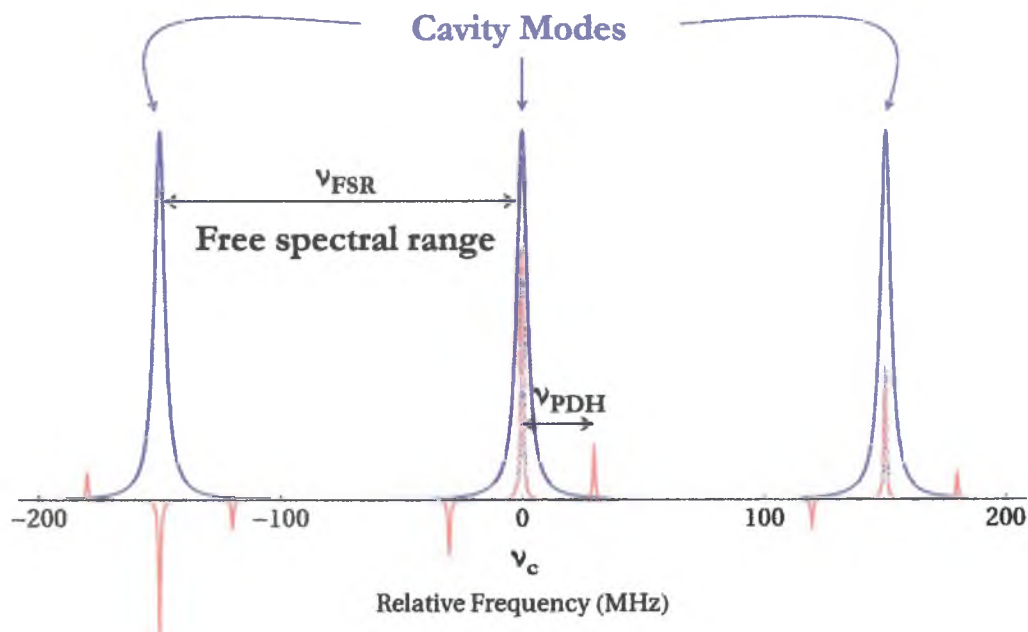


**Figure 8.7:** Schematic of the NICE-OHMS method. The laser is modulated at two frequencies  $\nu_{\text{PDH}}$  for laser frequency stabilization and  $\nu_{\text{FSR}}$  for noise immunity. The frequency for locking is smaller than the cavity FSR but larger than the cavity mode width, while  $\nu_{\text{FSR}}$  matches the cavity FSR. The transmission signal is demodulated at  $\nu_{\text{FSR}}$  to yield the NICE-OHMS signal.

and not produce a signal as can be seen directly from Eq. 8.1.10. However, changes to the phase or amplitude of one sideband such as the dispersion of an absorption feature of the analyte as discussed above, will produce a signal. The modulation frequency can be matched to the FSR by demodulating at the sum or difference of the two modulation frequencies. The term 'optical heterodyne' refers to the fact that we use beat notes from the two sidebands with the carrier, which are demodulated with a reference signal and fed back to the laser and the FSR modulation source for frequency correction.

A basic NICE-OHMS setup is depicted in Fig. 8.8. The two locking path ways are indicated in color, where blue stands for laser frequency stabilization and green for noise immunity, both occurring via the reflection signal. The molecular absorption or dispersion signal gets detected in transmission, indicated by

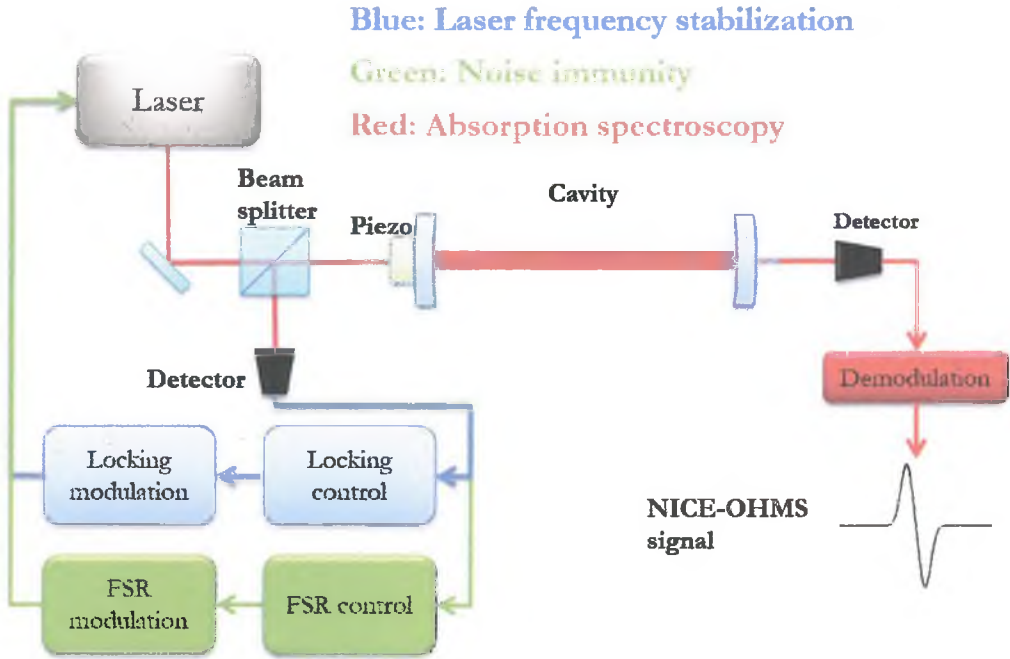


Figure 8.8: Schematic of a basic current modulated NICE-OHMS setup. Two modulations are employed, one for laser frequency stabilization (blue path) and one for noise immunity (green path). Molecular absorption spectroscopy is performed in transmission of the cavity (red path). Due to scanning over the absorption feature of a molecule, the cavity modes shift and the resulting detuning can be detected and corrected.

the red path. Assuming only small amounts of absorption, the final NICE-OHMS signal results from demodulation of the FSR reference signal with the transmission signal of the cavity. The Doppler-broadened NICE-OHMS signal can be obtained from Eq. 8.1.10, taking the cavity enhancement factor of  $2F/\pi$  into account [9, 15]

$$\begin{aligned}
 S^{\text{NICE-OHMS}} = \frac{2\mathcal{F}}{\pi} S_0 \left\{ \left[ f^{\text{abs}}(\nu_c - \nu_m) - f^{\text{abs}}(\nu_c + \nu_m) \right] \sin(\theta_{\text{FM}}) \right. \\
 \left. + \left[ f^{\text{disp}}(\nu_c - \nu_m) - 2f^{\text{disp}}(\nu_c) + f^{\text{disp}}(\nu_c + \nu_m) \right] \cos(\theta_{\text{FM}}) \right\} \quad (8.5.1)
 \end{aligned}$$

where  $2\mathcal{F}S_0/\pi$  is the NICE-OHMS signal strength. The shot noise limited absorption for a signal-to-noise ratio of 2 is derived from [9, 13]

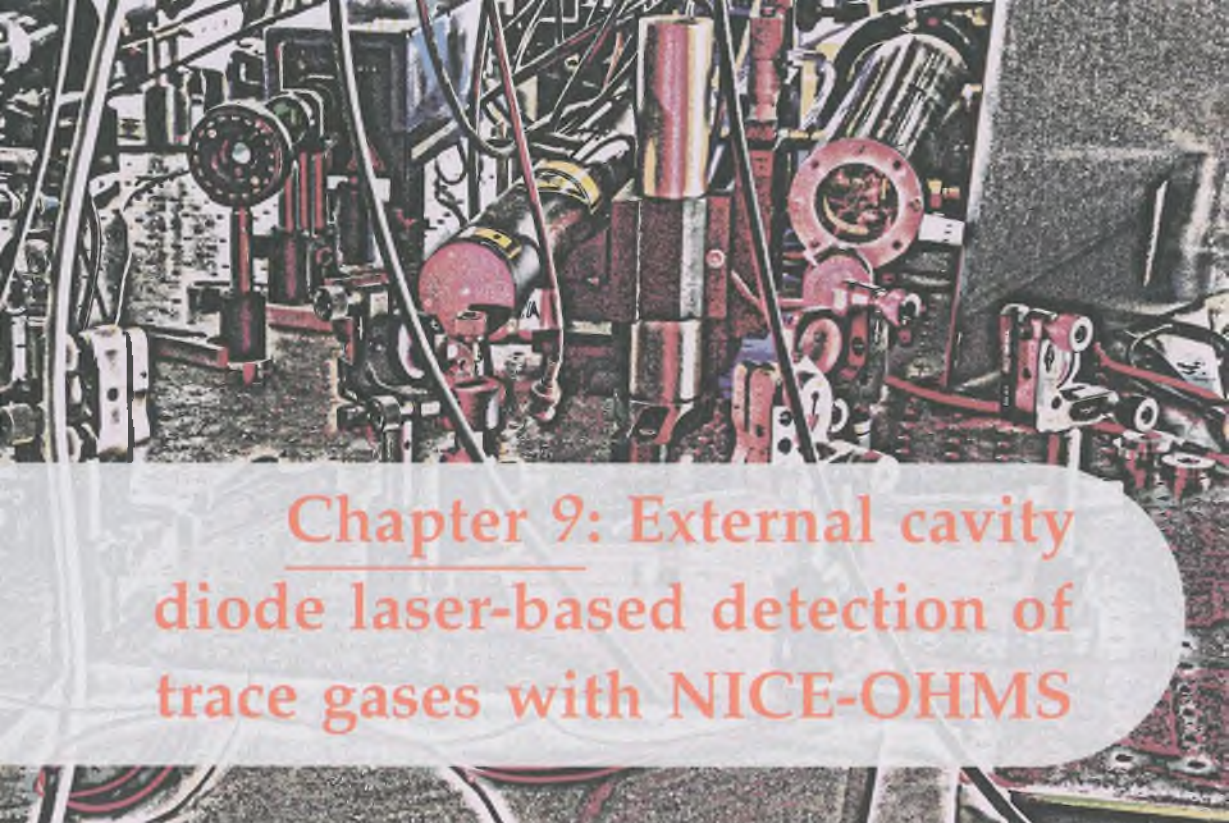
$$\text{NEAS}_{\text{shot}}^{\text{NICE-OHMS}} = \frac{\pi}{\mathcal{F}L} \sqrt{\frac{2e}{\eta_c \text{PN}_p}} \frac{1}{\sqrt{2}J_0(\beta)J_1(\beta)} \quad (8.5.2)$$

which simply increased the sensitivity value derived in Eq. 3.3.13 by the factor  $1/\left[\sqrt{2}J_0(\beta)J_1(\beta)\right]$  due to frequency modulation of the optical field. Since NICE-OHMS combines cavity enhanced spectroscopy with frequency modulation, it reaches detectivities closer the shot noise limit than the individual techniques. The best value of  $10^{-14}$  reached so far has been reported by Ye et al. in combination with a cavity finesse of  $10^5$  and sub-Doppler NICE-OHMS [13].

# References

- [1] G. C. Björklund, "Frequency-modulation spectroscopy: A new method for measuring weak absorptions and dispersions," *Optics Letters*, vol. 5, no. 1, pp. 15–17, 1980.
- [2] G. C. Björklund, M. Levenson, W. Lenth, and C. Ortiz, "Frequency modulation (FM) spectroscopy," *Applied Physics B*, vol. 32, no. 3, pp. 145–152, 1983.
- [3] J. Hall, L. Hollberg, T. Baer, and H. Robinson, "Optical heterodyne saturation spectroscopy," *Applied Physics Letters*, vol. 39, no. 9, pp. 680–682, 1981.
- [4] J. Hall, "Stabilized lasers and precision measurements," *Science*, vol. 202, no. 4364, pp. 147–156, 1978.
- [5] R. Drever, J. L. Hall, F. Kowalski, J. Hough, G. Ford, A. Munley, and H. Ward, "Laser phase and frequency stabilization using an optical resonator," *Applied Physics B*, vol. 31, no. 2, pp. 97–105, 1983.
- [6] R. V. Pound, "Electronic frequency stabilization of microwave oscillators," *Review of Scientific Instruments*, vol. 17, no. 11, pp. 490–505, 1946.
- [7] J. M. Supplee, E. A. Whittaker, and W. Lenth, "Theoretical description of frequency modulation and wavelength modulation spectroscopy," *Applied Optics*, vol. 33, no. 27, pp. 6294–6302, 1994.
- [8] E. A. Whittaker, M. Gehrtz, and G. C. Björklund, "Residual amplitude modulation in laser electro-optic phase modulation," *JOSA B*, vol. 2, no. 8, pp. 1320–1326, 1985.
- [9] A. Foltynowicz, *Fiber-laser-based noise-immune cavity-enhanced optical heterodyne molecular spectrometry*. PhD thesis, Umeå University, 2009.
- [10] R. W. Fox, C. W. Oates, and L. W. Hollberg, "Stabilizing diode lasers to high-finesse cavities," *Experimental Methods in the Physical Sciences*, vol. 40, pp. 1–46, 2003.
- [11] A. Foltynowicz, F. M. Schmidt, W. Ma, and O. Axner, "Noise-immune cavity-enhanced optical heterodyne molecular spectroscopy: Current status and future potential," *Applied Physics B*, vol. 92, no. 3, pp. 313–326, 2008.
- [12] L. Gianfrani, R. W. Fox, and L. Hollberg, "Cavity-enhanced absorption spectroscopy of molecular oxygen," *JOSA B*, vol. 16, no. 12, pp. 2247–2254, 1999.
- [13] J. Ye, L. S. Ma, and J. L. Hall, "Ultrasensitive detections in atomic and molecular physics: Demonstration in molecular overtone spectroscopy," *JOSA B*, vol. 15, no. 1, pp. 6–15, 1998.
- [14] M. S. Taubman, T. L. Myers, B. D. Cannon, and R. M. Williams, "Stabilization, injection and control of quantum cascade lasers, and their application to chemical sensing in the infrared," *Spectrochimica Acta Part A: Molecular and Biomolecular Spectroscopy*, vol. 60, no. 14, pp. 3457–3468, 2004.

- [15] P. Ehlers, A. C. Johansson, I. Silander, A. Foltynowicz, and O. Axner, "Use of etalon-immune distances to reduce the influence of background signals in frequency-modulation spectroscopy and noise-immune cavity-enhanced optical heterodyne molecular spectroscopy," *JOSA B*, vol. 31, no. 12, pp. 2938–2945, 2014.
- [16] P. C. Hobbs, "Noise cancelling circuitry for optical systems with signal dividing and combining means," July 28 1992. US Patent 5,134,276.
- [17] D. M. DeCain, P. C. Hobbs, and K. R. Pope, "Interferometer method for providing stability of a laser," July 10 2001. US Patent 6,259,712.
- [18] W. Zhang, M. Martin, C. Benko, J. Hall, J. Ye, C. Hagemann, T. Legero, U. Sterr, F. Riehle, G. Cole, *et al.*, "Reduction of residual amplitude modulation to  $1 \times 10^{-6}$  for frequency modulation and laser stabilization," *Optics Letters*, vol. 39, no. 7, pp. 1980–1983, 2014.
- [19] K. Ruxton, A. L. Chakraborty, W. Johnstone, M. Lengden, G. Stewart, and K. Duffin, "Tunable diode laser spectroscopy with wavelength modulation: Elimination of residual amplitude modulation in a phasor decomposition approach," *Sensors and Actuators B: Chemical*, vol. 150, no. 1, pp. 367–375, 2010.
- [20] R. DeVoe and R. Brewer, "Laser-frequency division and stabilization," *Physical Review A*, vol. 30, no. 5, p. 2827, 1984.



## Chapter 9: External cavity diode laser-based detection of trace gases with NICE-OHMS

This chapter is based on:

R. Centeno, J. Mandon, S.M. Cristescu, F.J.M. Harren, *External cavity diode laser-based detection of trace gases with NICE-OHMS using current modulation*, Optics Express, 23, 5, pp. 6277–6282 (2015),

<http://dx.doi.org/10.1364/OE.23.006277>

## Abstract

We combined an external cavity diode laser with noise-immune cavity-enhanced optical heterodyne molecular spectroscopy (NICE-OHMS) using current modulation. With a finesse of 1600, we demonstrate noise equivalent absorption sensitivities of  $4,1 \cdot 10^{-10} \text{ cm}^{-1} \text{ Hz}^{-1/2}$ , resulting in sub-ppbv detection limits for Doppler-broadened transitions of  $\text{CH}_4$  at  $6132,3 \text{ cm}^{-1}$ ,  $\text{C}_2\text{H}_2$  at  $6578,5 \text{ cm}^{-1}$  and  $\text{HCN}$  at  $6541,7 \text{ cm}^{-1}$ . The system was used for hydrogen cyanide detection from sweet almonds as an application.

## 9.1 Introduction

**N**OISE-IMMUNE cavity-enhanced optical heterodyne molecular spectroscopy (NICE-OHMS) is a laser-based spectroscopic detection method that combines the advantages of frequency modulation spectroscopy (FMS) and cavity enhancement, which are both sensitive spectroscopic methods, to achieve exceptionally high sensitivities for the detection of molecular gases. FMS is an optical heterodyne method that uses frequency modulation (FM) of laser light to produce sidebands on the laser frequency [1]. This modulation reduces the effect of  $1/f$ -noise for sufficiently high modulation frequencies and allows for the phase-sensitive detection of spectral features. With cavity-enhanced spectroscopy, the molecular gas is enclosed in a high finesse optical cavity to effectively increase the optical absorption path length. NICE-OHMS combines these two methods by locking the laser frequency to a longitudinal mode of the optical cavity, and an additional modulation frequency is introduced to exactly match the free spectral range (FSR). In this way, the transmitted FM triplet is kept balanced, because the three cavity modes interact with the three components of the triplet at exactly the same way. Therefore, the synchronous detection of the transmission signal at the FSR frequency is immune to the frequency-amplitude conversion noise between the incident laser and the cavity modes. NICE-OHMS has a very high sensitivity, because it combines FM with cavity enhanced absorption methods, where the FM signal is enhanced by a factor of  $2\mathcal{F}/\pi$ , with  $\mathcal{F}$  the cavity finesse. The method was originally developed in the 1990s by Ye et al. [2] for frequency standard applications based on a narrow line width Nd:YAG laser, achieving a minimum detectable absorption sensitivity (NEAS) of  $1 \cdot 10^{-14} \text{ cm}^{-1} \text{ Hz}^{-1/2}$  in 1 s averaging with a finesse of  $10^5$ . Continuing this research, the method has been implemented with various other lasers like fiber [3] or external cavity diode lasers (ECDL) [4–6]. The latter have a broader line width than Nd:YAG and fiber lasers, but possess the advantage of compactness and tunability over a wide wavelength range, making them ideal for molecular absorption applications in the near-IR. For example, Bell et al. detected  $\text{CH}_4$  using an ECDL, achieving a NEAS of  $4 \cdot 10^{-11} \text{ cm}^{-1} \text{ Hz}^{-1/2}$  with a finesse of 2600 [6]. The future potential for NICE-OHMS applications, however, resides in the realization of laser-based spectrometers operating in the molecular fingerprint region in the MIR. Recently, various MIR coherent light sources have been combined with NICE-OHMS, e.g. difference

frequency generation [7], optical parametrical oscillators [8] or quantum cascade lasers [9]. For most of these approaches, the optical field gets modulated via an electro-optical modulator (EOM). Furthermore, most RF components for laser frequency stabilization, FSR matching and signal acquisition have to be matched to the specifics of the setup, which increases the complexity of the system. The use of EOMs or current modulation produces residual amplitude modulation (RAM) that can be reduced by electronic or optical means [1]. RAM is generally seen as a slow variation in the background (see Section 8.4), which limits the signal-to-noise ratio of the NICE-OHMS signals. This places great constraints on the alignment perfection of an EOM to avoid RAM.

Additionally, in the MIR region, the use of EOMs becomes extremely costly. For further advancement of NICE-OHMS into the MIR and greater attractiveness for applications, a more straightforward approach and more user friendliness is essential. In this chapter, we present a NICE-OHMS setup in the near-IR implementing commercially available locking tools using current modulation of the laser field for all modulations. We chose to work initially in the near-IR due to the better quality of the sources and detectors to ease the transition to the mid-IR. We assessed the performance of the system using an ECDL for Doppler-broadened absorption spectroscopy of methane, acetylene and hydrogen cyanide (HCN). Additionally, we studied the dynamics of the HCN production in sweet almonds to verify the applicability and sensitivity of the NICE-OHMS apparatus.

## 9.2 Experimental setup

For NICE-OHMS, we applied two stages of FM to the laser light, which were demodulated sequentially. The first modulation ensured the lock of the laser to the cavity, while the second was at the cavity FSR to guarantee noise immunity. Below follows a description of the setup employing those two modulations to generate the NICE-OHMS signal.

A schematic of our experimental apparatus is shown in Fig. 9.1. The external cavity diode laser (ECDL) system (DL pro, Toptica, Germany) used for the stabilization and spectroscopic experiments had a line width of 60 kHz in less than 5  $\mu$ s, was tunable between 1510 – 1630 nm with a maximum output power of 50 mW and possessed two current modulation inputs. In the optical path between the ECDL and the optical cavity, two optical isolators (IO-4-1650-VLP, Thorlabs, Germany) were placed, passing through a half-wave plate ( $\lambda/2$ ), a quarter-wave plate ( $\lambda/4$ ) and a polarizing beam splitter (PBS) to optimize

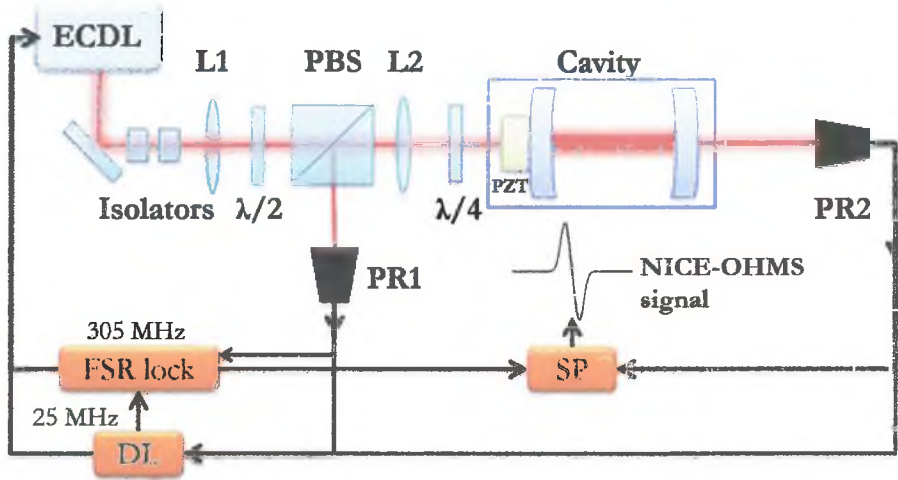


**Figure 9.1:** Schematic of the NICE-OHMS setup employing solely current modulation. ECDL: External Cavity Diode Laser; PBS: Polarizing beam splitter; PZT: Piezoelectric ring transducer;  $\lambda/2$  and  $\lambda/4$ : Half wave and quarter wave plate; PR1 and PR2: photoreceivers 1 and 2; DL: Digilock; SP: Signal processor, L1 and L2: mode-matching lenses.

the polarization and to separate the reflection signal from the incoming one. The optical isolators each provided 30 dB of isolation, protecting the ECDL from optical feedback from the cavity, which caused instabilities in the laser's frequency. The beam was mode-matched to the  $\text{TEM}_{00}$  mode of the cavity with two focusing lenses. Most optical elements were placed at etalon-free distances (integer multiples of the FSR) to couple a maximum of 65% of 0,5 mW incident power into the cavity [10]. The optical cavity was placed inside a vacuum chamber, which consisted of an invar tube to lower thermal influences and two CaF windows mounted under an angle ( $25^\circ$ ) to minimize reflections. This configuration was chosen to avoid the influence of pressure changes on the optical cavity. The optical cavity was formed by two high reflectivity mirrors (25 mm diameter, radius of curvature  $r = 1$  m, reflectivity  $R = 99,8\%$  at  $1,6 \mu\text{m}$ , Layertec, Germany) with a length of 49,2 cm, resulting in a cavity FSR of 304,9 MHz. One mirror was mounted on a piezoelectric ring actuator (Physik Instrumente P-025.40H) and was used for scanning the cavity length over a maximum of 6 GHz with a scanning rate of 5 Hz. Two photoreceivers (HCA-S-400M-IN-FS, bandwidth 400 MHz, FEMTO, Germany) monitored signals in reflection and transmission, which were used for laser frequency stabilization

and molecular spectroscopy. The wavelength was monitored with a wavelength meter (Bristol Instruments 621A, USA).

We measured three different gases covering almost the entire tuning range of the ECDL, namely  $\text{CH}_4$  at  $6132,3 \text{ cm}^{-1}$ ,  $\text{C}_2\text{H}_2$  at  $6578,5 \text{ cm}^{-1}$  and  $\text{HCN}$  at  $6541,7 \text{ cm}^{-1}$  without re-aligning or adapting the optical components. The cavity was evacuated to  $10^{-3}$  mbar before molecular gas was introduced via a mass flow controller (Brooks Instruments, Netherlands).

Two servo-locking systems existed in our NICE-OHMS setup. The first was used to lock the laser to a cavity mode and the second to match the frequency of the FSR. For this, our setup employed two modulation frequencies at 25 and 305 MHz, both added to the current of the laser via a Bias-T on one of the current inputs. The laser frequency was locked to a longitudinal mode of the cavity by the Pound-Drever-Hall (PDH) method ( $\beta = 0,12$ ) [11]. Upon reflection from the first cavity mirror, the light was directed via the PBS and a  $\lambda/4$ -plate to the photodiode. The resulting signal was demodulated to generate an error signal, which was fed to a noise canceler based on the patent of DeCain et al. [12, 13] and a commercial Toptica Digilock in order to maintain the laser frequency at the peak of the cavity resonance. The Digilock required minimal setting adjustment and the automated locking procedure was straightforward. Evaluation of the transfer functions of the laser and the locking servo occurred via internal routines. The servo loop had a bandwidth of 1 MHz and allowed for fast feedback to the laser current via a second current input, whereas low frequency signals were fed back to the laser piezo to allow a wide tuning range. Once locked with sufficient bandwidth, the cavity could be swept over 6 GHz, while the laser was following it.

The second modulation frequency, employed at  $\nu_{\text{FSR}}$  for noise immunity, was injected into the current at 305 MHz ( $\beta = 0,54$ ). The noise-immune aspect of NICE-OHMS required a good match between the modulation frequency and  $\nu_{\text{FSR}}$ . For this we used the locking scheme by DeVoe and Brewer [14]. A fraction of the cavity reflection signal was split off and demodulated at 280 MHz (the difference of  $\nu_{\text{FSR}}$  and  $\nu_{\text{PDH}}$ ) in a double balance mixer (Mini-Circuits ZLW-1, USA) to produce the error signal. A commercial PID controller with a 300 kHz bandwidth then matched the frequency of the oscillator to the FSR frequency. To produce the NICE-OHMS signal, the transmission signal was high-pass filtered (Mini-Circuits SHP-175) and then demodulated at  $\nu_{\text{FSR}}$  with a double balance mixer (Mini-Circuits ZLW-1). This signal was passed through an 80 Hz low-pass filter (Mini-Circuits PLP-10.7) and recorded via the data acquisition card.

Changing the demodulation phase allowed either the absorption or dispersion FMS signal to be acquired. After the data had been collected, it was sent to a data acquisition card (NI-6259, National Instruments), averaging five individual spectra (870 points) in an acquisition time of 1 s for post processing in Matlab to fit the measured NICE-OHMS lineshape function using Eq. 8.5.1.

### 9.3 Results and discussion

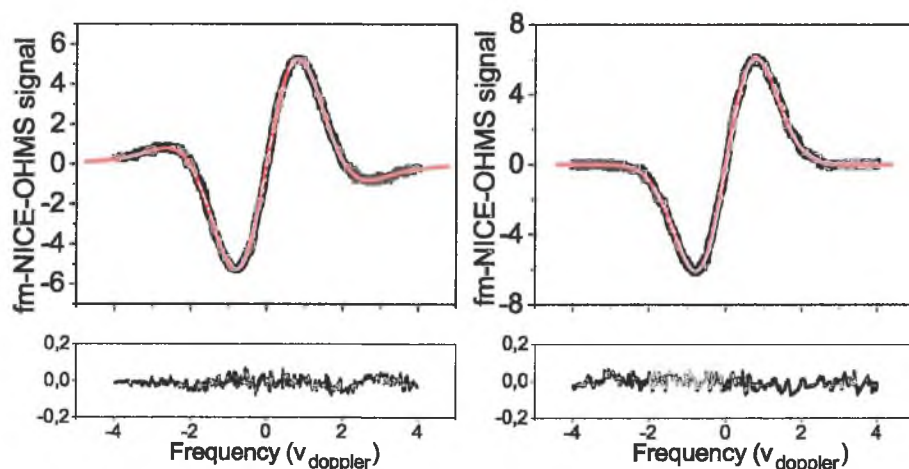


Figure 9.2: NICE-OHMS signal of 200 ppbv methane at  $6132,3 \text{ cm}^{-1}$  for dispersion (panel (a)) and absorption (panel (b)) as a function of the Doppler frequency (473 MHz). Black dots represent measurement points with a fit in red. Residuals of each plot are given below their respective graph.

To analyze the performance of the spectrometer over a broad wavelength range and to demonstrate that capability of the current modulation approach, this section details measurements of molecular transitions of methane, acetylene and HCN. Figure 9.2 shows an Doppler-broadened NICE-OHMS signal for both the dispersion (panel (a)) and the absorption case (panel (b)) for a concentration of 200 ppbv methane in  $\text{N}_2$  at 3 mbar at a wavelength of  $6132,3 \text{ cm}^{-1}$  with a scanning rate of 5 Hz over 1,5 GHz. At this pressure, no sub-Doppler features were visible in the spectrum. With a modulation index of  $\beta = 0,54$ , the RAM in the system amounted to  $\sim 6\%$ .

A similar approach was used to acquire absorption NICE-OHMS signals for 100 ppbv  $\text{C}_2\text{H}_2$  at  $6578,5 \text{ cm}^{-1}$  and 200 ppbv HCN at  $6541,7 \text{ cm}^{-1}$  at 3

mbar, shown in Fig. 9.3(b) and 9.3(c), respectively. As acetylene has the greatest integrated line strength in this region, its resulting absorption signal was the strongest of all three compounds. Due to the shift to a wavelength on the other end of the tuning range of the laser, the optical isolators were not able to suppress etalon effects strongly, which resulted in the intensity variations clearly seen in the spectra of acetylene and HCN.

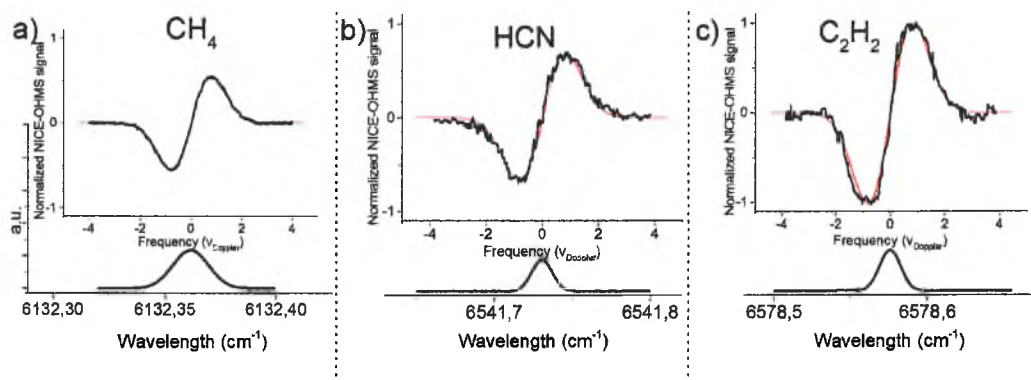


Figure 9.3: Measured (black line) and simulated (red line) NICE-OHMS absorption signals at 3 mbar from (a) 200 ppbv of methane, (b) 200 ppbv of HCN and (c) 100 ppbv of acetylene together with simulated absorption peaks at their respective wavelength below the corresponding graph.

The noise equivalent absorption sensitivity (NEAS) per point of the setup was calculated using Eq. 3.3.12 for all three wavelengths. The best achieved NEAS at  $6132,2 \text{ cm}^{-1}$  had a value of  $\text{NEAS} = 4,1 \cdot 10^{-10} \text{ cm}^{-1} \text{ Hz}^{-1/2}$ . The theoretical shot-noise limited noise equivalent absorption sensitivity of the NICE-OHMS setup is given by Eq. 5.5.2,  $\text{NEAS}_{\text{sh}} = 3,8 \cdot 10^{-12} \text{ cm}^{-1} \text{ Hz}^{-1/2}$ . Thus the sensitivity reported here is a factor 100 above the shot-noise limit. The detection limits were calculated by dividing the concentration of the gas under study by the signal-to-noise ratio (SNR), which gave a value of 0,93 ppbv for methane with a SNR of 215. The SNR was calculated by dividing half the peak-to-peak value of the NICE-OHMS signal by the root-mean-square of the data. For acetylene and HCN the detection limit deteriorated a factor 2 and 3,5, respectively. This was a direct result of the increased noise on the NICE-OHMS signal.

Having shown the performance capability of the system and multiple absorption measurements, we applied the NICE-OHMS system to the detection of HCN emission from sweet almonds. Figure 9.4 shows the dynamics of the HCN production over time, where the resulting HCN concentration was

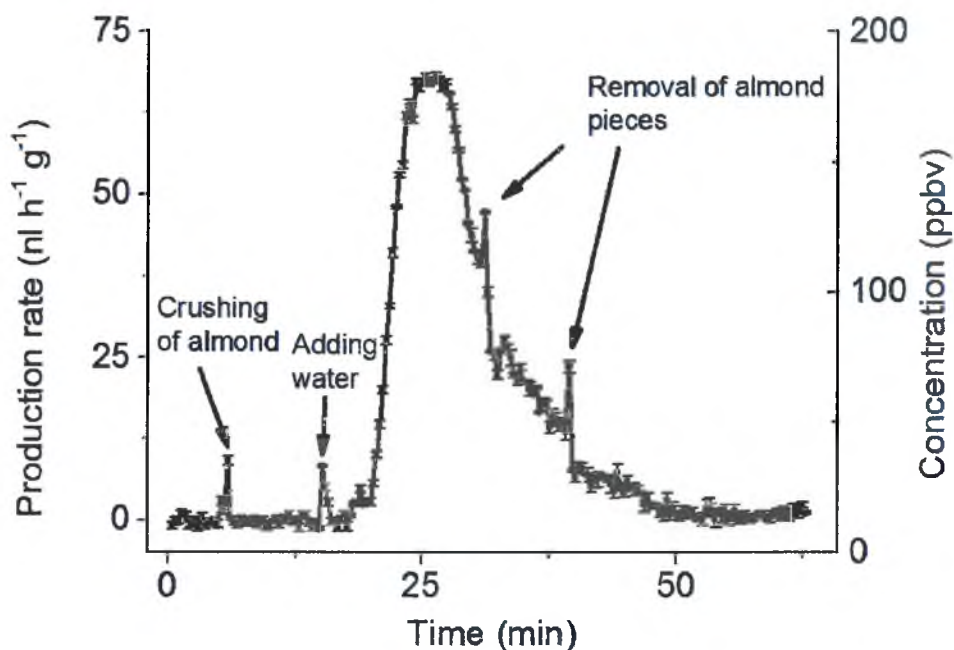


Figure 9.4: Dynamics of HCN production in sweet almonds over 75 min. The values are means of the production rate of three repeated experiments. The almonds were crushed after 15 min and started to produce HCN with a maximum of  $68 \text{ nl h}^{-1} \text{ g}^{-1}$  10 min after crushing. In intervals of 10 min, half the almond pieces were removed. The production of HCN in the remaining almond pieces ceased after 60 min.

expressed in emission rate per weight,  $\text{nl h}^{-1} \text{ g}^{-1}$ . The data was averaged over 100 scans every 20 s and the experiment was repeated three times. Initially, the almonds were flushed at 1 l/h with  $\text{N}_2$  at room temperature in a glass cuvet for 5 min, after which they were crushed. The peaks in Fig. 9.4 indicate a disturbance in the system due to the opening of the cuvette. At first, no HCN was present even after crushing, while the introduction of 1 ml of water after 15 min fueled the HCN production. After 2 min, the HCN production rose from 0  $\text{nl h}^{-1} \text{ g}^{-1}$  to  $68 \text{ nl h}^{-1} \text{ g}^{-1}$  within 7 min. Here, the values remained constant for 3 min, after which the amount of produced HCN decreased steadily. At 30 min and 39 min, half of the almond pieces were removed from the cuvet, lowering the production rate by a factor of  $\sim 2$ . From 40 min on, the HCN

values fell off exponentially until the production completely ceased at 60 min. For comparison and validation was the data compared to previously taken measurements (data not shown) with almonds from the same group taken with an OPO-based photoacoustic setup described elsewhere [15]. The production rates were comparable and the time-dependency showed identical behavior.

The two common noise sources of NICE-OHMS setups were also present in our system: Etalon effects, created by reflections between optical surfaces, and RAM, generated by the conversion from FM to AM during the modulation of the current. The former could be minimized by placing optical elements at etalon immune distances and by adding an anti-reflection coating to the surfaces. Additionally, optical isolators in front of the laser were important to suppress any feedback into the laser, which greatly disturbed the stability of the laser's frequency. For the transitions we studied, RAM was mostly removed by background subtraction in the noise canceler and the optimization of the PDH modulation frequency [9, 12]. In general, using the whole tuning range made the system less sensitive as compared to a situation, where the system would be optimized for a specific wavelength. This is clearly seen in the increased noise after changing the laser wavelength by  $\sim 400 \text{ cm}^{-1}$ . In addition, the use of a generic commercial device locking device yielded only average lock quality and performed less than a specifically matched one. For example, the Digilock contained only a single stage PID controller, whereas a double integrator was needed to achieve sensitivities of  $\sim 10^{-12} \text{ cm}^{-1} \text{ Hz}^{-1/2}$  [16, 17]. When utilizing a cavity finesse in the order of  $10^4$  or higher, it would be very difficult to lock the laser to it with the current commercially available devices as the lock needs to be much more stable to keep the laser in the narrow cavity mode. In addition, from the above measurements across the tuning range of the laser, it becomes clear that the use of a commercial servo lock has its limitations with respect to locking bandwidth and efficiency, if the transfer functions of the laser and the cavity change by tuning the laser wavelength. Nonetheless, employing current modulation and commercial devices reduced the time-consuming procedure of precise EOM alignment and fabrication of advanced home-made electronics. In spite of the variation in sensitivity across the tuning range, this system presented here has the ability to apply NICE-OHMS to various molecular gases, achieving only slightly worse sensitivity values compared to other ECDL-based systems of  $\sim 10^{-11} \text{ cm}^{-1} \text{ Hz}^{-1/2}$  with higher cavity finesse and additional wavelength modulation [4, 6]. The system can be enhanced by the use of a higher cavity finesse and more advanced servo circuitry. However, the key issue here was not

to strive for a better performance or stability, but for a simplification, such that the NICE-OHMS method can be employed efficiently with MIR laser systems. Therefore, in the near future, we will evaluate the implementation of current modulated NICE-OHMS with a broadband laser in the MIR region.

## 9.4 Conclusion

In summary, we have presented a simplified approach to implement the NICE-OHMS method using current modulation and commercial devices. A full description of our NICE-OHMS apparatus was given, and measurements of methane, acetylene and hydrogen cyanide at sub-ppbv levels were shown, resulting in noise equivalent absorption sensitivities of  $4,1 \cdot 10^{-10} \text{ cm}^{-1} \text{ Hz}^{-1/2}$ . The dynamics of the HCN production in sweet almonds was used to show the system's stability and applicability to sensitive trace gas detection. We aim to apply this current modulation approach in the MIR region for the sensitive detection of broadband absorption molecules.

# References

- [1] G. C. Björklund, M. Levenson, W. Lenth, and C. Ortiz, "Frequency modulation (FM) spectroscopy," *Applied Physics B*, vol. 32, no. 3, pp. 145–152, 1983.
- [2] J. Ye, L. S. Ma, and J. L. Hall, "Ultrasensitive detections in atomic and molecular physics: Demonstration in molecular overtone spectroscopy," *JOSA B*, vol. 15, no. 1, pp. 6–15, 1998.
- [3] A. Foltynowicz, W. Ma, and O. Axner, "Characterization of fiber-laser-based sub-doppler NICE-OHMS for quantitative trace gas detection," *Optics Express*, vol. 16, no. 19, pp. 14689–14702, 2008.
- [4] L. Gianfrani, R. W. Fox, and L. Hollberg, "Cavity-enhanced absorption spectroscopy of molecular oxygen," *JOSA B*, vol. 16, no. 12, pp. 2247–2254, 1999.
- [5] N. J. van Leeuwen, A. C. Wilson, *et al.*, "Measurement of pressure-broadened, ultraweak transitions with noise-immune cavity-enhanced optical heterodyne molecular spectroscopy," *JOSA B*, vol. 21, no. 10, pp. 1713–1721, 2004.
- [6] C. Bell, G. Hancock, R. Peverall, G. Ritchie, J. van Helden, and N. van Leeuwen, "Characterization of an external cavity diode laser based ring cavity NICE-OHMS system," *Optics Express*, vol. 17, no. 12, pp. 9834–9839, 2009.
- [7] M. W. Porambo, B. M. Siller, J. M. Pearson, and B. J. McCall, "Broadly tunable mid-infrared noise-immune cavity-enhanced optical heterodyne molecular spectrometer," *Optics Letters*, vol. 37, no. 21, pp. 4422–4424, 2012.
- [8] K. N. Crabtree, J. N. Hodges, B. M. Siller, A. J. Perry, J. E. Kelly, P. A. Jenkins II, and B. J. McCall, "Sub-doppler mid-infrared spectroscopy of molecular ions," *Chemical Physics Letters*, vol. 551, pp. 1–6, 2012.
- [9] M. S. Taubman, T. L. Myers, B. D. Cannon, and R. M. Williams, "Stabilization, injection and control of quantum cascade lasers, and their application to chemical sensing in the infrared," *Spectrochimica Acta Part A: Molecular and Biomolecular Spectroscopy*, vol. 60, no. 14, pp. 3457–3468, 2004.
- [10] P. Ehlers, A. C. Johansson, I. Silander, A. Foltynowicz, and O. Axner, "Use of etalon-immune distances to reduce the influence of background signals in frequency-modulation spectroscopy and noise-immune cavity-enhanced optical heterodyne molecular spectroscopy," *JOSA B*, vol. 31, no. 12, pp. 2938–2945, 2014.
- [11] R. Drever, J. L. Hall, F. Kowalski, J. Hough, G. Ford, A. Munley, and H. Ward, "Laser phase and frequency stabilization using an optical resonator," *Applied Physics B*, vol. 31, no. 2, pp. 97–105, 1983.
- [12] D. M. DeCain, P. C. Hobbs, and K. R. Pope, "Optical interferometer measurement apparatus and method," Nov. 16 1999. US Patent 5,986,759.

- [13] P. C. Hobbs, "Noise cancelling circuitry for optical systems with signal dividing and combining means," July 28 1992. US Patent 5,134,276.
- [14] R. DeVoe, C. Fabre, K. Jungmann, J. Hoffnagle, and R. Brewer, "Precision optical-frequency-difference measurements," *Physical Review A*, vol. 37, no. 5, p. 1802, 1988.
- [15] D. D. Arslanov, M. P. Castro, N. A. Creemers, A. H. Neerincx, M. Spunei, J. Mandon, S. M. Cristescu, P. Merkus, and F. J. Harren, "Optical parametric oscillator-based photoacoustic detection of hydrogen cyanide for biomedical applications," *Journal of Biomedical Optics*, vol. 18, no. 10, pp. 107002–107002, 2013.
- [16] P. Ehlers, I. Silander, J. Wang, A. Foltynowicz, and O. Axner, "Fiber-laser-based noise-immune cavity-enhanced optical heterodyne molecular spectrometry incorporating an optical circulator," *Optics Letters*, vol. 39, no. 2, pp. 279–282, 2014.
- [17] O. Axner, P. Ehlers, T. Hausmaninger, I. Silander, and W. Ma, "Noise-immune cavity-enhanced analytical atomic spectrometry - NICE-AAS - a technique for detection of elements down to zeptogram amounts," *Spectrochimica Acta Part B: Atomic Spectroscopy*, vol. 100, pp. 211–235, 2014.





## Summary

**T**HE STUDY OF INTERACTIONS BETWEEN LIGHT AND MATTER has been in the focus of modern scientific and technological developments, and has resulted in world changing inventions such as light emitting diodes and lasers. These inventions gave rise to a variety of potential applications such as free-space optical communication and molecular spectroscopy and, as a result from the latter, enabled high-sensitivity trace gas sensing and non-invasive breath analysis. Trace gas detection is an attractive research area important for both fundamental research and industrial applications. The advantages of the trace gas detection are evident: safety, non-invasiveness and reliability. Nowadays, there is a range of well-established trace gas detection methods such as chemiluminescence, gas chromatography, electronic nose and mass-spectrometry. However, advances in the development of infrared laser sources with high power, narrow linewidth and broad tuning range have made laser-based absorption spectroscopy a powerful tool for trace gas sensing. Laser-based spectrometers have significantly simplified the analysis of complex gas mixtures offering high sensitivity, selectivity and the potential for further miniaturization. To meet such ends, in this thesis several developed laser-based trace gas sensors in the near- and mid-infrared wavelength region are presented and their application to fruit storage and breath analysis is shown. The development of

several laser-based detectors and their applications aims to provide the reader with new insights into the possibilities of laser-based trace gas detection.

The MIR spectral range (2 – 25  $\mu\text{m}$ ) is particularly useful for chemical sensing due to the excitation of fundamental rotational and vibrational modes. In the 'fingerprint region' (2 – 20  $\mu\text{m}$ ), most molecules have unique absorption patterns, which provide absorption measurements with high selectivity. A quantum cascade laser (QCL), a coherent radiation source in the mid-infrared (MIR) wavelength region, presents an ideal light source for MIR chemical sensing due to its narrow linewidth, high spectral density, compact size, and ease of fabrication of nearly any MIR wavelength. QCLs are semiconductor devices, in which laser action takes place between intersubband transitions in quantum wells. The lasing emission is determined through the layer sequence of the heterostructure and lasers can therefore be engineered to emit in most of the MIR and far-infrared spectral regions. The laser emission frequency is selected to match a strong absorption feature for the analyte of interest, where no other interfering bands are located. As a result, high sensitivity measurements have been achieved in both gas and liquid phase. One of the primary goals of the present work was the development and application of high performance QCL-based spectrometers in the MIR wavelength region. Although the QCL technology has been undergoing a rapid and steady development phase ever since its invention in 1994, further improvements of QCL-based trace gas sensors are essential with regards to sensitivity, accuracy and cost-effectiveness for their commercial implementation. Chapter 2 provides an overview of the working principle of a QCL, its advantages and an overview of its different applications. The demonstrations of gas phase MIR sensors in this work advance the field towards finding key applications in medical, biological, environmental, and atmospheric measurements.

Laser-based trace gas detection uses spectral features of molecules to assess their quantity in a gaseous mixture. All experiments described in this thesis utilized absorption spectroscopy, a detection method described in detail in Chapter 3. Here, a description and discussion of the used detection methods is given.

Ethylene plays an important role in plant growth and development. Chapter 4 presents spectroscopic studies of ethylene using a pulsed QCL-based infrared spectrometer coupled to an optical cavity. We describe the optimization of the spectrometer, which operated at 10,9  $\mu\text{m}$  and used off-axis integrated cavity output spectroscopy (OA-ICOS), in the presence of high water and  $\text{CO}_2$  for use

in fruit storage. Details of the development of the spectrometer and the results of measuring the ethylene production in commercial Elstar apples are presented. In addition, we investigate the use of an additional third mirror in front of the optical cavity to re-inject the light. Due to this re-injection process, the sensitivity of the system could be enhanced by a factor 4 to 10 ppbv in 128 s.

Chapter 5 investigates, which parameters of the setup presented in Chapter 4 influence the most the enhancement of the re-injection process. We simulated and experimentally verified that the angle of injection and the ratio of distance to radius of curvature are essential for the optimal re-injection, which resulted in an increase in sensitivity of a factor 10 and in a noise equivalent absorption sensitivity (NEAS) of  $1,5 \cdot 10^{-8} \text{ cm}^{-1} \text{ Hz}^{-1/2}$ .

Although other MIR spectrometers (i.e. Fourier Transform Spectrometers) have a wide spectral range for multi-species and broadband molecular detection, they are too large and utilize too slow scan rates for practical use in high resolution spectroscopic applications. A QCL placed inside a diffraction grating based external cavity arrangement can easily provide  $> 100 \text{ cm}^{-1}$  frequency range with an output power in the order of tens of mW and a linewidth in the order of kHz. Therefore, an external cavity QCL (EC-QCL) provides both high spectral resolution and a wide frequency range. Chapter 6 describes the development of a home-made continuous wave EC-QCL in the Littrow configuration suitable for the detection of molecular gases with broadband absorption features. This device showed a maximum spectral coverage of more than  $300 \text{ cm}^{-1}$  and operated between  $1129$  and  $1432 \text{ cm}^{-1}$  ( $6,98 - 8,86 \text{ }\mu\text{m}$ ) producing  $\sim 200 \text{ mW}$  of output power at  $243 \text{ K}$ . Combined with OA-ICOS, the detection of broadband absorption molecules such as acetone resulted in a NEAS for the EC-QCL spectrometer of  $3,7 \cdot 10^{-8} \text{ cm}^{-1} \text{ Hz}^{-1/2}$ .

Chapter 7 emphasizes on the application of the developed spectrometer introduced in Chapter 6. This device was used for the detection of acetone and ethanol, both having broad absorption features, which distributed feedback (DFB)-QCLs cannot scan entirely. The correct assessment of the quantity of a gas depends, among other factors, on the selectivity of the sensor. For the determination of the acetone concentration in breath, mostly water and  $\text{CO}_2$  have been considered as the main interfering gases. However, research indicated that ethanol levels in breath can be of the same order as acetone levels. Using a wavelength of  $1216 \text{ cm}^{-1}$ , where acetone has been measured in earlier studies, we found that the relative error in acetone concentrations to the presence of ethanol in breath amounts up to 39%. As the absorption spectra of both

molecules overlap in the MIR range, measuring the full absorption profile of both gases enhances the accuracy of the measurements. We showed that the EC-QCL-based spectrometer is able to distinguish these molecules and accurately determined their concentration by correlating the measurements to data taken with a proton-transfer reaction mass spectrometer.

The most sensitive absorption method of today is noise-immune cavity-enhanced optical heterodyne molecular spectroscopy (NICE-OHMS). This method comprises of several approaches, cavity enhanced spectroscopy to enhance the optical path length and frequency modulation for noise reduction and laser frequency stabilization. However, due to its complexity, the method has so far not been applied to practical trace species detection. Chapter 8 provides insight into the aforementioned methods and describe how they are combined in NICE-OHMS, which has been extensively applied in the near-infrared region. To make this method more attractive and to be able to apply it effectively with broadly tunable MIR lasers, its complexity has to be reduced. For this end, we developed a NICE-OHMS system based on an external cavity diode laser between 1510 – 1630 nm using commercial devices and current modulation for the stabilization of the laser frequency. Chapter 9 presents the results of spectroscopic measurements of acetylene, methane and hydrogen cyanide (HCN) with the NICE-OHMS sensor. We showed a NEAS of  $4,1 \cdot 10^{-10} \text{ cm}^{-1} \text{ Hz}^{-1/2}$  with a cavity finesse of 1570 and a sensitivity of 0,93 ppbv. In addition, the system was applied to the detection of HCN in sweet almonds.



## Samenvatting

**D**E STUDIE NAAR DE INTERACTIES TUSSEN LICHT EN MATERIE is een pijler van de moderne wetenschappelijke en technologische ontwikkelingen en leidde tot wereldveranderende uitvindingen zoals licht emitterende diodes en lasers. Deze uitvindingen gaven aanleiding tot diverse mogelijke toepassingen zoals vrije-ruimte optische communicatie en moleculaire spectroscopie en als gevolg van de laatste maakten ze de zeer gevoelige sporengasdetectie en niet-invasieve ademanalyse mogelijk. Sporengasdetectie is een aantrekkelijk onderzoeksgebied, wat zowel belangrijk is voor fundamenteel onderzoek als voor industriële toepassingen. De voordelen van sporengasdetectie zijn evident: het is veilig, niet-invasief en betrouwbaar. Tegenwoordig worden verschillende methoden voor de detectie van sporengassen gebruikt, bijvoorbeeld chemiluminescentie, gaschromatografie, een elektronische neus en proton-transfer massaspectrometrie. Echter, de vooruitgang in de ontwikkeling van infrarode laserbronnen met een hoog vermogen, smalle lijnbreedte en brede golflengte afstembaarheid, hebben op laser gebaseerde absorptie spectroscopie een krachtig hulpmiddel voor sporengasdetectie gemaakt. Op laser gebaseerde spectrometers hebben de analyse van complexe gasmengsels met een hoge gevoeligheid aanzienlijk vereenvoudigd door hun selectiviteit en de potentie voor verdere miniaturisatie. Voor deze doeleinden worden in dit proefschrift een aantal ontwikkelde op laser gebaseerde sporengassensoren in het nabije en

mid-infrarode golflengtegebied beschreven en hun toepassing in fruit opslag en ademanalyse. De ontwikkeling van op verschillende laser gebaseerde detectoren en hun toepassingen is bedoeld om de lezer nieuwe inzicht te geven in de mogelijkheden van laser gebaseerde sporengasdetectie.

Het MIR bereik ( $2 - 25 \mu\text{m}$ ) is bijzonder nuttig voor chemische detectie door de excitatie van fundamentele rotatie en vibratiemodes. In het 'vingerafdruk gebied', ( $2 - 20 \mu\text{m}$ ), hebben de meeste moleculen unieke absorptie patronen, die absorptie metingen met een hoge gevoeligheid mogelijk maken. Een kwantumcascadelaser (QCL), een coherente stralingsbron in het midden-infrarood (MIR) golflengtegebied, presenteert een ideale lichtbron voor de chemische gasdetectie in het MIR gebied door zijn smalle lijnbreedte, hoge spectrale dichtheid, compactheid en het gemak van de fabricage van bijna elke MIR golflengte. QCLs zijn halfgeleiders, waarin laseractie plaatsvindt tussen elektrische subbanden in kwantumputten. De laseremissie wordt bepaald door de volgorde van de heterostructuur en lasers kunnen dus worden ontworpen om licht uit te zenden in het MIR en ver-infrarode spectrale gebied. De laserfrequentie wordt geselecteerd, zodat hij overeenkomt met een sterke absorptielijn van het molecuul, waar zich geen andere storende absorptiebanden bevinden. Als gevolg werden metingen met hoge gevoeligheid gerealiseerd in zowel de gas- als ook de vloeistoffase. Een van de belangrijkste doelstellingen in dit proefschrift was de ontwikkeling en toepassing van goed presterende spectrometers gebaseerd op QCLs in het MIR golflengtegebied. Hoewel de QCL technologie een snelle en stabiele ontwikkelingsfase ondergaat sinds zijn uitvinding in 1994, zijn verdere verbeteringen van op QCL-gebaseerde sporengassensoren essentieel met betrekking tot gevoeligheid, nauwkeurigheid en kosteneffectiviteit voor de commerciële realisatie. Hoofdstuk 2 geeft een overzicht van het werkingsprincipe van een QCL, zijn voordelen en een overzicht van de verschillende toepassingen. De demonstraties van de MIR sensoren in dit proefschrift hebben significante meerwaarde voor dit onderzoeksgebied door het vinden van de belangrijkste toepassingen in de medische, biologische, ecologische, en atmosferische metingen.

Laser gebaseerde sporengasdetectie maakt gebruik van spectrale kenmerken van moleculen om hun hoeveelheid te beoordelen in een gasmengsel. Alle experimenten in dit proefschrift maken gebruik van absorptie spectroscopie, een detectiemethode, welke in detail in hoofdstuk 3 beschreven wordt. Daarnaast wordt een spectroscopische methode door middel van optische resonatoren beschreven.

Ethyleen speelt een belangrijke rol in de groei en ontwikkeling van planten. Hoofdstuk 4 presenteert een spectroscopisch onderzoek van ethyleen, gebaseerd op een gepulseerde-QCL spectrometer gekoppeld aan een optische holte. We beschrijven de optimalisatie van een spectrometer, die wordt gebruikt in fruit opslag bij een hoge water en CO<sub>2</sub> concentratie, en werkt bij 10,9 μm in combinatie met off-axis integrated cavity output spectroscopy (OA-ICOS). Details van de ontwikkeling van de spectrometer en de resultaten van de metingen van de ethyleenproductie van commerciële Elstar appels worden gepresenteerd. Bovendien onderzoeken we het gebruik van een extra derde spiegel voor de optische holte voor het opnieuw injecteren van het gereflecteerde licht. Door dit herinjectie proces kan de gevoeligheid van het systeem worden verbeterd met een factor 4 met een detectielimiet van 10 ppbv in 128 s.

Hoofdstuk 5 onderzoekt, welke parameters van het systeem, beschreven in hoofdstuk 4, de meeste invloed heeft op de verbetering van het herinjectie proces. Door middel van simulaties en experimentele verificatie werd aangetoond, dat de hoek van injectie en de verhouding van de afstand tot kromtestraal van de spiegel essentieel is voor de optimale herinjectie, waardoor een toename in gevoeligheid van een factor 10 en een noise equivalent absorption sensitivity (NEAS) van  $1,5 \cdot 10^{-8} \text{ cm}^{-1} \text{ Hz}^{-1/2}$  werd bereikt.

Hoewel andere MIR spectrometers (d.w.z. Fourier Transform Spectrometers) een breed spectrum kunnen meten voor meerdere soorten en breedbandige moleculaire detectie, zijn ze te groot en veranderen te langzaam van golflengte voor praktisch gebruik in spectroscopische toepassingen met hoge resolutie. Een QCL geplaatst in een external cavity arrangement kan gemakkelijk  $> 100 \text{ cm}^{-1}$  afstembaar frequentiebereik bieden, waarbij het vermogen in de orde van tientallen mW ligt en de lijnbreedtes in de orde van kHz. Daarom levert een external cavity QCL (EC-QCL) zowel een hoge spectrale resolutie als ook een breed frequentiebereik. Hoofdstuk 6 beschrijft de ontwikkeling van een zelf geconstrueerde continuous wave EC-QCL in de Littrow configuratie, die geschikt is voor de detectie van moleculaire gassen met breedband absorptiepatronen. Dit apparaat geeft een maximaal spectraal bereik van meer dan  $300 \text{ cm}^{-1}$ , opereert tussen de 1129 en  $1432 \text{ cm}^{-1}$  (6,98 – 8,86 μm) en produceert een uitgangsvermogen van ~200 mW bij 243 K. Door de spectrometer met OA-ICOS te combineren, kunnen we breedbandige absorptiepatronen van moleculen zoals aceton detecteren en een NEAS van  $3,7 \cdot 10^{-8} \text{ cm}^{-1} \text{ Hz}^{-1/2}$  bereiken.

Hoofdstuk 7 legt de nadruk op de toepassing van de ontwikkelde spectrometer uit hoofdstuk 6. Deze apparatuur werd gebruikt voor de detectie van aceton en ethanol, beide met brede absorptiebanden, die distributed feedback QCLs niet volledig kunnen scannen. De juiste meting van de hoeveelheid van een bepaald gas is afhankelijk van, onder andere, de selectiviteit van de sensor. Voor de bepaling van de concentratie van aceton in de adem worden meestal water en CO<sub>2</sub> als de voornaamste storende gassen beschouwd. Uit onderzoek bleek, dat ethanol waardes in adem van dezelfde orde van grootte zijn als aceton waardes. Met een golflengte van 1216 cm<sup>-1</sup>, waarbij aceton in eerdere studies werd gemeten, vonden we dat de relatieve fout in aceton concentraties tot 39 % bedraagt in de aanwezigheid van ethanol in adem. Aangezien de absorptiespectra van beide moleculen overlappen in het MIR bereik, verbetert het meten van het volledige absorptieprofiel van beide gassen de nauwkeurigheid van de metingen. We zagen, dat de op de EC-QCL-gebaseerde spectrometer deze moleculen kon onderscheiden en de concentratie nauwkeurig werd bepaald door de metingen te correleren met data gemeten met een proton-transfer reaction mass spectrometer.

De huidige meest gevoelige absorptiemethode is noise-immune cavity enhanced optical heterodyne molecular spectroscopy (NICE-OHMS). Deze methode bestaat uit verschillende methodes, namelijk cavity enhanced spectroscopy om de optische padlengte te verhogen, en frequentie modulatie voor ruisonderdrukking en de stabilisatie van de laser frequentie. Vanwege de complexiteit werd deze detectiemethode tot nu toe niet toegepast op in de praktijk voor sporengasdetectie. Hoofdstuk 8 geeft inzicht in de genoemde methoden en beschrijven hoe ze worden gecombineerd in NICE-OHMS, welke uitvoerig in het nabij-infrarode gebied werden toegepast. Om deze methode aantrekkelijker maken en effectief toe te kunnen passen op breed afstembare lasers in het MIR gebied, is het noodzakelijk om de complexiteit te verminderen. Voor dit doel hebben we een NICE-OHMS systeem ontwikkeld op basis van een external cavity diode laser, werkend tussen 1510 – 1630 nm, met behulp van commerciële apparatuur en de stroommodulatie voor de stabilisatie van de laser frequentie. In hoofdstuk 9 worden de resultaten van spectroscopische metingen met de NICE-OHMS sensor van acetyleen, methaan en waterstofcyanide (HCN) gepresenteerd. We hebben een NEAS van  $4,1 \cdot 10^{-10} \text{ cm}^{-1} \text{ Hz}^{-1/2}$  bereikt met een cavity finesse van 1570 en een gevoeligheid van 0,93 ppbv. Bovendien werd het systeem toegepast op de detectie van HCN in zoete amandelen.

# Acknowledgments

**Z**UM SCHLUSS DIESER DISSERTATION möchte ich allen danken, die zum Gelingen der Arbeit beigetragen haben. Diese Arbeit erfolgte im Rahmen eines Zweitmittelpjektes, das von der Stichting FOM gefördert wurde und für deren finanzielle Unterstützung ich mich bedanken möchte.

During the period of my Ph.D., I have had cause to be grateful for the advice, support and understanding of many people. In particular I would like to express my sincere appreciation and gratitude to my supervisor Frans Harren for his continuous moral and technical support, as well as his unflagging enthusiasm. This work has also benefited greatly from much advice, and many useful discussions with Simona Cristescu, Julien Mandon, Denis Arslanov and Denys Marchenko. A special thanks to Simona and Julien for their endless effort to help throughout my thesis work. I am deeply indebted to my manuscript committee, Jos Oomens, Britta Redlich and Ove Axner, without whom the worth of this effort would have been greatly lessened. I also would like to express my gratitude to Dave Parker for providing me the opportunity to perform research in his department and to my colleagues for their support and comradeship during the exciting last four years.

Mein erster Dank gilt Frans Harren und Dave Parker, die es mir ermöglicht haben, meine Doktorarbeit an diesen spannenden Experimenten in ihrer Arbeitsgruppe zu schreiben und bei Fragen stets ein offenes Ohr hatten. Ove Axner, Jos Oomens und Britta Redlich danke ich für die Übernahme des Gutachtens dieser Arbeit und Ove stellvertretend für seine Gruppe für die Gastfreundlichkeit und Unterstützung während meines Aufenthaltes in Schweden. Auch allen anderen Mitgliedern unserer Gruppe möchte ich für die letzten Jahre danken. Durch die tolle Atmosphäre in der Gruppe hat es auch dann Spaß gemacht, zur Arbeit zu kommen, wenn es experimentell mal nicht so gut lief. Egal ob bei experimentellen oder theoretischen Schwierigkeiten, ich konnte mich immer an sie wenden. Auch die gemeinsame Zeit im Labor möchte ich nicht missen. Außerdem hatten eine Reihe von Leuten großen Anteil an der Realisierung meiner Arbeit. An dieser Stelle möchte ich mich bei allen bedanken, die mich während dieser Arbeit unterstützt und deren Gelingen erst ermöglicht haben. Insbesondere möchte ich noch einmal Julien Mandon und David Mundy meinen Dank für das Korrekturlesen dieser Arbeit aussprechen.

Außerdem geht mein Dank an: Cor Sikkens, Peter Claus, Leander Gerritsen, Magda Speijers, Erna Gouwens, Afric Meijer, Andre Eppink, Alexander von Zastrow, Sjoerd Vogels, Jolijn Onvlee, Chris Berkhout, Niek Janssen, Phil Brown, Anne Neerincx, Roy Scheidsbach, Mohiudeen Azhar, Devasena Samudrala, Yuwei Jin, Masha Kiseleva und Faisal Nadeem. Es gab noch mehr Personen, die mir in irgendeiner Form geholfen haben, aber ich bitte darum, mir zu verzeihen, sollte ich jemanden nicht namentlich in dieser Liste erwähnt haben. Weiterhin möchte ich Chris Berkhout und Peter Claus für die umfangreiche Hilfe mit der Elektronik und der technischen Realisierung danken. Ein herzlicher Dank geht an die Werkstatt des Instituts, insbesondere an Gerben Wulterkens stellvertretend für das gesamte Team für die Realisierung der externen Kavität für den Quantenkaskadenlaser. Weiterhin möchte ich mich bei den Mitarbeitern der Etatverwaltung bedanken, die sich um die reibungslose Bestellung der benötigten Komponenten gekümmert haben, sowie bei Magda Speijers und Erna Gouwens aus dem Sekretariat für die Erledigung der organisatorischen Dinge.

In schöner Erinnerung werden mir auch die außeruniversitären Aktivitäten mit euch bleiben. Die Organisation der OIIMMpiad war ein besonderes und großartiges Ereignis, deren Kommission ich hier auch erwähnen möchte. Dann möchte ich Hatzi danken für die schönen Jahre und das Verständnis in den letzten Monaten. Ebenfalls geht mein Dank auch an meine Freunde für die schöne (in letzter Zeit sehr seltene) Zeit neben der Uni. Schlussendlich möchte ich meiner Familie danken für ihre Unterstützung und den Glauben an meinen Weg.

# List of publications

1. R. Centeno, J. Mandon, S.M. Cristescu, F.J.M. Harren, *Three mirror off axis integrated cavity output spectroscopy for the detection of ethylene using a quantum cascade laser*, Sensors and Actuators B: Chemical, 203, 311–319 (2014), DOI: <http://dx.doi.org/10.1016/j.snb.2014.06.122>
2. R. Centeno, J. Mandon, S.M. Cristescu, F.J.M. Harren, *Sensitivity enhancement in off-axis integrated cavity output spectroscopy*, Optics Express, 22, 23, 27985 – 27991 (2014), DOI: <http://dx.doi.org/10.1364/OE.22.027985>
3. R. Centeno, D. Marchenko, J. Mandon, S.M. Cristescu, G. Wulterkens, F.J.M. Harren, *High power, widely tunable, mode-hop free, continuous wave external cavity quantum cascade laser for multi-species trace gas detection*, Applied Physics Letters, 105, 261907 (2014), DOI: <http://dx.doi.org/10.1063/1.4905281>
4. R. Centeno, J. Mandon, S.M. Cristescu, F.J.M. Harren, *External cavity diode laser-based detection of trace gases with NICE-OHMS using current modulation*, Optics Express, 23, 5, pp. 6277–6282 (2015), DOI: <http://dx.doi.org/10.1364/OE.23.006277>
5. R. Centeno, J. Mandon, S.M. Cristescu, F.J.M. Harren, *Influence of ethanol on breath acetone measurements using an external cavity quantum cascade laser*, submitted
6. E. Crespo, S. Devasena, C. Sikkens, R. Centeno, S.M. Cristescu, F.J.M. Harren, *Proton-Transfer Reaction Mass Spectrometry (PTR-MS) in combination with Thermal Desorption (TD) for sensitive off-line analysis of volatiles*, Rapid Communications in Mass Spectrometry, 26, 990–996 (2012), DOI: <http://dx.doi.org/10.1002/rcm.6191>



# Curriculum vitae

## Raymund Centeno

Date of birth: July 1, 1986

Place of birth: Bochum, Germany

### Design Engineer

ASML, the Netherlands

2015 - present

### PhD researcher in Physics

Radboud University Nijmegen, the Netherlands

Thesis title: *Advancing the detection of molecules in gas phase with infrared lasers.*

*Further development of semiconductor laser-based cavity enhanced absorption spectroscopy*

2010 - 2015

### MSc. in Physics

Radboud University Nijmegen, the Netherlands

Thesis title: *Analysis of trace gas molecules.*

*Characterization and optimization of a proton-transfer reaction ion trap mass spectrometer*

2008 - 2010

### BSc. in Physics

Radboud University Nijmegen, the Netherlands

Thesis title: *Active contours: How to find a doublecross pattern written in turbulent air*

2005 - 2009







Almost everything we do in daily life results in the release of volatile organic species to the atmosphere. Whether we drive a car, cook or breathe, these trace gases accompany us unwittingly in everyday life, and have a large impact on it. Laser spectroscopy enables the detection and quantification of trace gases by studying the absorption or emission of electromagnetic radiation. How can this significantly contribute to further improvement of our life quality? Laser spectroscopy is such a valuable tool for gas sensing and chemical analysis, because through recent advances trace gases can be scrutinized with high sensitivity and selectivity to enable advanced knowledge of their origin and composition. **Advancing the detection of molecules in gas phase with infrared lasers** examines these advances, and how infrared laser spectroscopy can be used in a diverse range of industrial, medical, and environmental applications. The book encompasses a systematic introduction to the relevant spectroscopic techniques in a clear, yet fundamental manner and provides applications of infrared laser spectroscopy for molecular gas sensing to give examples of the new and exciting current developments.

ISBN 978-94-6259-605-4



9 789462 596054 >